

Biophysical Studies of the Interactions Between Small Molecule Inhibitors and Viral Protein Targets

BY

ALEKSANDAR ANTANASIJEVIĆ

B.S., University of Belgrade, Serbia, 2010

M.S., University of Belgrade, Serbia, 2011

THESIS

Submitted as partial fulfillment of the requirements
for the degree of Doctor of Philosophy in Biochemistry and Molecular Genetics
in the Graduate College of the
University of Illinois at Chicago, 2016

Chicago, Illinois

Defense Committee:

Dr. Michael Caffrey, Chair and Advisor

Dr. Arnon Lavie

Dr. Miljan Simonović

Dr. Vadim Gaponenko

Dr. Lijun Rong, Microbiology and Immunology

Dr. Duncan Wardrop, Chemistry

This thesis is dedicated to my dear mother Verica, for her unconditional love and support.

ACKNOWLEDGEMENTS

I would like to thank my advisor Dr. Michael Caffrey for his guidance, support and for all the effort he has invested in my education and development as scientist. He is an exceptional scientist, educator and a great person, and it was my honor to work with him and learn from him during my PhD.

I would also like to express my gratitude to my committee members for their generous support in ideas, mentoring and material. Most of the work described in the thesis depended on close collaborations with their labs and would not be possible without active resource exchange. In particular, I would like to thank Dr. Arnon Lavie and all of his lab members for the support on the X-ray crystallography studies on hemagglutinin and several other joint projects. Chemical optimization of tert-butyl-hydroquinone was done in collaboration with Wardrop lab. Most of the compound synthesis was performed by Nick Hafeman and Dr. Duncan Wardop. Mammalian cells, viral protein vectors, virus handling protocols and a few antiviral compounds were kindly provided by Dr. Lijun Rong. Dr. Han Cheng from Rong lab oversaw and helped with several different experiments. I would also like to thank Dr. Miljan Simonović and Dr. Vadim Gaponenko for their support in lab resources and mentoring.

I would like to thank Dr. Arnab Basu and Dr. Terry Bowlin from Microbiotix Inc. for providing several antiviral compounds and for collaborating with us on multiple influenza projects.

Special gratitude goes to Dr. Ben Ramirez and Dr. Gerd Prehna of the Center for Structural Biology for allowing me to use the equipment and resources at the Center, as well as for providing all necessary training and support.

I would also like to thank College of Medicine and Graduate College of the University of Illinois at Chicago (UIC), as well as Chicago Biomedical Consortium (CBC) for financial support.

At the end I would like to thank all lab heads, members and all employees of the Department of Biochemistry and Molecular Genetics for creating an idyllic work environment full of support and mutual respect.

Contribution of Authors

In the thesis I have included the data and text from previously published work that was directly related to the main thesis project (Antanasijevic et al., 2013; Antanasijevic et al., 2014a; Antanasijevic et al., 2014b; Basu et al., 2014; Antanasijevic et al., 2016;). The origin of the data is appropriately indicated at the beginning of each chapter. All published and non-published work was performed through collaborations with different laboratories and institutions and the author contributions are indicated in the main text of the manuscript. In the thesis, I am including only the experiments mainly performed by myself using the resources from Michael Caffrey's laboratory. The contributions in effort and resources from other researchers and laboratories (where present) are described in the text.

Table of contents

Chapter 1. Introduction	1
Chapter 1.1 - Influenza virus	1
Chapter 1.2 - Hemagglutinin	5
Chapter 1.3 - Development and characterization of influenza fusion inhibitors	10
Chapter 1.4 - Studies on the regulation of pH-induced conformational change in HA	12
Chapter 1.5 - WaterLOGSY and Saturation Transfer Difference (STD) method comparison and optimization	15
Chapter 1.6 - Application of virus-like particles (VLP) to NMR characterization of viral membrane protein interactions	17
Chapter 2. Methods	20
Chapter 3. Results	34
Chapter 3.1 - Characterization of the stem-loop region	34
Chapter 3.2 - Studies on the mechanism behind the early and intermediate steps of the fusion process	44
Chapter 3.3 - Characterization of Group 1 inhibitors: MBX2329 and MBX2546	55
Chapter 3.4 - Group 1 inhibitors: Determining the binding site and mode of action of RLC	75
Chapter 3.5 - Characterization of Group 2 inhibitors: TBHQ	81
Chapter 3.6 - Chemical optimization of TBHQ	86
Chapter 3.7 - NMR methods development: Comparison of the sensitivities of WaterLOGSY and STD NMR experiments	114
Chapter 3.8 - NMR Methods Development: Application of virus-like particles (VLP) to NMR characterization of viral membrane protein interactions	125
Chapter 4. Conclusions	137
Chapter 4.1 - Characterization of the stem-loop region	137
Chapter 4.2 - Studies on the mechanism behind the early and intermediate steps of the fusion process	138

Table of Contents (continued)

Chapter 4.3 - Characterization of Group 1 inhibitors: MBX2329 and MBX2546	143
Chapter 4.4 - Group 1 inhibitors: Determining the binding site and mode of action of RLC	145
Chapter 4.5 - Characterization of Group 2 inhibitors: TBHQ derivatives	147
Chapter 4.6 - NMR methods development	150
Appendices	156
Appendix A	156
Appendix B	157
Appendix C	159
Appendix D	160
Literature	161
VITA	173

List of Tables

TABLE I --- Most recent flu pandemics and their consequences

TABLE II --- Summary of the mutational effects to influenza H5 HA

TABLE III --- Data collection and refinement statistics for H5 HA under different conditions

TABLE IV --- IC50 results for MBX2329 and MBX2546 against H5 HA mutants

TABLE V --- TBHQ and its derivatives

TABLE VI --- The comparison of chemical properties of silicon and carbon

TABLE VII --- Comparison of the results from the infectious virus and pseudovirus entry inhibition assays

TABLE VIII --- Average $S/N^{wl}/S/N^{std}$.

List of Figures

Figure 1. Influenza virus structure.

Figure 2. Hemagglutinin structure and role in viral entry.

Figure 3. HA as a drug target.

Figure 4. The structures of TBHQ, MBX2329, MBX2546 and RLC.

Figure 5. Conformational changes in HA.

Figure 6. Schematic representation of the WaterLOGSY and STD experiments.

Figure 7. Location of mutant sites within H5 HA.

Figure 8. Western blot and hemagglutination assay of virus-like particles of H5 HA wild-type and mutants.

Figure 9. HA-mediated entry of H5 HA wild-type and mutant virions.

Figure 10. Mutant effects on entry inhibition of H5 HA by monoclonal antibody C179.

Figure 11. Space-filling representation of the mutational effects on H5 HA entry and entry inhibition.

Figure 12. The studies of H5 HA stability as a function of pH.

Figure 13. Relocalization of the fusion peptide at pH 6.5.

Figure 14. pH induced rotation of the side chain of H38.

Figure 15. pH dependent change in anchoring of Glu69 to His114.

Figure 16. Activity of MBX2329 and MBX2546 against pseudovirus entry.

Figure 17. MBX2329 and MBX2546 bind to the conserved conformational epitope in the HA stem region.

Figure 18. Surface plasmon resonance experiments with H5 HA and the two inhibitors.

Figure 19. MBX2329 and MBX2546 bind to nonoverlapping sites on HA.

Figure 20. Mutations affecting the inhibitory properties of MBX2329 and MBX2546.

Figure 21. Molecular dynamics models of the MBX2329 and MBX2546 interactions with H5 HA.

Figure 22. Crystal structure of H5 HA with MBX2546.

Figure 23. NOESY-based determination of the structure of MBX2546 in the bound state.

Figure 24. pH-based limited proteolysis assays confirm that MBX2329 and MBX2546 act as fusion inhibitors.

Figure 25. Thermal shift assay results for H5 HA with MBX2329 and MBX2546.

Figure 26. Crystal structure of RLC in complex with H5 HA.

Figure 27. Overlay of the low pH structure of HA and the structure of H5 HA complex with RLC.

Figure 28. Sequence and structure alignment in the vicinity of RLC binding site.

Figure 29. NMR studies on RLC interactions with H5 HA.

Figure 30. TBHQ inhibits H3 and H7 HA-mediated entry.

Figure 31. TBHQ binds to the H3 and H7 HA stem loops.

Figure 32. TBHQ stabilizes the neutral pH conformation of H7 HA.

Figure 33. Redox chemistry of TBHQ.

Figure 34. Stability of TBHQ, TBBQ and Compound 11.

Figure 35. Structure of TBHQ in complex with H3 HA.

Figure 36. Cytotoxicity of compounds 4, 5, 6 and 11.

Figure 37. Molecular dynamics models of compounds with H7 HA highlighting important hydrogen bonding and hydrophobic interactions.

Figure 38. STD comparison of the interactions of H7 HA with compounds 4, 24, 25 and 26.

Figure 39. Stability of compounds 24, 25, 26 and 27 over time.

Figure 40. Stability and mode of binding of compound 32.

Figure 41. Activity of the compounds from TBHQ series against infectious H3 N2 virus.

Figure 42. TBHQ competition assays.

Figure 43. WaterLOGSY and STD pulse sequences and the compounds used in the experiments.

Figure 44. Optimization of the STD parameters.

Figure 45. Comparison of WaterLOGSY and STD spectra.

Figure 46. Quantified differences in sensitivities of individual resonances in the WaterLOGSY and STD NMR experiments.

Figure 47. Protein saturation in WL and STD experiments.

Figure 48. WL NMR detection of small molecule binding to serum proteins present in cell culture media.

Figure 49. SDS PAGE stained by Coomassie Blue showing purification of HA-VLP.

Figure 50. WL NMR spectra of the MBX2329 interaction with recombinant HA and HA embedded in VLP.

Figure 51. STD NMR characterization of the MBX2329 interaction with recombinant HA and HA embedded in VLP.

Figure 52. CORCEMA simulations of relative STD signal as a function of correlation time and target protein concentration for the HA-MBX2329 experiments.

Figure 53. NMR characterization of NA kinetic activity in NA embedded in VLP.

Figure 54. Characterization of inhibitor DANA binding to NA-VLP by NMR.

Figure 55. Comparison of H5 HA structure at pH 7.0 and pH 5.5 and H1 HA structure at pH 5.5.

Figure 56. Positions of the His residues presumably undergoing protonation at low pH.

Figure 57. Chemical optimization of the TBHQ.

Figure 58. Raw SPR data for the binding of MBX2329 and MBX2546 to recombinant H5 HA.

Figure 59. Proposed binding sites of MBX2329 (blue), MBX2546 (yellow), RLC (orange) and TBHQ (red) on HA.

List of Abbreviations

NMR	–	Nuclear magnetic resonance
HA	–	Hemagglutinin
NA	–	Neuraminidase
TBHQ	–	Tert-butyl-hydroquinone
XRC	–	X-ray crystallography
STD	–	Saturation transfer difference
TSA	–	Thermal shift assay
DSF	–	Differential scanning fluorimetry
PEI	–	Polyethylene-imine
VLP	–	Virus-like particles
HA1	–	Head domain of hemagglutinin
HA2	–	Fusion domain of hemagglutinin
FP	–	Fusion peptide
WL	–	WaterLOGSY NMR
STD	–	Saturation Transfer Difference NMR
HSQC	–	Heteronuclear single quantum coherence spectroscopy
HMQC	–	Heteronuclear multiple quantum coherence spectroscopy

Summary

The main focus of my PhD research was on influenza virus. The main regulator of influenza localization and a central player in viral entry is one of three envelope proteins – hemagglutinin (HA). The central role it plays in the entry process makes it an ideal target for therapeutic intervention. Over the course of my research I have applied a variety of biophysical and virology techniques to study the exact mechanism by which this protein regulates viral entry. However the main focus was on the small molecule compounds that can block viral entry by interfering with normal HA function. By studying the mechanisms of interaction and inhibition of these “fusion” inhibitors we have gathered very useful knowledge that helped us understand potential target sites on the HA surface. I have identified a very conserved region on HA called the stem-loop region that we believe is its “Achilles’ heel”. Many different compounds, antibodies and peptides are thought to bind to this region and interfere with the regulation of the fusion step of the entry process. I have applied nuclear magnetic resonance (NMR), mutagenesis, X-ray crystallography and other biochemical and virological methods to gather molecular level detail on the mechanism of inhibition by different small molecule inhibitors. In the subsequent steps I have applied the gathered knowledge to navigate the chemical optimization of these inhibitors and improve their activity against different types of influenza virus.

A large portion of the work was focused on developing and optimizing the methodology that can help us learn more about the interactions between the inhibitors and different protein targets. I have developed an x-ray crystallography based method for studying low pH-induced conformational change that helped us learn more about the fusion triggering mechanism and pointed towards novel drug sites on the protein surface. HA construct that was designed over the course of research can also be used in combination with NMR to study the dynamics of this protein under different conditions and to identify the amino-acids interacting with various inhibitors. In addition, I have characterized and optimized WaterLOGSY and Saturation Transfer Difference (STD) NMR techniques and extended their application to whole virus systems. Moreover, I have developed protocols to obtain high purity virus-like particles (VLP) and optimized these protocols for their application with NMR and other biophysical techniques.

Chapter 1 - Introduction

Chapter 1.1 - Influenza virus

Influenza virus belongs to the family of Orthomyxoviridae. It infects birds and mammals causing respiratory diseases (“flu”) with symptoms including but not limited to high fever, cough, body ache, runny nose, muscle pain and occasionally pneumonia (<http://www.cdc.gov/>). Most commonly influenza virus is transmitted by aerosols created by coughing or sneezing. Airborne transmission and relative stability give this virus very high epidemic potential. Influenza spreads in yearly cycles (seasonal epidemics), resulting in around 4 to 6 million cases of severe illness and 250,000 to 500,000 deaths per year (<http://www.cdc.gov/>; Fauci, 2005). These numbers increase significantly in pandemic years, happening every few decades and taking millions and millions of lives (Table I) (Potter, 2001; Donaldson et al., 2009).

TABLE I

Most recent flu pandemics and their consequences

Name of pandemic	Date	Deaths	Case fatality rate
Asiatic (Russian) Flu	1889-1890	1 million	0.15%
Spanish Flu	1918-1920	20 – 100 million	2%
Asian Flu	1957-1958	1 to 1.5 million	0.13%
Hong Kong Flu	1968-1969	1 million	<0.1%
2009 “Swine” Flu	2009-2010	18,000	0.03%

Additionally, there are some strains of influenza virus that are more specific for animals (birds and some mammals) but can also infect humans and cause serious consequences. In 2004, an avian adapted, highly pathogenic strain of H5N1 started spreading worldwide, affecting bird populations. However, this virus could also infect humans causing severe respiratory symptoms and having much higher fatality rate than any other flu virus (~60%, Boni et al., 2013). Fortunately, the H5N1 strains did not develop an ability to efficiently transmit in humans which has prevented more devastating consequences.

Given all this information, it is clear why influenza is considered to be one of the biggest health threats worldwide, and why there is urgency for anti-influenza vaccines and therapeutics. Currently, there are only 4 drugs for the prevention and treatment of influenza available on the market, and few others in clinical trials. The 4 drugs proved to be very useful tools in the fight against flu, but also showed some undesirable properties that are starting to limit their applicability. Most of the problems are related to the relative lack of efficiency, development of resistance in the new viral strains, drug administration, and some dangerous side effects (Waten et al., 2013; Yang et al., 2013; Zhu et al., 2012; Papp et al., 2011; Vanderlinden et al., 2010). To overcome the appearance of these and similar problems and continue the fight against flu it is necessary to discover more therapeutics, perhaps with new mechanisms of anti-influenza action that can be used alone or in combination with other drugs.

Influenza is an enveloped virus. Its' genome is single stranded RNA based consisting of eight single stranded negative-sensed RNA segments encoding 12 proteins with different roles, including three subunits of the viral specific RNA polymerase (PA, PB1 and PB2), the nucleoprotein (NP), the matrix protein (M), two non-structural proteins (NS1 and NS2), and three envelope proteins hemagglutinin (HA), neuraminidase (NA) and the proton channel M2 (Figure 1.). HA and NA are the most abundant proteins on the viral surface and they completely define the antigenic group of the virus. HA,

present in approximately 400 copies per viral particle, is the major determinant of viral localization and a central player in viral entry (Hamilton et al., 2012; Luo, 2012). On the other hand, NA (~100 copies per particle) is suggested to aid the exit and release of the virus from the host cell (Air, 2012).

Influenza enters the cells in an endosome-dependent way. Initial cell recognition and attachment is through sialyl-lactose residues on the cell surface. Hemagglutinin recognizes the specific type of sugar residues (2,6-sialyl-lactose for human, or 2,3-sialyl-lactose for avian flu strains) and forms a relatively loose interaction with them. In the subsequent steps, through a mechanism that is still poorly understood, virus gets endocytically internalized. Endosome evolution triggers a pH-induced conformational change in HA that eventually results in the fusion of viral envelope and endosomal membrane and the release of all viral material into the cell. This process is known as the “endosome escape”. Genetic material is then transcribed by the influenza polymerase and viral components are expressed in cells. As the new viral particles bud on the cell surface, neuraminidase (NA) cleaves the sialyl-lactose residues, promoting the viral release from the cell surface.

Influenza induces cell death and tissue damage directly by interfering with internal cell signaling leading to apoptosis, and indirectly by inducing strong immune response and the development of inflammation. Influenza strains with the preference towards 2,6-sialyl-lactose mostly infect cells in the upper respiratory tract, mainly larynx and trachea (due to the presence of 2,6-SL receptors), causing mild to moderate flu symptoms (de Graaf & Fouchier, 2014). These are referred to as the “human” flu strains because they are easily transmissible between humans and they have a very high epidemic potential. Example is H3N2 virus, most common seasonal strain of influenza. On the other hand, strains that prefer 2,3-sialyl-lactose receptors, as is the case with avian flu viruses (e.g. H5N1 and H7N9), tend to infect the cells in the lower respiratory tract of humans (bronchi and alveoli) due to the presence of 2,3-SL receptors causing more severe symptoms including pneumonia. The final result is much higher

mortality that ranges between 2 and 60 %. However, targeting of lower respiratory tract consequently gives these viruses a much lower epidemic potential as they are less likely to efficiently transmit between humans (de Graaf & Fouchier, 2014).

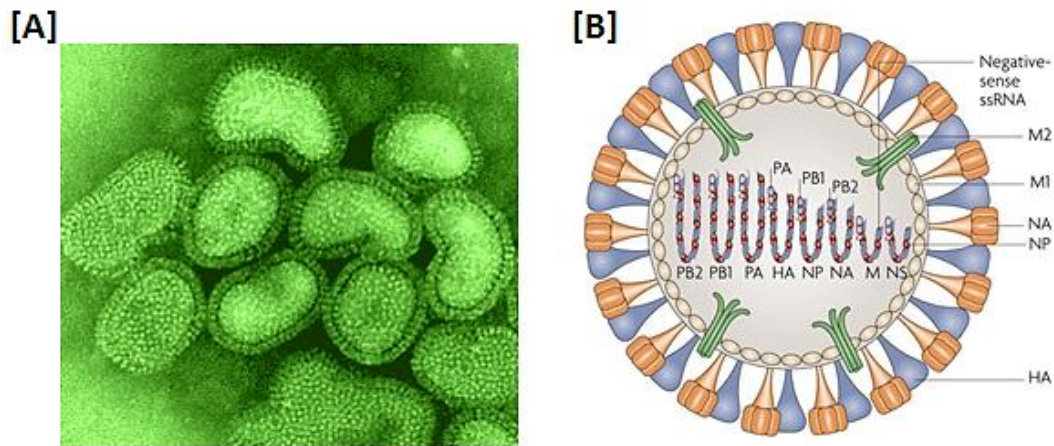


Figure 1. Influenza virus structure. [A] Electron micrographs of the flu virus; [B] Schematic representation of the virus structure illustrating all the viral components and their positions (Adapted from Nelson & Holmes, 2007)

Chapter 1.2 - Hemagglutinin (HA)

Hemagglutinin plays a central role in influenza virus entry. It is a well-studied protein and the crystal structures in several different conformations have been determined (Figure 2.A). Originally, it is expressed as a 550 amino-acid precursor (HA0) that interacts with two other monomers forming a trimer (hemagglutinin “spike”). Each of the monomers gets cleaved post-translationally into two subunits (HA1 and HA2) that stay connected by non-covalent interactions and a disulfide bond. HA1 (shown in gray in Figure 2.A) carries a receptor binding site and is involved in target cell recognition and binding, while HA2 (shown in blue in Figure 2.A) represents a pH sensitive nano-machine that is able to extend at low pH and cause fusion of the endosomal and viral membranes (Hamilton et al., 2012; Luo, 2012).

In the first step of the entry process HA head domain (HA1) attaches to sialyl-lactose sugar residues on the cell surface (Figure 2. B). Cell membrane then engulfs the virus into the endosome. As the endosome evolves, the internal pH decreases the original folded structure of the HA molecule becomes unstable, causing it to partially unfold and release a very hydrophobic portion of HA2 that was previously hidden within the protein. This so-called “fusion peptide” acts like a molecular hook that stabs the endosome membrane and attaches to it. Once the attachment and refolding process is completed, the hook is retracted causing two membranes to get in very close proximity. Eventually, this process results in fusion of the endosomal and viral membranes and the release of the viral material into the cytoplasm (Hamilton et al., 2012, Russell, 2014).

Given the fundamental importance of hemagglutinin for influenza virus entry, it is clear why this protein was considered to be one of the most appealing targets for therapeutics. Unfortunately, the realization of this idea has been very unsuccessful. Currently, there are 4 available anti-influenza drugs on the market that fall into 2 categories, the M2 ion channel blockers (amantadine and rimantadine)

and neuraminidase inhibitors (oseltamivir and zanamivir). There are also ~20 other drugs in clinical trials that target both, viral and host factors. Out of these, only 2 are designed to block viral entry by inhibiting HA and these are both monoclonal antibodies (Wathen et al., 2013; Gasparini et al., 2014). There are no reports of small molecule inhibitors of HA in clinical trials.

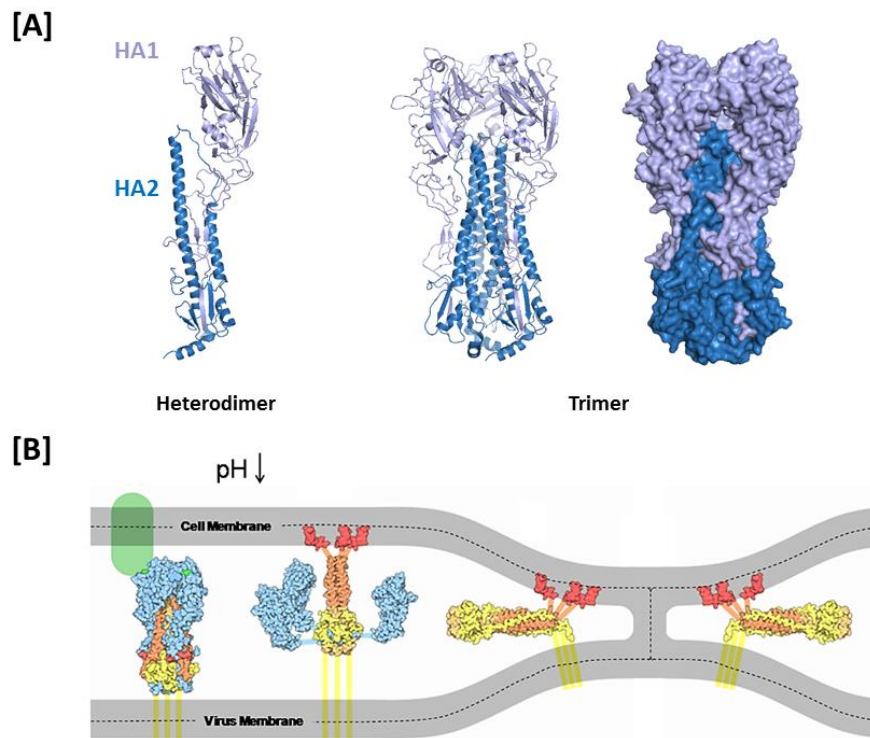


Figure 2. Hemagglutinin structure and role in viral entry. [A] 3D structure of hemagglutinin ectodomain (adapted from PDB entry: 2FK0) and [B] the proposed mechanism of fusion process (adapted from Goodsell, 2006)

Part of the reason for this shortcoming is due to standard limitations of the methodology used (the relative inefficiency of current drug screening and drug development approaches, particularly for membrane proteins), and also due to the problems specific for viral proteins as targets for therapeutics (delivery, development of resistance, limitations of certain animal models). The other part lies in the fact that a significant effort in the drug pursuit was focused towards finding compounds that block the HA – sugar receptor interactions, an approach that proved to be very unfruitful (to date). Some new studies even suggest that this interaction is not essential for influenza entry (Stray et al., 2000; Kumari et al., 2007).

In the last two decades, the course of research has been turning towards the development of so called “fusion inhibitors”. These inhibitors are suggested to bind to the HA stem-loop region, stabilizing the native HA conformation, and preventing the pH-induced conformational change from occurring (Figure 3.A). The stem-loop region is composed of HA1 and HA2 segments that are very sensitive to pH. “Metastability” of this region makes it susceptible to such a large structural rearrangement induced by pH shift of just one unit (Skehel and Wiley, 2000;). So, if another element (a compound, peptide or an antibody) that can cause the stabilization/destabilization of this region is introduced into the system it is possible that element would block or postpone the fusogenic conformational change, thereby inhibiting influenza entry.

Consequently, this blocking of influenza HA action would lock the entire virus in the endosome resulting in its’ slow degradation. Due to the absolute necessity of maintaining the metastable nature of HA the stem loop region is also very conserved across influenza kingdom, making this site even more attractive as a drug target (Steel et al., 2010). The probability for development of resistant strains would be lower for all drugs that could bind in this region.

There are 18 different HA types that fall into two evolutionary conserved groups (Figure 3.B). With respect to the work presented herein, the representatives of Group 1 are H1 HA (from 2009 “swine” flu) and H5 HA (found in “bird” flu from 2004), while in Group 2 there are H3 HA (present in most common seasonal flu strains) and H7 HA (found in H7N9 avian flu from 2013). The level of sequence conservation ranges from 50 – 80 % within the group and 30 – 70 % between two groups. As a consequence of this discrepancy, the regulatory and functional properties of HA are occasionally significantly different for different strains despite only minor structural variations. From the pharmacological standpoint the major problem is that the inhibitors tend to be group specific (i.e. inhibitors of Group 1 HA do not cross-react with Group 2 HA and vice versa) (Xie et al., 2011).

Despite all problems and limitations when working with influenza HA, the development of fusion inhibitors has shown to be a very fruitful idea. Several compounds, peptides and antibodies that can act as fusion inhibitors were discovered in the last few years as a result of growing interests (Wathen et al., 2013; Yang et al., 2013; Zhu et al., 2012; Papp et al., 2011; Vanderlinden et al., 2010; Zhu et al., 2011; Boltz et al., 2010; Colpitts et al., 2013; Basu et al., 2014; Li et al., 2015; Antanasijevic et al., 2013). While the antibodies are subjects of substantial and detailed studies, the great majority of small molecule compounds were only discovered in library screens and they have not been characterized in detail. For some of the small molecules we have a rough idea of the binding site based on escape mutants. For others we have certain assays showing the basic mode of action. Nevertheless, comprehensive research that would give detailed structural characterization of the mechanism of inhibition for most of these compounds is still lacking. We believe that the knowledge obtained in research like this would help us understand what makes some of these compounds inhibitory and others not. In other words, it could help us decipher the interaction pattern required to disturb the HA1-HA2 interface and block the virus from entering the cell. One could use this knowledge as a guide in designing new and better therapeutics and/or as a tool to learn something about the HA function. Furthermore, given the

structural and functional similarity between influenza HA and other glycoproteins from enveloped viruses like HIV, Ebola, SARS, the general principles from this type of research can be applied to all these systems. It is easy to understand the potential benefit if a new entry inhibitor was to be developed against other enveloped viruses.

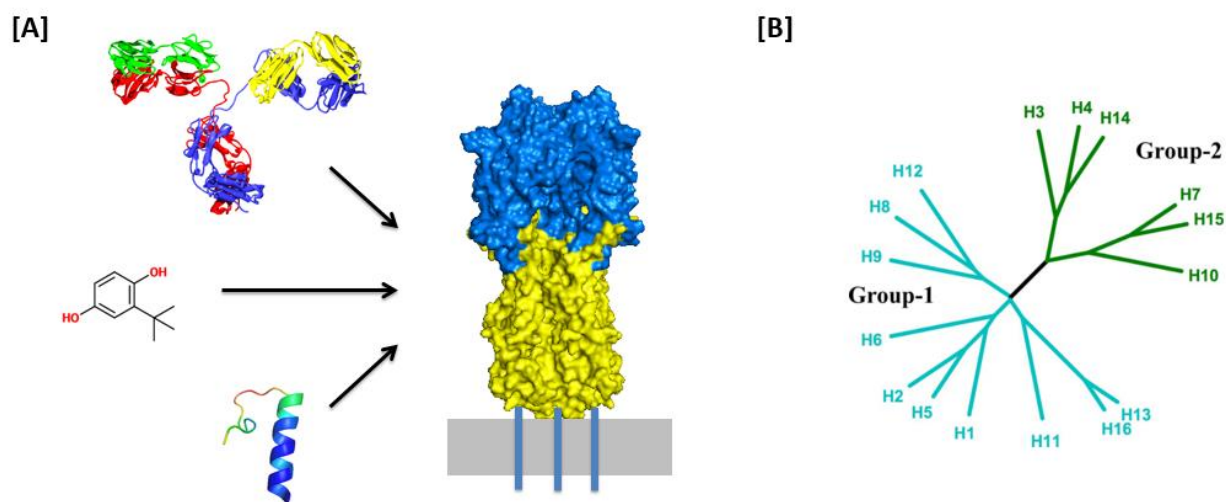


Figure 3. HA as a drug target. [A] Three different types of fusion inhibitors (antibodies, small molecules and peptides) and their target - the stem-loop region (HA1 – HA2 interface), highlighted in yellow; [B] Two evolutionary conserved groups of influenza HA (adapted from Russell et al, 2008).

Chapter 1.3 - Development and characterization of influenza fusion inhibitors

We have chosen to study the fusion inhibitors against both Group 1 and Group 2 HA. We find that this approach leads to more generally applicable conclusions and it brings us one step closer to designing a universal, broad-spectrum fusion inhibitor. The structures of all fusion inhibitors studied are shown in Figure 4.

The Group 2 inhibitor used was tert-Butyl-Hydroquinone (TBHQ), a small molecule of simple structure that is also an FDA approved food preservative present in many commonly used groceries and food types to the concentrations up to 2 mM (van Esch, 1986). Its anti-influenza properties have been discovered in the late 1980s, and since then it has been a subject of detailed characterization (Bodian et al., 1993; Luo et al., 1996; Russell et al., 2008; Antanasijevic et al., 2013). High resolution x-ray structures of the complex between TBHQ and H3 HA and H14 HA have been reported in the literature (Russell et al., 2008). Interestingly, this is the only small molecule fusion inhibitor of any type of influenza HA for which a structure in complex is available. In our work we have focused on the interactions between H7 HA and TBHQ. H7 HA belongs to Group 2 HA viruses and was present in H7N9, avian viral strain that had an outbreak in China in 2013 (Lam et al., 2015). It was discovered that this strain is able to infect humans with case fatality rate of ~ 19 %. We were the first group to show the activity of TBHQ against H7 HA based viruses (Antanasijevic et al., 2013) and the first group to use the structural data to perform chemical optimization of this compound. This work was done in collaboration with Duncan Wardrop's lab (Department of Chemistry, University of Illinois at Chicago).

The Group 1 inhibitors used were small hydrophobic molecules MBX2329, MBX2546 and RLC. All of the molecules were discovered in high throughput screening efforts performed in collaboration with Lijun Rong lab (Department of Microbiology and Immunology, University of Illinois at Chicago). The research on MBX2329 and MBX2546 was performed in collaboration with Microbiotix Inc (Worcester,

MA). After an HTS screen of 100,000 small molecules, these two compounds were identified based on their potency against H1 HA (Basu et al., 2014). In the initial experiments at the Rong lab these molecules were found to be very potent fusion inhibitors of H5 and H1 HA based viruses with the IC50 in the low micro-molar range. Additionally, the activity against infectious viruses was also demonstrated (Basu et al., 2014). Biophysical characterizations of the binding site, mode of action and inhibition mechanism were performed in our lab (Basu et al., 2014; Antanasijevic et al., 2014). In the studies, we have used mutagenesis, HA fusion assays, x-ray crystallography, nuclear magnetic resonance (NMR), surface plasmon resonance (SPR) and several other methods and techniques to obtain a detailed molecular understanding of their activity against hemagglutinin. This work was done in collaboration with Lijun Rong lab, Arnon Lavie lab, and Microbiotix Inc.

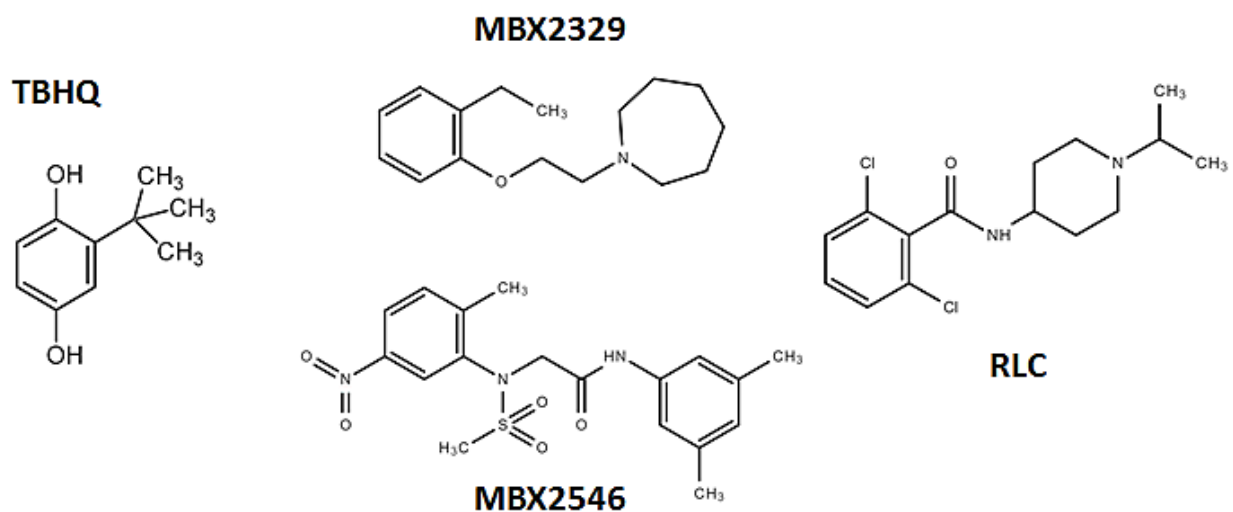


Figure 4. The structures of TBHQ, MBX2329, MBX2546 and RLC

Chapter 1.4 - Studies on the regulation of pH-induced conformational change in HA

Another major goal of the research was to use fusion inhibitors as tools in combination with structural biology and virology methods and techniques at our disposal to better understand the mechanism behind the fusogenic conformational change that HA undergoes. This pH-dependent process has been a subject of extensive research (Chernomordik et al., 1999; Madhusoodanan et al., 2003; Mittal et al., 2003; Ivanovic et al., 2013; Mair et al., 2014; Ivanovic et al., 2015; Costello et al., 2015). Kinetic data for many different HA strains can be found in the literature and the structures at the starting and final conformations of the fusion domain have been determined for H2 HA and H3 HA (Figure 5.A; Bullough et al., 1994; Xu et al., 2011). In the past couple of years cryogenic-electron microscopy (cryo-EM) has offered some valuable new insights regarding this complex process (Fontana et al., 2015). Based on all gathered data the “spring-loaded” mechanism of fusion has been established. As the pH is lowered, HA is suggested to go through a set of higher energy states characterized by increased dynamics and lower stability of the protein. Further drop in pH brings more positive charge to the trimer leading to the rearrangement of HA1 subunits to an open conformation where the space is formed for HA2 to completely extend. The 20-amino-acid loop in HA2 that connects the two helices (residues 56 – 75) also takes a helical secondary structure at low pH. This results in a full extension of HA2 and penetration of the fusion peptide into the endosomal membrane. During this process a very long helix is formed (~ 130 residues). However, this state is thought to be very unstable and the triple-helix structure folds back bringing the two membranes in close proximity until they become one entity and the pore is formed (Ivanovic et al. 2013; Xu et al., 2011). An alternative model suggests that the fusion peptide relocalization is the major driving force of the process (Garcia et al., 2015). In this case, MS studies seem to suggest that fusion peptide is the most dynamic part of the protein below pH 7.0 and that it actually drives the HA1 dissociation process and all the subsequent steps.

Despite extensive research efforts and scientific breakthroughs over the past century, we still have not developed the tools to study the late stages of the fusion process. Some of the states are very short-lived and nearly impossible to explore using the methodology available. Moreover, little is still known about the early and intermediate, reversible steps in the fusion process that induce the onset of spring-loaded conformational change. It is suggested that the coordinated protonation of HA at low pH is the key of all the structural rearrangements, but the complete mechanism of regulation and the amino-acid residues involved have been a matter of controversy.

The influenza community agrees that conserved histidine residues throughout the protein are the most likely candidates for the regulatory role, given the pKa values of their side-chains and the pH range at which the fusion takes place (Mair et al., 2014; Kalani et al., 2013; Thoennes et al., 2008; Stevens et al., 2004). Other charged amino-acids at different positions in the HA trimer, like arginine and glutamate have also been connected with the fusion control mechanism (Xu et al., 2011; Wang et al., 2015; Reed et al., 2009). However, despite the extensive mutagenesis work done over the years, consensus on the role and involvement of individual residues in regulation of this highly coordinated process is still lacking.

In this part of the study we have applied x-ray crystallography, mutagenesis, pseudovirus entry assays, fusion assays, and differential scanning fluorimetry on H5 HA (recombinant ectodomain and in the context of a virus) to learn more about the stem-loop region and how it is involved in the regulation of hemagglutinin-mediated fusion. Particular emphasis was on the pH dependency of protein structure and dynamics.

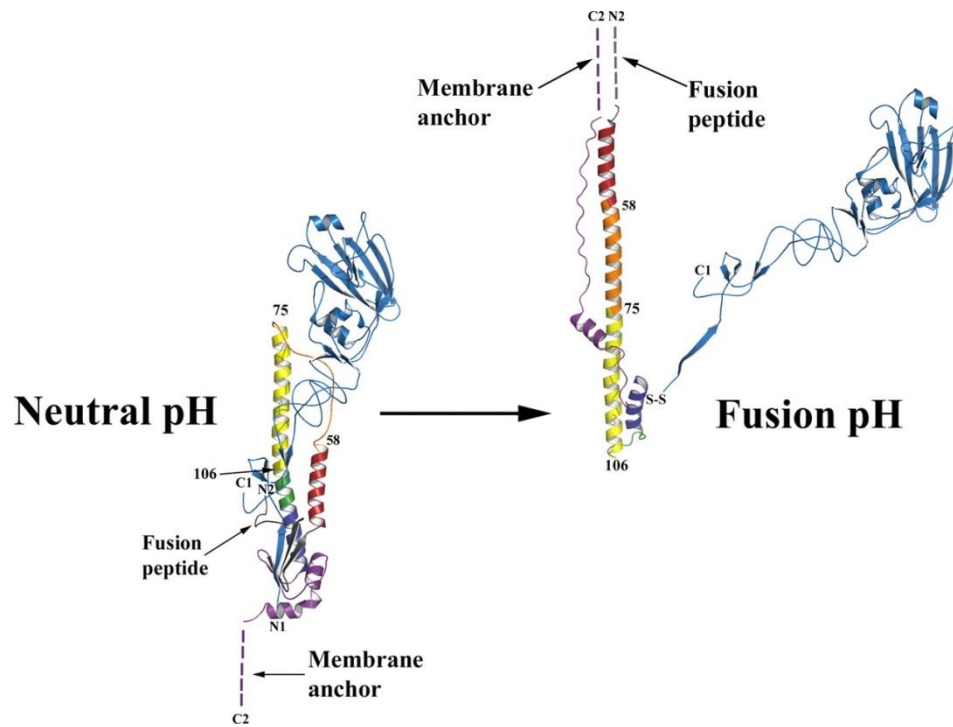


Figure 5. Conformational changes in HA. The structures of HA monomer at neutral and fusion pH (Adapted from Russell et al., 2008).

Chapter 1.5 - WaterLOGSY and Saturation Transfer Difference (STD) method comparison and optimization

(Adapted from Antanasijevic et al., 2014b; see Appendix A)

NMR has proven to be a powerful technique to characterize interactions between small molecules and large biomolecules (Carlomango et al., 2005; Williamson, 2009; Harner et al., 2013). The biomolecules under study may consist of proteins, DNA, RNA, and carbohydrates. The small molecules, termed ligands hereafter, may consist of natural ligands (e.g. substrates, products, receptors, inhibitors or activators), where NMR studies give insights into function, or drug-like molecules, in which NMR studies enable discovery and optimization of potency. NMR characterizations may occur via target-based (i.e. biomolecule) or ligand-based techniques. Target-based techniques employ chemical shift perturbations of the biomolecule and in some cases intermolecular NOEs between the ligand and target. Such experiments present the potential to not only identify binding (and affinity) but also the interaction site and, in favorable cases, the structure of the ligand-biomolecule complex (Shuker et al., 1996). However, target-based techniques require relatively large amounts of highly purified biomolecule (i.e. mg quantities), as well as labeling with stable isotopes (typically ^{13}C and/or ^{15}N), and are limited to relatively small molecular weight biomolecules (MW < 30 kDa). In the case of fast exchange (e.g. 100 sec^{-1} or $K_d > 0.1\ \mu\text{M}$, Williamson, 2009) and excess ligand, ligand-based techniques exhibit higher sensitivity due to narrower line-widths and multiple binding events, as well as lower spectral complexities (i.e. fewer signals). Moreover, ligand-based techniques present the potential to utilize smaller quantities, as well as unpurified samples, of targeted biomolecules, and labeling with stable isotopes is unnecessary. However, ligand-based techniques require additional experiments to identify the binding site (e.g. competition assays with ligands of known binding sites, mutagenesis of the target biomolecule, or high resolution x-ray structures).

WaterLOGSY (WL) and Saturation Transfer Difference (STD) are two popular ligand-based NMR experiments used to characterize interactions of small molecules with biomolecules (Dalvit et al., 2001; Mayer and Meyer, 2001). Both WL and STD are based on intermolecular NOEs to the transiently bound ligand ^1H (Figure 6.). In the case of WL, ^1H of bulk water are excited and magnetization is transferred from transiently bound water ^1H to bound ligand ^1H (Dalvit et al., 2000; Dalvit et al., 2001). Note that magnetization transfer to the bound ligand ^1H may also occur via indirect spin diffusion through exchangeable and nonexchangeable ^1H of the biomolecule and that exchangeable ^1H of ligands cannot be used as probes in WL (Dalvit et al., 2000; Dalvit et al., 2001). In the case of STD, a selected ^1H spectral region of the biomolecule is saturated in the “on” resonance experiment (e.g. the methyl ^1H that resonate near 0 ppm), additional biomolecule ^1H are saturated via efficient spin diffusion that occurs in large biomolecules, and an intermolecular NOE occurs from biomolecule ^1H that are proximal to the binding site ($< 6 \text{ \AA}$) to the small molecule ^1H (Mayer & Meyer, 2001). A second experiment is performed in which a region far from the biomolecule spectral range is saturated, the “off” resonance experiment, and the difference spectrum of the “on” and “off” experiments reveals the magnetization transfer from a biomolecule to individual ligand ^1H .

In our studies we have compared relative sensitivities of the WL and STD experiments for three model ligand-biomolecule systems: ketoprofen (KET)-bovine serum albumin (BSA), tert-butylhydroquinone (TBHQ)- hemagglutinin (HA), and chloramphenicol (CAM)-ribosome (70S), with the goal of determining the optimal NMR-experiments for the characterization of ligand-biomolecule interactions in relatively large molecular weight systems.

In our work we have found that despite the higher information content, STD appears to be 3 -30 times less sensitive than WaterLOGSY. This can often be detrimental for experiments in various systems, and so we offer several ways to improve the sensitivity of STD.

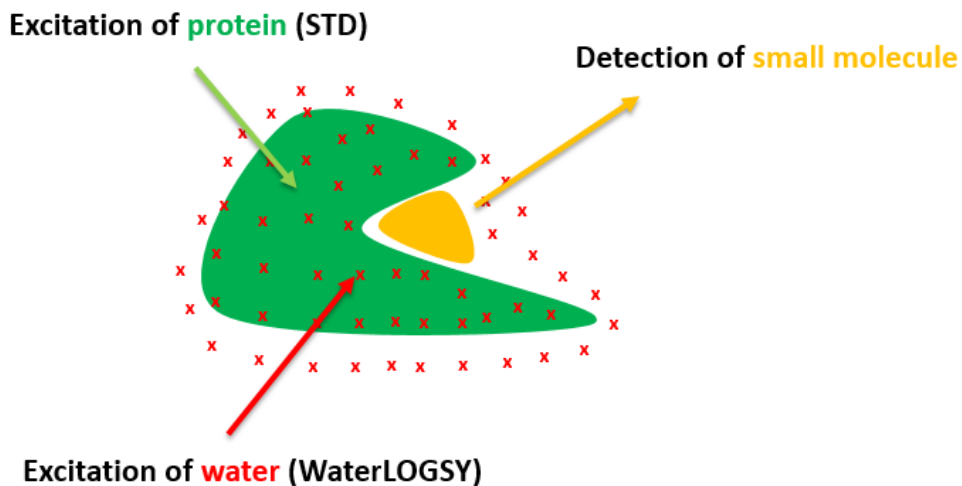


Figure 6. Schematic representation of the WaterLOGSY and STD experiments.

Chapter 1.6 - Application of virus-like particles (VLP) to NMR characterization of viral membrane protein interactions

(Adapted from Antanasijevic et al., 2016; see Appendix A)

As noted above, membrane proteins of enveloped viruses, which include Ebola, HIV, influenza, and SARS Coronavirus, play critical roles in viral entry and thus they are attractive targets for antiviral therapeutics (Kuhn et al. 2007; Lagoja and De Clercq 2008; Caffrey 2011; Yermolina et al. 2011). For example, hemagglutinin (HA) found in the viral membrane of influenza mediates virus receptor binding and entry; neuraminidase (NA) also found in the viral membrane of influenza mediates virus egress

(Skehel and Wiley 2000; von Itzstein 2007). The study of viral membrane proteins by biochemical and biophysical methods is challenging due to the presence of transmembrane domains, glycosylation, multiple disulfide bonds, and limitations of detergent usage (Skehel and Wiley 2000; Garavito and Ferguson-Miller 2001; von Itzstein 2007; Caffrey 2011).

To date, most efforts to study viral membrane proteins have utilized solubilized versions of recombinant proteins produced in mammalian or insect cells, which often require addition of stabilization domains (Stevens et al. 2006; Lee et al. 2008; Li et al. 2010; Julien et al. 2013). However, preparation of recombinant constructs is tedious and there are concerns that the recombinant protein structure may not accurately reflect the native structure due to the absence of transmembrane domains, and membrane components (i.e. lipids, carbohydrates, cholesterol and cellular proteins), and presence of stabilization domains. An alternative approach is to prepare infectious virus containing their native membrane proteins; however, there are clearly biosafety concerns with the preparation and study of infectious virus (e.g. pandemic strains of influenza, HIV or Ebola).

Recently, the use of virus-like particles (VLP) has become a very powerful tool to study the membrane proteins of many dangerous viruses without the necessity for biosafety level 3 or 4 facilities (Yonezawa et al. 2005; Zhang et al. 2008; Garcia and Lai 2011; Qian et al. 2013). In these experiments VLP are prepared by co-transfection of plasmid encoding the desired viral membrane protein with a plasmid encoding a capsid background (e.g. that of HIV or influenza), often with the addition of a reporter construct (e.g. GFP or luciferase). Current applications of viral membrane proteins embedded in VLP include studies of processing, kinetics and activity (Jacobs et al. 2005; Jalaguier et al. 2011; Ku et al. 2013; Antanasijevic et al. 2014a; Tedbury et al. 2015), drug screening trials (Wang et al. 2014; Kouznetsova et al. 2014; Basu et al. 2014), and use as immunogens (McBurney et al. 2007; Haynes 2009; Carra et al. 2015).

Recently, STD NMR has been applied to studies of interactions between small molecules and influenza membrane proteins embedded in VLP, which include interactions of a receptor analog with HA embedded in VLP (Haselhorst et al. 2008) and interactions of substrate or inhibitor analogs with NA embedded in VLP (Mohan et al. 2010; Garcia et al. 2014). Notably, the use of VLP to study viral membrane proteins obviates potential limitations of recombinant proteins due to the presence of the complete amino sequence, native processing, and native membrane components. Moreover, STD and WL are NOE-based methods and thus their sensitivities increase with increasing molecular mass and correlation times (Williamson 2009; Antanasijevic et al. 2014b). In the present work, we show the importance of VLP purity for studies of viral membrane proteins using influenza HA and NA as model systems. Moreover, we demonstrate that WL is significantly more sensitive than STD NMR for the study of VLP interactions. In addition, we compare interactions of an inhibitor with membrane-bound viral protein versus recombinant protein. Finally, we demonstrate the utility of VLP for the study of mutant viral membrane proteins by NMR-based kinetic methods.

Chapter 2 - Methods

Compounds

Ascorbic acid, propyl gallate and 2,6-di-tert-butyl-4-methylphenol, TBHQ, and TBBQ were purchased from Sigma. 2-tert-butyl-4-methoxyphenol was purchased from Fluka. 2-tert-butylphenol was purchased from Fisher. 2-tert-Butyl-4-methylphenol, 2-tert-butyl-4-ethylphenol, and 4-bromo-2-tert-butylphenol were purchased from Enamine. 3-tert-Butyl-4-methoxyphenol was purchased from USP. 2-tert-Butylanisole, 3-tert-butyl-4-methoxybenzoic acid, (3-(tert-butyl)-4-methoxyphenyl)methanol, 3-tert-butyl-4-methoxybenzamide, 3-tert-butyl-4-methoxy-N-methylbenzamide, and 3-tert-butyl-4-methoxybenzylamine were synthesized in-house. All silicone-containing compounds were synthesized in the lab of Dr. Duncan Wardrop. The purity and identity of all compounds was confirmed by 1D NMR spectroscopy.

MBX2329 and MBX2546 were kindly provided by Microbiotix Inc. or purchased from Enamine (MBX2329) and Vitas M (MBX2546). RLC was kindly provided by Dr. Lijun Rong.

Influenza pseudovirus production and characterization

For experiments with H5 HA pseudoviruses we have used a pcDNA3.1 plasmid containing H5 HA (A/Vietnam/1203/04 (H5N1)). Stratagene QuikChange II site-directed mutagenesis kit was used to generate mutant vectors that were subsequently verified by DNA sequencing. Virus-like particles were prepared by co-transfecting plasmids pcDNA3.1-H5HA (bearing wild-type or mutant H5 HA), pcDNA3.1-NA (bearing N1 influenza neuraminidase, strain A/Puerto Rico/8/1934 (H1N1)), and pNL4-3-Luc.R-E using PEI (Polysciences, Inc.) into HEK 293T cells, which were maintained in Dulbecco's medium with 10% FBS and 1% penicillin-streptomycin as previously described (Wang et al., 2012). Forty-eight hours post-transfection, the medium was harvested and filtered through a 0.45 μm filter to make the virus

stock. For Western blot analyses, virions were normalized to p24 levels (HIV-1 p24 antigen capture assay kit (SAIC Frederick); Sen et al., 2010) and were lysed by adding Triton X-100 solution to a 1 % final amount, and subsequent incubation at 37 °C for 1 h. After SDS-PAGE, transfer and blocking the membranes with 5 % milk/TBST, the blots were probed with mouse anti-H5-HA1 monoclonal antibody (BEI Resources). The secondary antibody used was peroxidase-conjugated goat anti-mouse IgG (Bio-Rad). Millipore Immobilon Western was used for visualization of the bands. The relative amount of HA on the Western blots was determined by a densitometric analysis as previously described (Sen et al., 2010).

An identical procedure was applied for generation and characterization of H7 HA and H3 HA pseudoviruses, except in these cases we have used pcDNA3.1 vector with H7 HA (A/Netherlands/219/2003) or H3 HA (A/Brisbane/10/2007), both obtained from BEI Resources. For the detection of H7 HA we have used a goat anti-H7 HA primary antibody (BEI Resources) and donkey anti-goat secondary antibody (Santa Cruz Biotechnology Inc.). As a control we also used pseudoviral particles with vesicular stomatitis virus G protein (VSVG) on the surface.

Pseudovirus entry assays

The viral entry assays were performed as previously described (Wang et al., 2012). Briefly, A549 lung cells, which were maintained in Dulbecco's medium with 10% FBS and 1% penicillin-streptomycin, were seeded to 2×10^4 cells/well of a 24-well cell culture plate in a volume of 0.5 mL. In some cases HEK293T cells were used as alternative targets and they were seeded to 1×10^5 cells/well. The following day, 500 μ L of the pseudovirus stock (H5N1, H7N1, H3N1 or VSVG) was added to each of the wells of the A549/HEK293T cells after removal of the medium. The plates were incubated at 37 °C in a CO₂ incubator. After ~6 h, the virions were aspirated and replaced with medium and the cells were allowed to rest for another 48 h. Luciferase activity was measured using the Luciferase Assay System from

Promega and a Berthold FB12 luminometer running Sirius software. In all cases, the viral entry levels fell within the linear range of detection (i.e. the values of the wild-type and mutants never exceeded 1×10^7 relative light units). Entry levels were normalized to relative p24 levels, which were determined by ELISA as previously described (Sen et al., 2010). The inhibition of entry for different compounds and antibodies was tested by pre-incubating the viruses for ~ 15 minutes with different concentrations of the inhibitor before the virus – inhibitor mixture was loaded onto the cells. IC50 value was determined from the equation: $\text{entry} = \text{entry}_{\text{max}} / (1 + ([\text{inhibitor}] / \text{IC50})^n)$, where $\text{entry}_{\text{max}}$ = entry in the absence of inhibitor and n = Hill coefficient.

Infectious virus assays

Infectious virus assays were performed in the lab of Dr. Balaji Manicassamy, as previously described (Manicassamy et al., 2008). Briefly, A549 cells were seeded at a density of 4×10^5 cells/well of a 12-well plate a day prior to infection. The next day, A549 cells were washed twice with PBS and infected with A/Hong Kong/1/1968 (H3N2) at a multiplicity of infection = 1 for 1 hour at 37 °C with shaking every 15 min. The infected cells were washed 3 times with PBS and incubated in DMEM/10 % FBS media for 3 hours at 37 °C. At 3 hpi, the cells were trypsinized and stained with an anti-NP monoclonal antibody followed by Alexa-647 conjugated secondary antibody. The cells were subjected to analysis in LSRII flow cytometer and the samples were processed using FlowJo software (TreeStar). The relative inhibition of virus infection were calculated based on DMSO treated cells.

Compound cytotoxicity assays

Compound cytotoxicity was measured using CellTiter-Glo kit (Promega). HEK293T cells were seeded in 24-well plates (1×10^5 cells/well) and on the next day incubated with medium containing

different amounts of compounds over 24 hours. Cell viability was then measured using the reagents and instructions provided with the kit. CC50 values were determined by fitting the data in OriginPro.

Large-scale VLP production and purification

HEK293T cells were grown in DMEM media with 10 % FBS and 1x penicillin/streptomycin. Cells at 70–80 % confluency were co-transfected with plasmids encoding HIV core (pNL4-3.Luc.R-E-, NIH AIDS Reagents Program) and H5 HA (strain A/Vietnam/1203/04 (H5N1), BEI Resources) and N1 NA (strain A/Puerto Rico/8/1934 (H1N1), BEI Resources). For the production of VLPs with only NA on the surface (NA-VLP) or without any viral membrane protein (native-VLP), the cells were co-transfected with HIV core and NA plasmids or just the HIV core DNA, respectively. PEI (Polysciences, Inc) was used as a transfection reagent. 48 h post transfection the cell supernatant was collected (60–80 mL), cleared through a 0.45 µm filter, and concentrated using Amicon Ultra-15 Centrifugal Filter Units (Millipore) with a 100 kDa cutoff. The concentrate was then run through a Sepharose 4 Fast Flow column (GE Healthcare) with phosphate buffer (20 mM sodium phosphate/pH 7.5 and 150 mM NaCl) used as running buffer. VLP containing fractions were combined and subsequently VLP were precipitated over a 30 % sucrose cushion (33,000 rpm for 50 min). The VLP pellet was then re-suspended in 0.5 mL phosphate buffer, concentrated further if necessary, and dialyzed overnight against phosphate buffer to remove residual sucrose. The relative purity of VLP fractions was determined by SDS-PAGE on Novex 4–12 % Bis–Tris gels (Life Technologies). For normalization purposes VLP samples were lysed with Triton X-100 (1 % final concentration) and the VLP samples (with or without dilution) were loaded onto ELISA plates pre-coated with anti-p24 or anti-H5 HA antibodies. Further manipulations were performed according to the HIV-1 p24 antigen capture assay kit (SAIC Frederick) and Hemagglutinin (H5N1)(A/Anhui/1/2005) ELISA Development Kit (Immune Technology Corp) protocols.

Hemagglutination assay

The hemagglutination assay was performed as previously described (Wang et al., 2012). For H5 HA mutant studies normalization to total HA was done using Hemagglutinin ELISA Development Kit (Immune Technology Corp.). Briefly, 60 μ L of virus or control stocks and their dilutions, purified by sucrose gradient centrifugation (Sen et al., 2010), were mixed with at different dilutions into a 40- μ L suspension of 0.5 % chicken red blood cells (Lampire Biological Laboratories) in a U-bottom 96-well plate. After 2 h of incubation at 4 °C the results were recorded.

Recombinant H5 HA production and purification

In several experiments we have used recombinant full length H5 HA, H7 HA, H3 HA and H1 HA obtained from BEI Resources. However most of the experiments with H5 HA were performed with an in-house-made construct containing H5 ectodomain and artificial trimerization domain from T4 fibrin on its C-terminus (foldon domain). In text it will be indicated which H5 HA was used. H5-Foldon was expressed in SF9 insect cells grown in SF-900 II serum free media (Life Technologies). The cells were co-transfected with a pAcGP67 plasmid containing a H5 HA (A/Vietnam/1203/ 04 (H5N1)) expression construct and BD BaculoGold linearized baculovirus DNA (BD Biosciences). The H5 HA protein construct has altered N and C-termini. The mammalian cells secretion signal (residues Met-1 to Ser-16) was replaced with the GP67 secretion signal (from the pAcGP67 vector). The transmembrane and cytosolic regions of the protein (residues Val-521 to Arg-564 were removed and replaced with an artificial trimerization domain (the foldon from T4 fibrin), and a His-tag as previously described (Stevens et al. 2006). Cell handling, transfection and protein expression were performed as recommended by the BD BaculoGold starter package kit (BD Biosciences). Viral titers were monitored using the BacPAK™ qPCR Titration Kit (Clontech Laboratories). For expression, fresh SF9 or Hi-5 cells at $2-3 \times 10^6$ cells/mL confluency were infected with H5 HA containing baculovirus solution at MOI between 2 and 6. 4 days

later the suspension was collected and the cells were removed by centrifugation. H5 HA is secreted into the insect cell media and purified by Ni-affinity chromatography. Given the low processing percentage of HA expressed in either cell line, furin protease (NEB) was used to cleave the HA0 into HA1 and HA2. After 48 hours at 4 °C, furin was inactivated using Furin Inhibitor I from EMD Millipore. The protein concentrate was then subjected to Sephacryl S300 gel filtration column with phosphate buffer (50 mM sodium phosphate/pH 8.1 and 50 mM NaCl) as a running buffer. Protein fractions were pooled and concentrated and the final yield was ~ 3 mg of protein per liter of cell culture media for SF9 cells or 6 mg of protein per liter of cell culture media for Hi-5 cells.

HA stability (fusion) assays

In the limited proteolysis experiments, ~10 μM HA (H5 or H7) was pre-incubated in the presence of small molecule inhibitors (TBHQ, MBX2329 and MBX2546) for 15 min at 37 °C (control experiments were performed with the equivalent amount of DMSO). 200 mM Phosphate-Citrate buffer stock solutions at the appropriate pH were added. The buffered solution was then incubated for 30 min at 37 °C. Next, the solutions were neutralized to pH 8.0 and incubated with 2 μg of trypsin for 30 min at 37 °C. The proteolysis was stopped by adding 11 μL of 5X SDS running buffer and heating the samples at 95 °C for 10 min. After SDS PAGE and Coomassie staining, the HA bands were quantified using Bio-Rad Image Lab 2.0.1. Subsequently, the HA band intensities were fit to $\% \text{ Native} = 100 / (1 + (I_{\text{obs}} / [H^+]_{\text{mp}})^n)$, where I_{obs} is the observed intensity at a particular pH, $[H^+]_{\text{mp}}$ is the midpoint $[H^+]$ concentration, and n = Hill Coefficient, using Kaleidagraph 4.1.3.

Alternatively, we used the fluorescence dequenching of bis-ANS (4,4'-Dianilino-1,1'-binaphthyl-5,5'-disulfonic acid dipotassium salt, purchased from Sigma Aldrich) to detect the protein unfolding at low pH. After the low pH incubation and the neutralization of solutions bis-ANS was added to a final concentration of 2 μM and its fluorescence was measured ($\lambda_{\text{exc}} = 380 \text{ nm}$, $\lambda_{\text{em}} = 480 \text{ nm}$). Fluorescence

intensity for different samples was then plotted against the pH of incubation. Experiments were performed in the presence/absence of inhibitors. The data was analyzed using OriginPro.

Differential scanning fluorimetry (thermal shift assays)

For DSF experiments we used SYPROOrange dye (Sigma). Individual samples (40 μ L in volume) were prepared with 15 μ M recombinant H5 HA, 50 μ M compounds (or DMSO in control measurements) and the SYPROOrange at 500-fold dilution (final concentrations). pH adjustment was performed by adding 200 mM phosphate-citrate buffer at the appropriate pH. Multiple variations of the experimental parameters were attempted. The effect of pH on the melting temperature of H5 HA in the presence/absence of inhibitors was measured. Compound stabilization effect was also measured with buffers of different pH (where compounds were added either before or after the low pH incubation). Once all of the samples were prepared they were loaded onto 384-well plates (Bio-Rad). We had a total of 3 wells/sample with 10 μ L/well. Protein melting curves were recorded using Applied Biosystems ViiA7 Real Time PCR system. Temperature was continuously increased from 25 $^{\circ}$ C to 95 $^{\circ}$ C at 0.075 $^{\circ}$ C/sec and SYPROOrange fluorescence was recorded. First derivative of the normalized datasets for each measurement was calculated using the AB ViiA7 software and the T_m values were determined from dF/dT vs T plots (as the temperature at which maximum of the derivative curve occurred).

Surface plasmon resonance (SPR) experiments

CM5 sensor chip was purchased from GE Healthcare and H5 HA (at 0.5 mg/mL) was immobilized using standard amine coupling with PBSP (pH 5.5) as a running buffer as previously described (Zhu et al., 2013). All measurements were performed on Biacore T200. Running buffer was: 50 mM phosphate, pH 8.3, 50 mM NaCl, 0.05 % Tween20, 2 % DMSO. MBX2329 and MBX2546 at concentrations ranging from

0 to 50 μM were loaded to the chip and the binding curves were acquired. Binding constants for MBX2329 and MBX2546 were determined from steady-state affinity curves using Excel.

WaterLOGSY and Saturation Transfer Difference (STD) NMR experiments

NMR experiments were performed on a Bruker 800 and 900 MHz AVANCE spectrometers. Details for each experiment will be specified in the result section. Sample buffer was most commonly 20 mM phosphate pH 7.4, 150 mM NaCl in 90 % $^1\text{H}_2\text{O}$, 10 % $^2\text{H}_2\text{O}$ (WaterLOGSY) or 100% $^2\text{H}_2\text{O}$ (STD). Experiments were all performed at 25 °C in 3 mm and 5 mm NMR tubes. The WaterLOGSY experiments were performed as previously described (Dalvit et al. 2011, Ramirez et al., 2013, Antanasijevic et al., 2013; Antanasijevic et al., 2014a; Antanasijevic et al., 2014b). Water was selectively saturated using a 2 msec square shaped pulse with a mixing time of 1 to 2 sec and a relaxation delay of 2.5 sec. STD experiments were performed as previously described (Meyer et al., 2003; Antanasijevic et al., 2013; Antanasijevic et al., 2014a; Antanasijevic et al., 2014b). In these experiments, protein ^1H were saturated with a train of 50 msec gaussian-shaped pulses at 100 Hz power for 1 to 2 sec with “on” resonance saturation typically at -1 ppm and “off” resonance saturation at 30 ppm (the relaxation delay was 2.5 sec before the saturating pulses). Spectra were processed by NMRPipe with a 5 Hz line broadening function and analyzed by NMRDraw (Delaglio et al., 1995) and/or Bruker Topspin 2.1. Relative % STD was defined as $100 \times \text{STD}_{\text{obs}}/\text{STD}_{\text{max}}$ where $\text{STD} = \Delta I/I_{\text{off}}$, $\Delta I = I_{\text{off}} - I_{\text{on}}$ and I_{off} and I_{on} are the intensities observed for the various resonances after the “off” and “on” presaturation of the protein. Errors in the WaterLOGSY and STD were estimated from the equation $\Delta I/I_{\text{ref}} / ((N\Delta I/\Delta I)^2 + (NI_{\text{off}}/I_{\text{ref}})^2)^{0.5}$, (as described in McCullogh et al., 2012) where $N\Delta I$ and NI_{ref} are the noise calculated by NMRDraw in the appropriate spectrum (no antibody in WaterLOGSY and I_{off} in the STD).

Antibody competition experiments

For the studies of the inhibitory properties of TBHQ against H3 HA and H7 HA (BEI resources), monoclonal antibody F49 was used (Takara Bio). Competition WaterLOGSY experiments were performed with a 2:1 ratio of F49 monoclonal antibody to H3 and H7 HA (the spectra in the presence of antibody have been corrected for any binding of TBHQ to F49). The total concentrations were 0.5 μM HA and 1 μM antibody while TBHQ was at 50 μM . 20 mM phosphate (pH 7.4) + 150 mM NaCl in 10 % $^2\text{H}_2\text{O}$ was used as a buffer. Total number of scans in the WaterLOGSY experiment was 1024. Saturation time was 2 sec with a relaxation delay of 2.5 sec.

For the studies with H5 HA inhibitors MBX2329 and MBX2546, we used a monoclonal antibody C179 (Takara Bio). For this set of experiments, the conditions were 20 μM MBX2329 or 10 μM MBX2546 with or without 0.2 μM H5 HA (BEI resources) and with or without 0.4 μM C179 in 50 mM PBS (pH 7.3), using a 900-MHz spectrometer with a mixing time of 2 sec.

WaterLOGSY and STD studies with VLP

NMR experiments were performed on Bruker 800 or 900 MHz AVANCE spectrometers equipped with room temperature or cryogenic triple resonance probes, respectively, at 25 °C. WL experiments were performed as previously described (Antanasijevic et al. 2014b). To saturate water ^1H , 2 msec square shaped pulses were used and the total saturation time was 2 sec with a relaxation delay of 2.5 sec. The number of scans was set to 1024, which corresponds to a ~2-hour experiment. Saturation transfer difference (STD) experiments were performed as previously described (Antanasijevic et al. 2014b). A train of 50 msec Gaussian pulses was used to selectively excite the protein ^1H . Total saturation time was 1 s and the relaxation delay was set to 2.5 sec. “On” resonance frequency was set to -0.5 ppm and the “off” resonance acquisition was set to 300 ppm. The total length of each STD experiment was

~13 hours. Buffer conditions were 50 mM phosphate/pH 8.2, 50 mM NaCl and 10 % $^2\text{H}_2\text{O}$ for WL or 100 % $^2\text{H}_2\text{O}$ for STD. 3 mm NMR tubes were used in all studies. Data were processed and analyzed using NMRDraw (Delaglio et al. 1995). Relative % STD was calculated as described in previous sections.

X-ray crystallography studies on H5 HA

After the Ni-affinity chromatography step of H5 HA purification thrombin (Sigma, final concentration ~ 10-50 ng/mL) and furin (NEB, final concentration ~ 10-20 units/mL) were added to the sample that will be used for crystallography. Furin cleaves the residual HA0 and thrombin removes the foldon trimerization domain. Furin inhibitor I (EMD Millipore) and thrombin inhibitor cocktail (both at the final concentration ~ 10 μM) were added to the sample to stop the reaction and H5 HA was then run on the Sephacryl S300 gel filtration column with 50 mM phosphate pH 8.2 + 50 mM NaCl as the running buffer. After purification, H5 HA was concentrated to ~ 8 mg/mL and used for crystallization. Initial crystallization trials were done for H5 HA alone and in complex with MBX2329 and MBX2546, using JSSG+, Protein Complex and PEGs suites. Multiple hits were observed and optimized for hanging drop vapor diffusion method. Diffraction datasets were collected at the stations of Life Sciences Collaborative Access Team at the Advanced Photon Source, Argonne, Illinois. Crystal structures were obtained for H5 HA alone under several different conditions, H5 HA – MBX2546 complex and H5 HA – RLC complex. MBX2329 was not observed in any of the datasets collected. Initial data processing was done using XDS program package (Kabsch, 2010). Molecular replacement and structure refinement were done in CCP4 (Winn et al., 2011) and Phenix (Adams et al., 2010), and all manual refinement was performed with Coot (Emsley et al., 2010)

The structure of H5 HA in complex with MBX2546 was collected from crystals grown in reservoir containing 100 mM Tris, pH 8.5 + 22 % PEG 6000. The drops were initially set up by mixing 1 μL of complex solution of 8 mg/mL H5 HA + 150 μM MBX2546 and 1 μL of precipitant solution, 100 mM Tris,

pH 8.5 + 16 % PEG 6000. For crystal freezing we used the following cryo-solution: 100 mM Tris pH 8.5 + 20 % PEG 6000 + 20 % Glycerol + 150 μ M MBX2546. Molecular replacement was performed using PDB entry 2FK0 as a search model. Given that the identical strain and construct of H5 HA was used to the one in the model, there was no need for sequence corrections. J-Ligand was applied to generate structure files and restraints for the MBX2546 and the ligand was then introduced in the complex structure using Coot. Data collection and refinement statistics will be shown in the results section.

The structure of H5 HA in complex with RLC was collected from crystals grown in reservoir containing 100 mM Tris, pH 8.5 + 20 % PEG 6000 + 10 % Glycerol. The drops were initially set by mixing 1 μ L of 8 mg/mL H5 HA solution and 1 μ L of reservoir solution. To make the H5 HA – RLC complex the crystals were soaked in a cryo solution containing 100 mM Tris, pH 8.5 + 20 % PEG 6000 + 20 % Glycerol + 5 mM RLC. For molecular replacement we have used PDB entry 4FQI as a search model. J-Ligand was applied to generate structure files and restraints for RLC and the ligand was then introduced in the complex structure using Coot. For comparison, crystal structure was also obtained under the same conditions for H5 HA alone. Data collection and refinement statistics will be shown in the results section.

For the pH-based experiments we used crystals obtained under the following reservoir conditions: 100 mM Cacodylate buffer, pH 6.5 + 200 mM NaCl + 2 M $(\text{NH}_4)_2\text{SO}_4$ + 10 % Glycerol. The drops were initially set by mixing 1 μ L of 8 mg/mL H5 HA solution and 1 μ L of reservoir solution. For crystal freezing we used the cryo-solution containing 100 mM Cacodylate buffer + 200 mM NaCl + 2 M $(\text{NH}_4)_2\text{SO}_4$ + 20 % Glycerol. 4 versions of this solution were made with the only difference in the final pH value (pH 7.0, pH 6.5, pH 6.0, pH 5.5). The crystals were soaked in appropriate cryo-solutions for 10 min before freezing and data acquisition. For molecular replacement PDB entry 2FK0 was used. Datasets for each pH of the cryo solution were refined separately.

All experiments were performed under the guidance of Dr. Arnon Lavie and with significant contribution in resources from the Lavie lab.

Neuraminidase activity assays

Fluorescent neuraminidase substrate, MUNANA (Sigma), was used to measure the catalytic properties of recombinant NA and NA-expressing VLP (for WT and the H274Y mutant). Briefly, different amounts of MUNANA substrate were mixed with NA samples and the fluorescent product buildup was monitored by measuring fluorescence at $\lambda_{\text{exc}} = 365$ nm, $\lambda_{\text{em}} = 445$ nm. Initial reaction rates were calculated for different substrate concentrations and the K_m was estimated from Michaelis-Menten plots. The competitive inhibitor of NA activity, Neu5Ac2en (DANA), was used to confirm the specificity of NA for its substrate.

NA catalyzed reactions were also followed using 1D NMR experiments by measuring the line intensities for the substrate MUNANA resonance at 2.50 ppm. Experimental conditions were ~ 10 nM NA or H274Y-NA in VLP, 20 mM phosphate, pH 7.4, 150 mM NaCl, and 1 mM CaCl_2 at 25 °C in the presence and absence of different amounts of MUNANA (substrate). OriginPro (OriginLab Corp) was used to determine the kinetic parameters (K_m) and inhibitory constant K_i .

Molecular Docking

Molecular docking was applied to predict the structures of H5 HA complexes with MBX2329 and MBX2546 based on the C179 binding site on the surface of H5 HA. The apo crystal structure of the H5 (PDB code 2FK0) was considered for the modeling studies. The SITE-ID module of the Tripos molecular modeling package (SybylX 1.3; Tripos International) was used to identify the potential small molecule ligand binding sites in the crystal structure. The FlexiDock docking package of Tripos was used to preposition the MBX2329 and MBX2546 ligands in the possible ligand binding sites. FlexiDock works in

torsional space, keeping the bond lengths and the angles constant while allowing the amino acids interacting with the ligand to be flexible during the docking process. The energetically most favorable position and the poses of MBX2329 and MBX2546 obtained from FlexiDock were considered for further modeling studies. The molecular dynamics simulations (MDS) in the Optimized Potentials for Liquid Simulations (OPLS2005) force field was used to carry out the MDS of the H5 and MBX2329/MBX2546 complex structures. All MDS computations were carried out in MacroModel9.8 implemented in Schrodinger software suite (MacroModel, 9.8, Schrodinger LLC) in one NPT ensemble (constant pressure and temperature). In the MacroModel dynamics panel, stochastic dynamics were chosen as it includes random forces that stimulate the buffering of a system by solvent molecules. To constrain the bond lengths to the original values, the "SHAKE" option was selected. The simulation of the complex was carried out at 300 K with a time step of 1.5 fs and equilibrium time of 1 ps. The MD simulations were run for 1, 5, and 10 ns recording the energies and the trajectories of the system. The plot of the potential energy versus the time at 10 ns revealed that the system had attained an equilibrium condition.

Molecular docking was also applied to predict the structures of H7 HA complexes with TBHQ and several TBHQ daughter compounds. H7 HA structure used was 4R8W, and the initial TBHQ positioning was based on the crystal structure with H3 HA (3EYM). MD simulations were performed as described previously for H5 HA and MBX2329/MBX2546.

All simulations were performed by Dr. Rama Mitra at the Center for Molecular Innovation and Drug Discovery, Northwestern University.

CORCEMA simulations

To calculate the relative STD signal as a function of correlation time and target protein concentration, we used the program CORCEMA-SX 3.8 (Jayalakshmi and Krishna, 2002) and our

previously published model of the HA-MBX2329 complex (Antanasijevic et al. 2014a). HA concentrations examined were 30 nM (the concentration of HA in the VLP experiments), 300 nM, 3000 nM and 30,000 nM (the concentration of HA in the recombinant HA experiments) with 100 μ M MBX2329 (ligand). The other input parameters included: 10 Å cutoff distance, 100 % $^2\text{H}_2\text{O}$, $K_d = 5 \mu\text{M}$, $k_{on} = 1 \times 10^9 \text{ s}^{-1}$, free ligand $\tau_{sc} = 0.5 \text{ nsec}$, 900 MHz field strength, saturation time = 1 s, and instantaneous irradiation of Ile, Leu and Val methyl groups.

Chapter 3 - Results

Chapter 3.1 - Characterization of the stem-loop region by mutagenesis

(Adapted from Antanasijevic et al., 2014a; see Appendix A)

We have used H5 HA as a model system to test the importance of the stem-loop region in hemagglutinin for viral entry. The stem loop is comprised of HA2 residues 40–110 (H3 numbering). In addition, we noted that residues 22–35 of HA1 and 17–25 of HA2 also make contacts in this region. Accordingly, we prepared 18 site-directed mutants at 14 different positions to probe the function of the stem loop region in H5 HA. The location and degree of conservation among diverse Groups 1 and 2 HA is shown in Figure 7.A. Mutations to positions Thr41, Gln42, Ile45, Asn53, and Leu99 of HA2 are highly conserved and designed to assay the importance of these residues to HA function. Mutations to positions Asp26, Ile28, and Met31 of HA1 and Thr49, Val52, Ser54, Ile55, Asp57, and Met102 of HA2 are less conserved and designed to assay differences between Group 1 (i.e. H1 and H5) and Group 2 (i.e. H3 and H7) HA. The location of the mutated side chains with respect to the HA structure is shown in Figure 7.B with HA1 colored blue and HA2 colored red. For clarity, only one monomer of the symmetric trimer is shown. Note that residues range from being highly solvent exposed to being relatively buried and that the mutated residues are involved in a variety of intra and intermolecular contacts, which will be discussed below. For full sequence alignment between H1, H3, H5 and H7 HA see Appendix B.

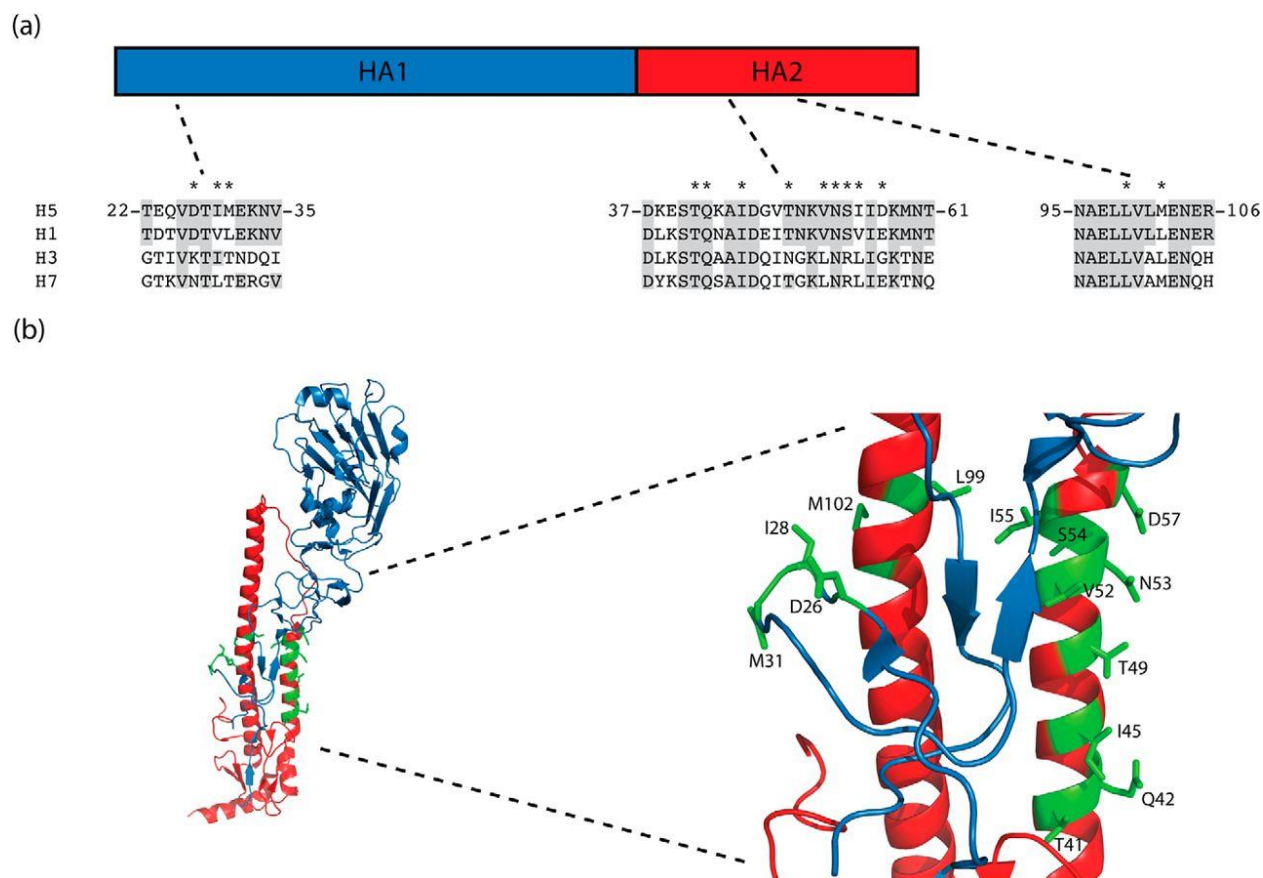


Figure 7. Location of mutant sites within H5 HA. (A) Sequence alignment of Group 1 (H5 and H1) and 2 (H3 and H7) HA strains. Conserved residues are shaded gray. The sites of site-directed mutations are denoted by asterisks. Numbering corresponds to H3 HA. (B) Location of mutant sites in the structure of H5 HA. The HA1 subunit is shown in blue and the HA2 subunit is shown in red. The side chains of substituted residues are shown in green. For clarity, only one monomer of the symmetric trimer is shown.

We first assessed the mutational effects on protein expression, processing (i.e. cleavage of HA0 to HA1 and HA2), and incorporation into virions using a Western blot analysis of wild-type and mutant virions. The results of this analysis are shown in Figure 8.A using a monoclonal antibody to HA1, which detects processed HA1 and unprocessed HA0, and summarized in Table II. In the case of the wild-type, both HA0 and HA1 are observed with the majority of the HA found in virions observed to be processed (~85%). In the case of the mutants all mutants exhibited >50% HA processing. On the other hand, mutants HA1-D26K, HA1-M102L, HA2-V52A, and HA2-I55A exhibit significantly reduced levels of total HA (<30% of the wild-type HA levels), suggesting that they have significantly reduced the expression and/or incorporation of HA into virions. In contrast, all other mutants exhibit HA levels that are similar to the wild-type, suggesting that the mutation has not significantly affected HA expression, processing, and incorporation into virions. Next, we used the hemagglutination assay to assess mutational effects on the HA1 conformation and the ability to bind the receptor. In this assay, virion preparations are added to red blood cells (RBC) placed at the bottom of the well and binding of virions to RBC is then visualized as the agglutination of the RBC. As shown in Figure 8.B (and summarized in Table II) all virion preparations cause agglutination of the RBC with mutants HA1-I28A, HA1-I28V, HA1-M31A, HA2-T41A, HA2-Q42A, HA2-I45A, HA2-V52A, HA2-N53A, HA2-S54R, HA2-I55A, HA2-I55V, HA2-D57E, HA2-L99A, and HA2-M102A exhibiting wild-type titers (agglutination observed up to ~1:16 dilution) and HA1-D26K, HA2-T49A, and HA2-M102L exhibiting lower titers (agglutination observed up to ~1:4 dilution). Thus, with the possible exceptions of mutants HA1-D26K, HA2-T49A, and HA2-M102L, the mutant HA are competent to bind to their receptor and have presumably not disrupted the HA1 structure.

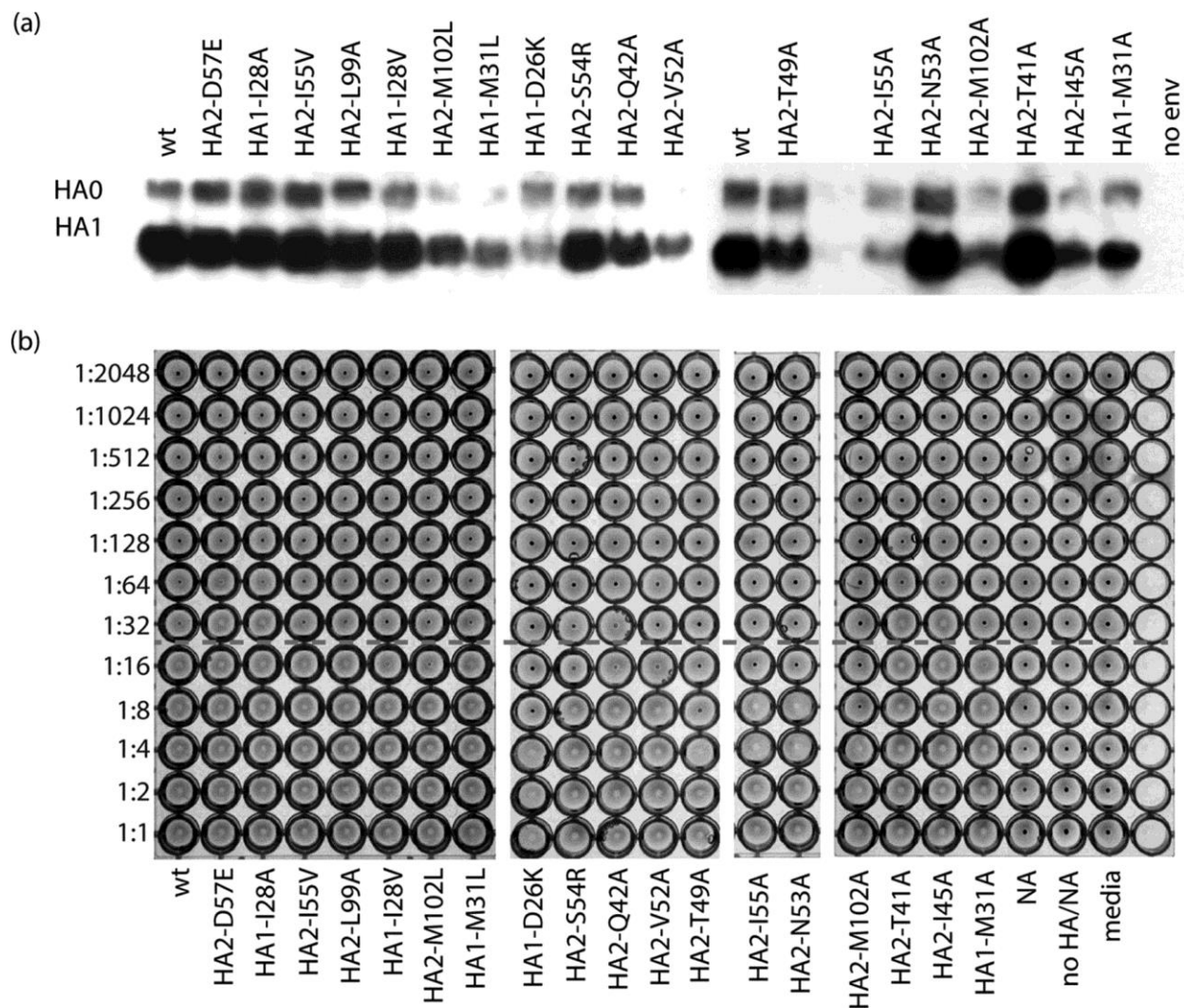


Figure 8. Western blot and hemagglutination assay of virus-like particles of H5 HA wild-type and mutants. (A) Western blot analysis of HA in virus-like particles with no env corresponding to virions without HA and NA. Note that the primary antibody used is against HA1 and thus detects both HA0 and HA1. (B) Hemagglutination assay of virus-like particles with “NA” and “no HA/NA” samples corresponding to virions prepared with only NA and without NA or HA, respectively. Each assay was performed in triplicate.

TABLE II

Summary of the mutational effects to influenza H5 HA

Mutant ^a	WT entry	HA expression ^b	HA processing ^c	Hemagglutination ^d
		%		
WT	100 ± 1	100	85	1:16
HA1-D26K	0.10 ± 0.07	28	50	1:4
HA1-I28A	4.4 ± 0.8	100	73	1:32
HA1-I28V	23 ± 3	83	79	1:16
HA1-M31A	2.8 ± 1.3	56	74	1:16
HA1-M31L	51 ± 13	27	96	1:16
HA2-T41A	17 ± 9	150	69	1:32
HA2-Q42A	14 ± 2	62	77	1:8
HA2-I45A	7.4 ± 1.1	39	84	1:32
HA2-T49A	19 ± 5	71	64	1:4
HA2-V52A	51 ± 12	20	100	1:8
HA2-N53A	2.1 ± 1.5	130	75	1:8
HA2-S54R	47 ± 5	82	79	1:8
HA2-I55A	0.7 ± 0.9	27	56	1:8
HA2-I55V	67 ± 5	120	74	1:16
HA2-D57E	33 ± 7	100	75	1:32
HA2-L99A	5.8 ± 1.2	97	73	1:16
HA2-M102A	11 ± 3	37	75	1:4
HA2-M102L	22 ± 9	43	93	1:8
No env	0.90 ± 0.30			

^a - Numbering according to H3 HA.

^b - % HA expression with respect to the wild-type.

^c - % Processing with respect to total HA.

^d - Largest dilution at which agglutination was observed.

Previously, we and others have shown that the VLP containing envelope proteins on an HIV background vector are useful surrogates to characterize functional properties of envelope proteins from diverse viruses including influenza, HIV, Ebola, and SARS-CoV (Basu et al., 2014; Jacobs et al., 2005; Guo et al., 2009; Jiang et al., 2009;). In Figure 9. (and summarized in Table II) we show the relative entry of virions containing wild-type or single site mutations into A549 lung cells. First note that all single-site mutations exhibit decreased entry with respect to the wild-type, even those with relatively conservative substitutions (e.g. HA2-T49A or HA2-D57E). For ease of discussion we have divided the effects into 3 classes: non-functional (<1% entry), impaired (1–25%), and intermediate (>25%). Interestingly, there are only 2 mutants that fall into the non-functional category: HA1-D26K and HA2-I55A. Presumably, the very low entry levels of these mutants is due in part to their significantly low levels of expression and/or incorporation into virions. Mutants that exhibit impaired (but measurable) entry include: HA1-I28A, HA1-I28V, HA1-M31A, HA2-T41A, HA2-Q42A, HA2-I45A, HA2-T49A, HA2-N53A, HA2-L99A, HA2-M102A, and HA2-M102L. Finally, mutants that exhibit the least effects on entry include: HA1-M31L, HA2-V52A, HA2-S54R, HA2-I55V, and HA2-D57E. Taken together, the mutational effects on entry underscore the importance of this part of the stem loop region to HA-mediated entry.

Furthermore, we decided to investigate whether these mutants can be used to disrupt the binding sites of fusion inhibitors that bind in the region. Previously, the monoclonal antibody C179 has been shown to neutralize the entry of influenza virus by binding to the HA stem loop region and stabilizing the neutral pH conformation (Sakabe et al., 2010). Additionally, a crystal structure of the antibody with H2 HA is available in the literature (Dreyfus et al., 2013) and thus the exact binding surface for C179 – HA interaction is known. Accordingly, we were interested in testing whether our stem loop region mutants would affect the binding and entry inhibition of C179. In this case we used the viral entry assay under conditions where wild-type HA is only partially inhibited (Figure 10.). For this analysis mutants HA1-D26K and HA2-I55A were excluded due to their very low entry levels in the absence of

entry inhibitor (Figure 9. and Table II). The relative entry levels in the presence of C179 (at 0.05 $\mu\text{g}/\text{mL}$) were calculated by normalizing to the entry levels in the absence of the C179 for each individual mutant. As shown in Figure 10, under these conditions C179 reduced wild-type entry to $29 \pm 3 \%$. Mutants HA2-T41A, HA2-Q42A, HA2-T49A, HA2-V52A, HA2-N53A, HA2-S54R, HA2-D57E, HA2-M102A, and HA2-M102L exhibit entry inhibition that is similar to the wild-type ($< 20 \%$ different), suggesting that their stem loop structures are competent to bind the antibody. In contrast, HA2-L99A is more sensitive to entry inhibition by C179 (> 3 times more sensitive), suggesting that the mutation enhances antibody binding and/or mode of action. Interestingly, mutants HA1-I28A, HA1-M31A, HA1-M31L, HA2-I45A, and HA2-I55V render HA less sensitive to entry inhibition by C179 (> 2 times less sensitive) suggesting that the mutation decreases antibody binding and/or mode of action.

The locations of activity-altering mutations are shown in Figure 11. In this representation, we have considered the outer face (i.e. solvent exposed) and inner face (i.e. contact region with other subunits) of a single HA monomer. The red, blue, and green coloring scheme corresponds to negative, minimal, and enhanced effects (respectively) on HA-mediated entry or inhibition by C179. By minimal effects we considered every entry result that was within two-fold range of the WT. The antibody binding site (based on Dreyfus et al., 2013) is shown in yellow.

We demonstrate that there is a great correlation between residues predicted to affect the binding site and inhibitory activity of C179 (based on the crystal structure) and residues determined here via mutagenesis. These results are somewhat expected as the C179 antibody is very well characterized in the literature. Nevertheless, the experiments clearly demonstrate the applicability of this type of approach for testing the binding sites of novel, non-characterized inhibitors.

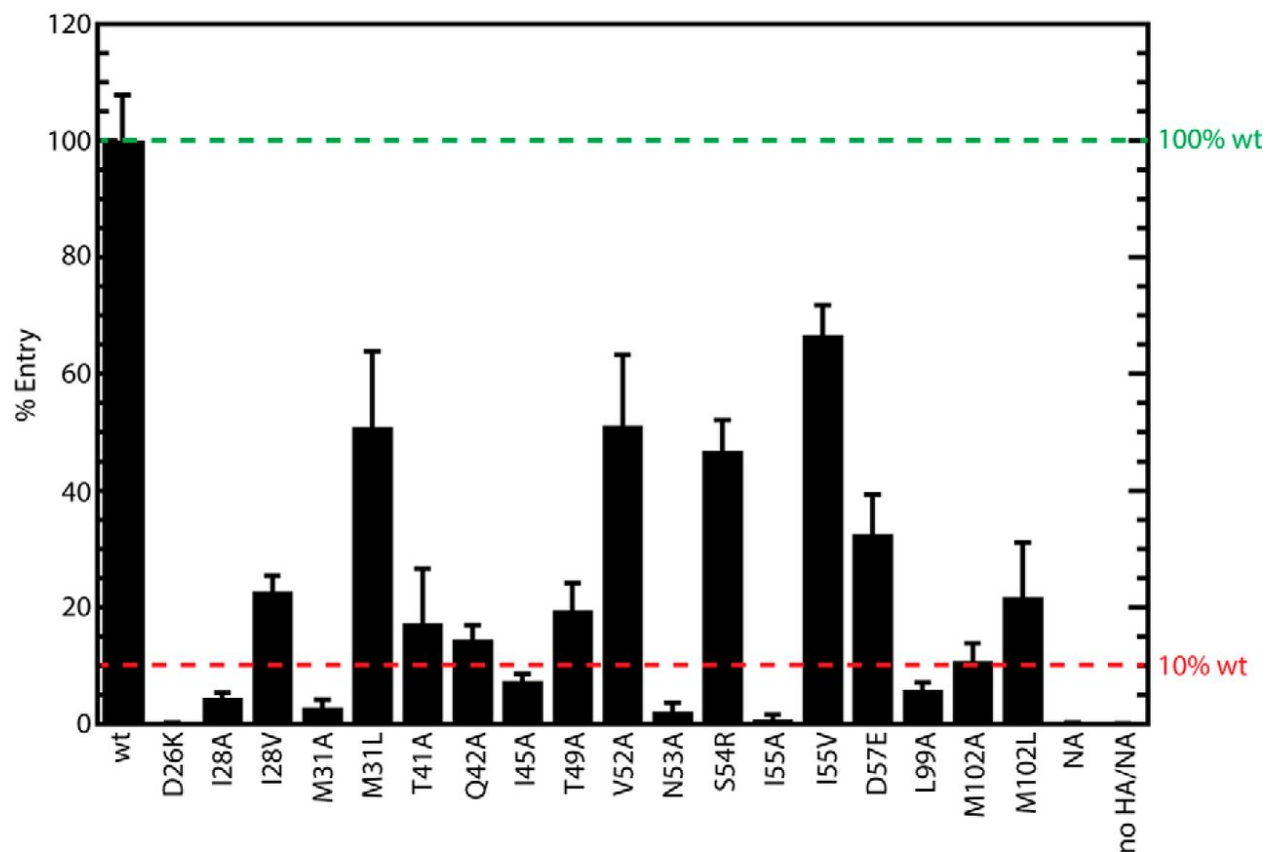


Figure 9. HA-mediated entry of H5 HA wild-type and mutant virions. The relative entry levels are based on the entry of pseudovirus into A549 lung cells using a luciferase-based assay. Each experiment was performed six times from the transfection step.

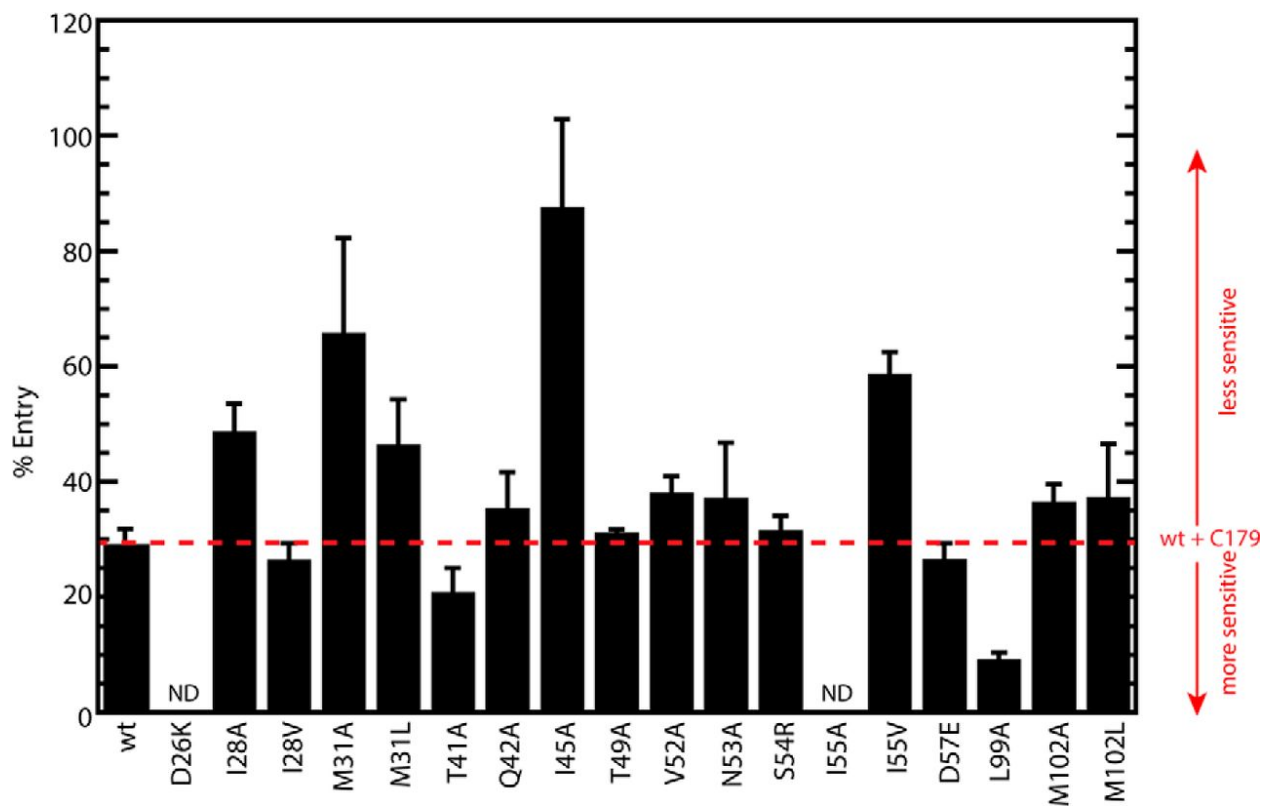


Figure 10. Mutant effects on entry inhibition of H5 HA by monoclonal antibody C179. The relative entry levels are based of the entry of pseudovirus into A549 lung cells in the presence of C179 (concentration = 0.05 $\mu\text{g}/\text{mL}$) and absence of it. Each experiment was performed in triplicate.

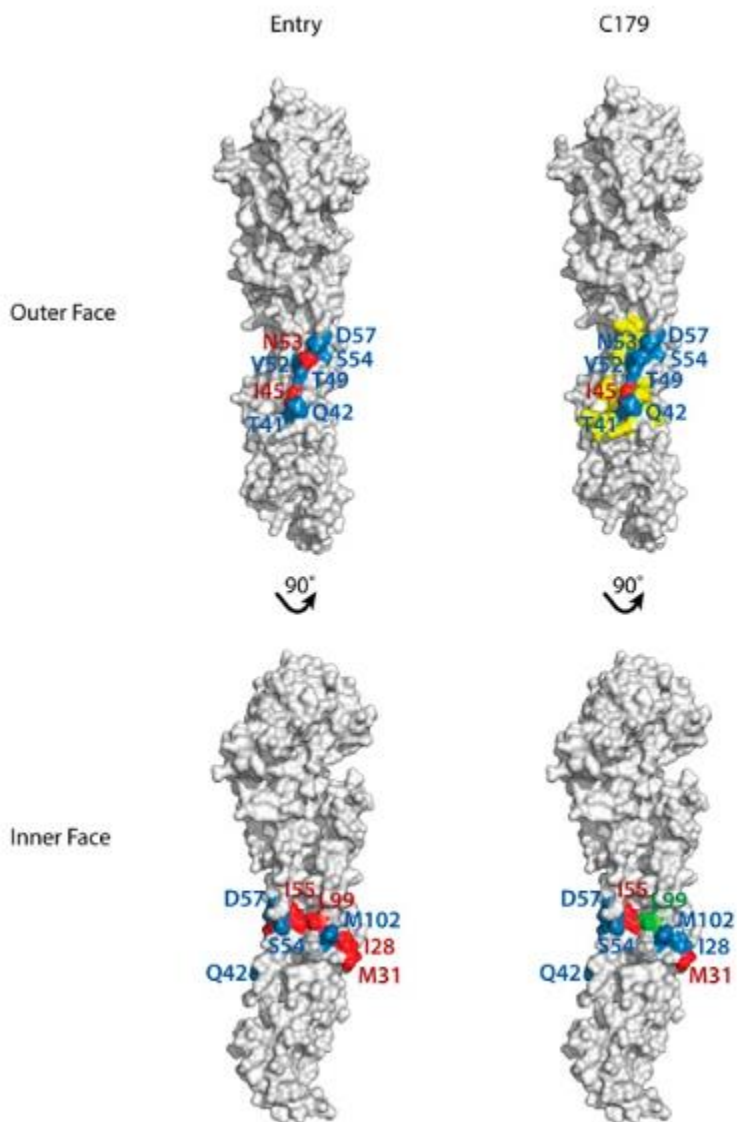


Figure 11. Space-filling representation of the mutational effects on H5 HA entry and entry inhibition. For clarity, only one monomer of the trimer is shown. The outer face represents the solvent-exposed region and the inner face, achieved by a 90° rotation about the y axis, represents the site of interaction with the other subunits. In the case of the C179 results, the antibody binding site is denoted in yellow. See the text for color coding of mutational effects.

Chapter 3.2 - Studies on the mechanism behind the early and intermediate steps of the fusion process

In order to learn more about how the fusion process is regulated in HA and what the role of the stem-loop region in this process is, we decided to apply x-ray crystallography. Studying the late stages of fusion is very difficult given the short lifetime of these states and solubility issues with recombinant protein systems (Ni et al., 2014; Remeta et al., 2002; Garcia et al., 2015). The structures of HA in post-fusion state are available for H2 HA (Xu et al., 2011), H3 HA (Bullough et al., 1994) and influenza B HA (Ni et al., 2014). In all three cases the structures are determined only for the ectodomain of HA2 (without C-terminus and without HA1), raising concerns about how representative these structures are of the intact, full-length HA.

Nevertheless, the majority of the fusion inhibitors target and interact with the stem-loop region only in conformations at neutral and intermediate pH values (before any large structural changes take place). In fact, most of them are believed to work by blocking early steps of the fusion process. A better understanding of these early, reversible states will provide more insight into the processes that precede the onset of fusion and the residues that regulate them. Additionally, these findings would be very useful when it comes to determination of the mechanism of action for different types of fusion inhibitors. A better understanding of how entry inhibitors work facilitates and speeds up the chemical optimization process.

H5 HA fusion is a multi-step process. We applied limited proteolysis experiments to help us determine the pH range at which our H5 HA undergoes the conformational change. In these assays the protein was incubated in a set of phosphate-citrate buffers of different pH for 30 min (37 °C) and upon re-neutralization trypsin proteolysis was used to determine the extent of HA that has undergone the conformational change. The data is shown in Figure 12.A. H5 HA appears to be very stable and more

than 90 % of it stays in the pre-fusion state unless the pH is lowered below pH 5.25. However, the melting points of the protein under identical conditions show strong variations across the same pH range (Figure 12.B). This data suggests that the stability of HA changes significantly as the pH is lowered and that the protein most likely goes through a set of reversible states. At pH 6.50 and 6.00 H5 HA appears to enter a more stable state and the melting point increases by 4 - 6 °C. On the other hand, at pH 5.75 and below there seems to be a continuous decrease in stability. It should be noted that the post-fusion state of HA is not observable by this method due to its insolubility in the lack of membranes or detergents. The values determined using the assay under these conditions correspond to HA in pre-fusion conformations. However, because of the high sensitivity of SYPROOrange dye to hydrophobic protein domains, an increase in background fluorescence is observed at pH < 5.0, where relatively significant amounts of HA have reached to the post-fusion state and precipitated. The determination of T_m in these samples is more challenging.

Interestingly, the increased stability of the pH 6.0 – 6.5 forms may play a role in favoring the final conformation. The neutral pH conformation is thought to be metastable (Skehel et al., 2000; Bullough et al., 1994), and the intermediate states may be expected to reduce the transition energy necessary to convert to the low pH conformation.

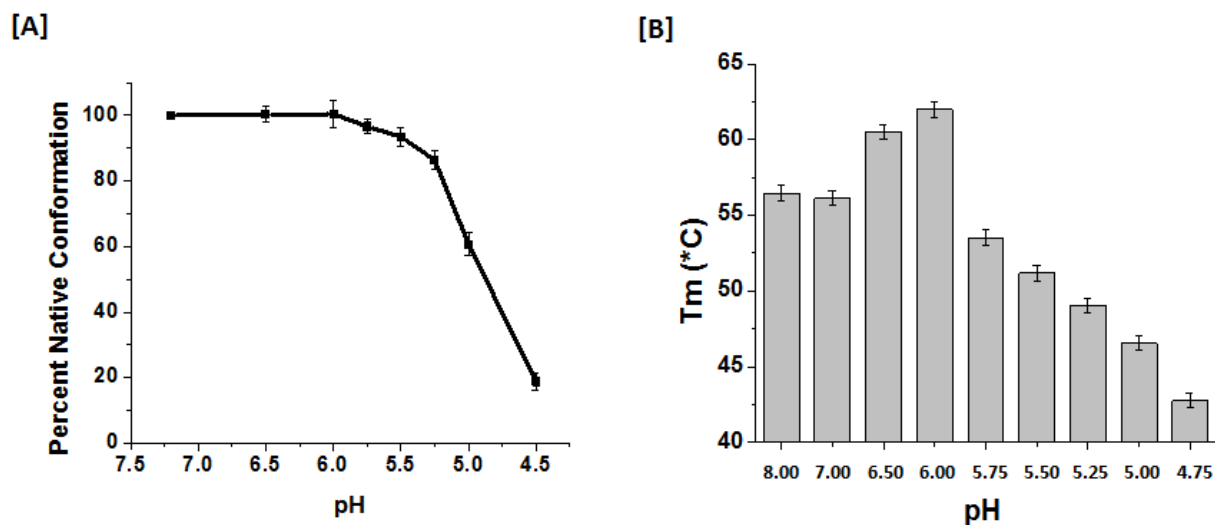


Figure 12. The studies of H5 HA stability as a function of pH. (A) Limited proteolysis experiments showing the amount of H5 HA that undergoes the conformational change after 30 min incubation at different solution pH; (B) Thermal shift assay results showing H5 HA melting point at different solution pH.

To help us learn more about the intermediate states in fusion we have crystallized H5 HA using two different conditions: (1) 100 mM Cacodylate buffer, pH 6.5 + 200 mM NaCl + 2 M $(\text{NH}_4)_2\text{SO}_4$ + 10 % Glycerol and for comparison (2) 100 mM Tris, pH 8.5 + 20 % PEG6000 + 10 % Glycerol. Crystallization and data processing was performed as described in the methods section and the final statistics are shown in Table III.

TABLE III

Data collection and refinement statistics for H5 HA under different conditions

Structure	H5-F (pH 8.5)	H5-F + RLC	H5-F + MBX2546
Data collection statistics			
X-ray source and detector	LS-CAT (ID-D) MAR CCD 300	LS-CAT (ID-G) MAR CCD 300	LS-CAT (ID-D) MAR CCD 300
Wavelength (Å)	1.008	0.979	1.008
Temperature (K)	100	100	100
Resolution (Å)	2.00	2.20	2.80
Number of Reflections			
Observed	944,212 (141,613)	608,789 (91,468)	703,724 (135,456)
Unique	154,261 (23,314)	110,799 (17,093)	57,267 (10,577)
Completeness (%)	98.8 (93.7)	94.1 (91.2)	99.8 (100.0)
R _{meas} (%)	9.5 (83.3)	9.2 (71.4)	28.9 (120.5)
Average I/σ(I)	13.42 (2.51)	12.28 (2.34)	8.62 (2.10)
Space group	P2 ₁ 2 ₁ 2 ₁	P2 ₁ 2 ₁ 2 ₁	P2 ₁ 2 ₁ 2 ₁
Unit cell (Å): a, b, c	72.82, 126.50, 249.33	72.71, 126.08, 249.64	68.71, 131.03, 253.32
(°): α = β = γ	90.00	90.00	90.00
Refinement statistics			
Refinement program	REFMAC5	REFMAC5, J-Ligand	REFMAC5, Phenix 1.10, J-Ligand
R _{cryst} (%)	19.62	18.93	22.72
R _{free} (%)	23.13	24.04	27.50
Resolution range (Å)	30.00 - 2.00	30.00 - 2.20	30.00 - 2.80
Protein molecules per a.u.	6	6	6
Number of atoms:			
Protein			
(ChainA, ChainB)	(2588, 1412)	(2608, 1412)	(2561, 1352)
ChainC, ChainD	2595, 1416	2615, 1416	2561, 1363
ChainE, ChainF)	2581, 1412)	2601, 1412)	2521, 1338)
Water molecules	851	741	91
Ligands	-	60	27
Sulfate molecules	-	-	-
RMSD from ideal:			
Bond length (Å)	0.0181	0.0155	0.0132
Bond angles (°)	1.8847	1.7280	1.7067
Average B-factors (Å²)			
Protein			
(ChainA, ChainB)	(37, 48,	(47, 62,	(78, 112,
ChainC, ChainD)	35, 51,	44, 68,	74, 124,
ChainE, ChainF)	41, 69)	49, 85)	94, 158)
Water molecules	44	49	60
Ligands	-	83	209
Ramachandran plot (%):			
most favored regions	94.65	95.33	86.55
additionally allowed regions	4.74	3.79	9.60
outlier regions	0.61	0.88	3.85

TABLE III (continued)

Data collection and refinement statistics for H5 HA under different conditions

Structure	H5-F (pH 5.5)	H5-F (pH 6.0)	H5-F (pH 6.5)	H5-F (pH 7.0)
Data collection statistics				
X-ray source and detector	LS-CAT (ID-G) MAR CCD 300			
Wavelength (Å)	0.979	0.979	0.979	0.979
Temperature (K)	100	100	100	100
Resolution (Å)	2.30	2.10	2.40	2.82
Number of Reflections				
Observed	260,754 (37,761)	356,742 (53,484)	345,944 (51,268)	161,037 (21,885)
Unique	43,303 (6,554)	55,355 (8,604)	37,825 (5,929)	24,399 (3,544)
Completeness (%)	99.1 (94.7)	99.4 (96.9)	99.5 (98.6)	98.2 (90.1)
R _{meas} (%)	8.7 (78.5)	6.3 (81.9)	16.3 (176.4)	16.6 (139.7)
Average I/σ(I)	11.78 (2.09)	14.59 (2.04)	12.29 (2.57)	14.79 (1.54)
Space group	H32	H32	H32	H32
Unit cell (Å): a, b, c (°): α, β, γ	109.38, 109.38, 421.03 90.00, 90.00, 120.00	108.54, 108.54, 419.79 90.00, 90.00, 120.00	108.06, 108.06, 419.82 90.00, 90.00, 120.00	109.55, 109.55, 421.56 90.00, 90.00, 120.00
Refinement statistics				
Refinement program	REFMAC5, Phenix 1.10	REFMAC5, Phenix 1.10	REFMAC5, Phenix 1.10	REFMAC5, Phenix 1.10
R _{cryst} (%)	19.15	19.69	21.39	21.96
R _{free} (%)	23.29	24.91	26.34	29.35
Resolution range (Å)	30.00 – 2.30	30.00 – 2.10	30.00 – 2.40	30.00 – 2.82
Protein molecules per a.u.	2	2	2	2
Number of atoms:				
Protein (ChainA, ChainB)	(2617, 1371)	(2617, 1371)	(2627, 1366)	(2617, 1371)
Water molecules	134	153	117	76
Ligands	-	-	-	-
Sulfate ions	5	5	3	2
RMSD from ideal:				
Bond length (Å)	0.017	0.017	0.014	0.013
Bond angles (°)	1.987	2.067	1.871	1.809
Average B-factors (Å²)				
Protein (ChainA, ChainB)	(68, 69)	(66, 67)	(62, 65)	(71, 75)
Water molecules	60	65	52	51
Sulfate ions	96	102	96	107
Ramachandran plot (%):				
most favored regions	94.46	93.84	92.55	91.79
additionally allowed regions	4.52	4.93	5.38	6.16
outlier regions	1.03	1.23	2.07	2.05

The analysis of the two structures of H5 HA (and HA structures available in PDB database) reveals some very interesting properties of the pH 6.5 structure. The fusion peptide (residues 1-12 on HA2) that is usually hidden inside the trimer cavity because of its hydrophobic nature, is well exposed and facing towards the outside of the molecule extending over the side-chains of β -sheet residues on HA1-HA2 interface (amino acids HA1: Q12 – Y17 and HA2: G136 – F140) as shown in Figure 13. This repositioning of the fusion peptide has been observed only in a few other cases for H3 HA (Iba et al., 2014) and H17 HA (Sun et al., 2013; Zhu et al., 2013). The common factor in these studies was the slightly acidic pH of the crystallization buffer (pH 6.5 or lower). This finding is in excellent agreement with the results of dynamics studies on H3 HA performed under different buffer conditions (Garcia et al., 2015). Using HD exchange at neutral to intermediate pH values the authors show that one of the very first changes happening in HA during fusion is a great increase in the solvent exposure and dynamics of the fusion peptide. In fact, at intermediate and low pH, fusion peptide becomes one of the most dynamic parts of the protein. The results strongly support the model in which fusion peptide relocalization is the major driving force behind the early stages of HA fusion. Based on these findings the change in conformation of the fusion peptide observed in the pH 6.5 crystal structure (and other low pH structures) is most likely a real effect and not a crystal packing artefact. However the extent to which crystal lattice is affecting the fusion peptide conformation is not clear. It should be noted that the first 4 amino acids of the fusion peptide are not present in the density indicating very dynamic behavior, which is in agreement with the HD exchange experiments (Garcia et al., 2015).

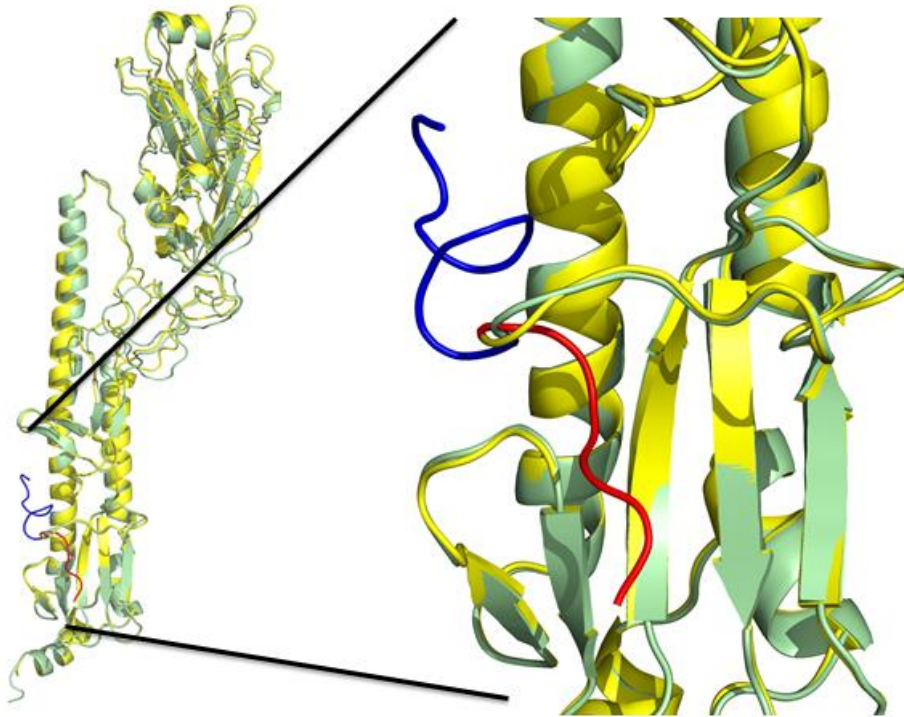


Figure 13. Relocalization of the fusion peptide at pH 6.5. The overlay of the H5 HA monomer structures at pH 8.5 (light green) and pH 6.5 (yellow) is shown on the left. Enlarged fusion peptide region is on the right. FP in pH 8.5 and pH 6.5 structures is highlighted in blue and red, respectively.

An in depth comparison between the pH 6.5 structure of H5 HA and the other H5 HA structures at neutral or slightly basic pH (including our own pH 8.5 structure) revealed many additional small-scale changes in the orientation of side chains of amino acids. To better understand and assess this observation we determined the crystal structures of H5 HA using crystals from the pH 6.5 crystallization condition (100 mM Cacodylate buffer, pH 6.5 + 200 mM NaCl + 2 M $(\text{NH}_4)_2\text{SO}_4$ + 10 % Glycerol), soaked in the cryo-solutions at pH 7.0, pH 6.5, pH 6.0 and pH 5.5 for 15 min prior to freezing and data collection. The details of the experiment are described in the Methods section. This type of analysis allows us to very reliably determine small structural rearrangements that take place in H5 HA as a consequence of change in pH and under the same crystal packing restraints. The particular focus was on all charged amino acids and the changes in local environment around them. Not surprisingly given the pH range covered in our studies, the greatest perturbations were seen around histidine residues.

One location of particular interest is the His-rich region found in the stem-loop, on the interface between HA1 and HA2 subunits (also in close proximity of the fusion peptide). In group 1 HA (like H5) there are three highly conserved His residues: HA1 - H18, HA1 - H38 and HA2 - H111 (Figure 14.). It has been suggested elsewhere that upon protonation, these histidines might help facilitate the dissociation of HA1 from HA2 (Stevens et al., 2013). In our experiments we directly observe a change in conformation of H38 at pH below 7.0. In the pH 7.0 structure (as well as the other H5 HA structures available, including Tris pH 8.5 determined in our lab), H18 and H38 side chains are found in immediate proximity (nitrogen to nitrogen distance $\sim 6 \text{ \AA}$). H18 is forming a hydrogen bond with the main chain carbonyl of HA2 – M17. This interaction positions the titratable π - nitrogen towards the H38. In pH 6.0 and pH 5.5 structures, a $\sim 120^\circ$ rotation of the H38 side-chain around $\text{C}_\alpha - \text{C}_\beta$ bond is observed. It now faces away from H18 as a result of protonation in both residues. H38 is stabilized in the new conformation via electrostatic interaction with HA1 – E23. The formation of a new salt bridge between H38 and E23 might account for the increase in stability observed at pH 6.0 in the thermal shift assays (T_m

increased by ~ 6 °C). Additionally, the increase in positive charge of this site at low pH attracts a sulfate group. The structure at pH 6.5 captures the middle point of this transition. H38 chain exists in two conformers (facing towards and away from H18) at ~ 50 % occupancy in each. From the electron density, HA2 – H111 doesn't seem to induce any local rearrangements over the pH range used in our structures.

Additionally, the protonation of several other histidine residues induces local changes in occupancies of the charged amino acids surrounding them. One example is the protonation HA1 - H113 (Figure 15.). This amino acid is on the interface between HA1 and the loop linker region on HA2. The linker becomes helical at low pH, inducing full extension of the HA2 subunit and the introduction of the fusion peptide into the endosomal membrane. The importance of H113 for normal functioning of HA has already been shown elsewhere (Herfst et al., 2012; Zhang et al., 2013). This residue is in close proximity of HA2 – E69 and the interaction between them is suggested to couple the HA1 dissociation process to the loop-to-helix transition taking place in HA2. In our structure E69 appears to be very dynamic and its electron density can barely be detected in the pH 7.0 and pH 6.5 structures. However, at pH 6.0 and pH 5.5, there is a significant increase in occupancy of E69 in a conformation directly facing H113. In other words, at lower pH glutamate becomes more anchored to histidine, which is an indication of electrostatic interaction caused by protonation of histidine residue.

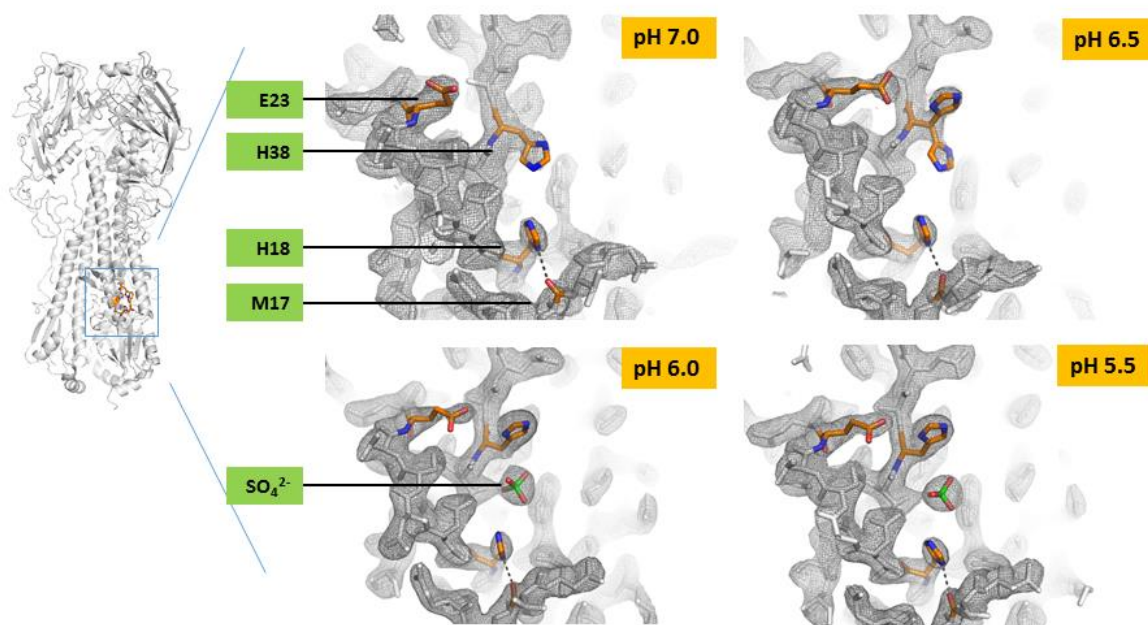


Figure 14. pH induced rotation of the side chain of H38. Structures (with electron densities) of the triple-histidine region in 4 H5 HA structures determined after freezing the crystals using cryo-solutions at different pH (corresponding pH shown in the top right corner of each structure). $2\text{Fo} - \text{Fc}$ difference maps are shown for each structure, with the contour level at 1.5σ (gray mesh). The structure on the left shows the position on H5 trimer. Important residues highlighted in pH 7.0 structure. See text for details. Information on the resolution and refinement parameters for each structure are shown in Table III.

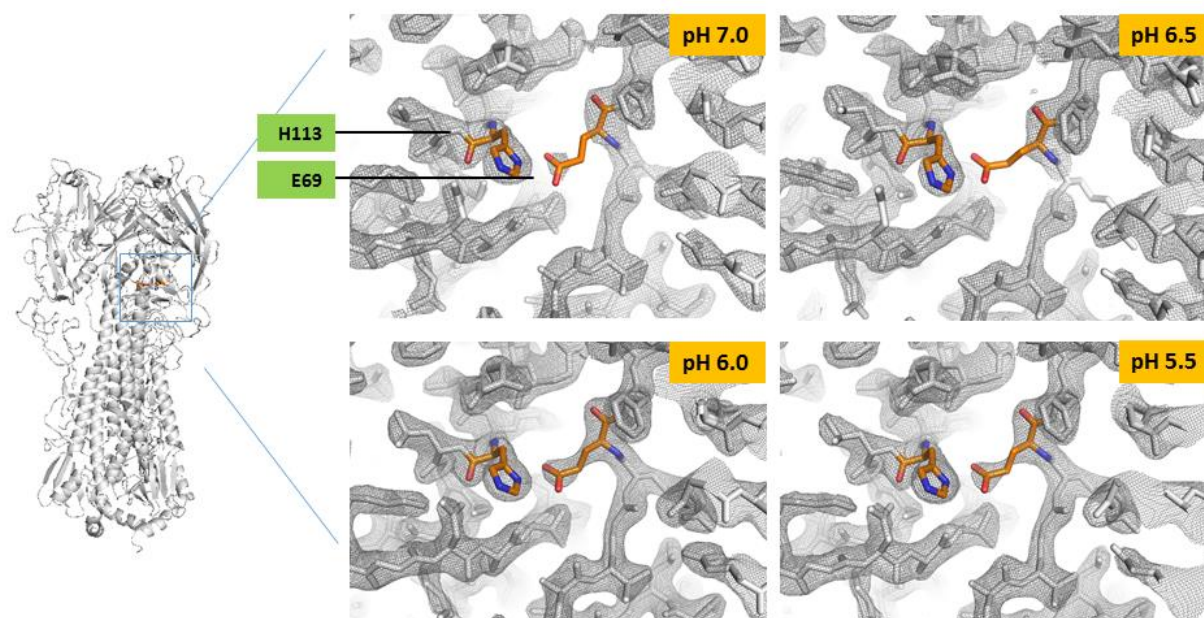


Figure 15. pH dependent change in anchoring of Glu69 to His113. Structures (with electron densities) of the HA1 – HA2 interface region in 4 H5 HA structures determined after freezing the crystals using cryo-solutions at different pH. $2F_o - F_c$ difference maps are shown for each structure (gray mesh), with the contour level at 2σ . The location of the region on H5 HA trimer is shown on the left. Positions of residues H113 and E69 are illustrated in pH 7.0 structure. Information on the resolution and refinement parameters for each structure are shown in Table III.

Similar behavior was observed in the local environments of HA1- H120, HA1 – H189 and HA2 – H142. These are novel residues that haven't been characterized in previous studies and their contribution to the regulation of the fusion process is unknown. In order to test the role of all discovered residues in the normal functioning of HA we will perform extensive mutagenesis studies and measure the mutational effects on pH induced conformational change and viral entry. Despite the fact that many tests still need to be done, it is very encouraging that the two largest changes observed by this methodology are in locations previously characterized by others as being very important for the regulation of fusion. Moreover, in the case of HA1-H38 the structural data reveals the potential mechanism by which the fusion process might be triggered.

Altogether, on the example of H5 HA we show a new X-ray crystallography - based approach to study the locations of pH sensor residues and the formation of salt bridges in pH sensitive proteins. This approach in combination with appropriate biological assays can give very useful information about changes in structure and dynamics of different viral and cellular proteins.

Chapter 3.3 - Characterization of Group 1 inhibitors: MBX2329 and MBX2546

(Adapted from: Basu et al., 2014; Antanasijevic et al., 2014a; see Appendix A)

As discussed above, MBX2329 and MBX2546 were discovered in an HTS project of over 100,000 small molecules performed by Microbiotix Inc. Extensive initial characterization of compound activity against different strains of influenza virus was performed in Lijun Rong's laboratory. It was discovered that MBX2329 and MBX2546 are very potent inhibitors of Group 1 influenza (H5 and H1 HA) with the IC50 values in the low micromolar range, while not having any activity against Group 2 influenza viruses. Additionally, the evidence from the RBC hemolysis assays suggested that they function by disrupting the HA-mediated fusion process (Basu et al., 2014).

First we tested the activity of the two compounds against H5N1 pseudovirus. Both compounds display the ability to inhibit the entry of H5N1 in a dose dependent way but show no activity against VSVG pseudovirus (Figure 16.). MBX2329 inhibits influenza entry with an IC₅₀ of 4.4 μ M, while the IC₅₀ for MBX2546 is 1.5 μ M.

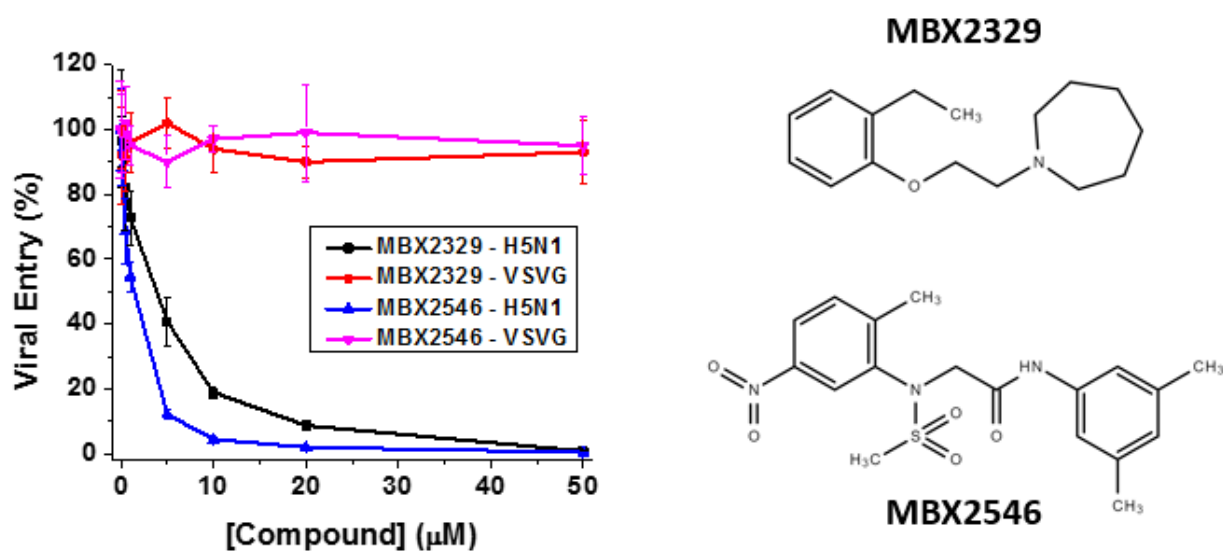


Figure 16. Activity of MBX2329 and MBX2546 against pseudovirus entry. MBX2329 and MBX2546 both show dose dependent inhibition of H5N1 pseudovirus entry while not inhibiting VSVG pseudovirus (left). The structures of the two compounds shown on the right.

Specific inhibition of influenza viruses with group 1 HA by MBX2329 and MBX2546 suggests that they interact with group 1 HA. To verify that HA is the target of the two compounds, we investigated the binding of MBX2329 and MBX2546 to recombinant H5 HA using WaterLOGSY NMR spectroscopy, which is designed to detect binding of small molecules to high-molecular-mass targets. Recombinant NA was used as the specificity control. In Figure 17.A, the top spectrum corresponds to the 1D NMR spectrum of the downfield region of MBX2329, with the aromatic resonances of the compound being denoted by red arrows. The second spectrum corresponds to the WaterLOGSY spectrum observed for MBX2329 in the absence of HA (i.e., a control experiment), and the third spectrum corresponds to the WaterLOGSY spectrum observed for MBX2329 in the presence of H5 HA. The relatively strong positively phased resonances of MBX2329 in the presence of H5 HA indicate that it is binding to HA. Conversely, the absence of signals in the fourth spectrum, which corresponds to the WaterLOGSY experiment in the presence of NA, suggests that MBX2329 is not binding to NA.

We characterized the binding properties of MBX2546 in a similar manner (Figure 17.B). The top spectrum corresponds to the 1D NMR spectrum of the downfield region of MBX2546, with the aromatic resonances of the compound being denoted by green arrows. The second spectrum corresponds to the WaterLOGSY spectrum observed for MBX2546 in the absence of HA (i.e., a control experiment), and the third spectrum corresponds to the WaterLOGSY spectrum observed for MBX2546 in the presence of H5 HA. In the presence of H5 HA, increased intensity of the positively phased resonances of MBX2546 clearly indicates that it is binding to HA. In contrast, in the presence of NA (Figure 17.B, bottom spectrum), the relatively weak signals, which resemble the no-protein control, suggest that MBX2546 is not binding to NA.

To further determine the binding region of MBX2329 and MBX2546, a WaterLOGSY-based competition assay was performed with a monoclonal antibody (C179). C179 was previously shown to

bind to a group 1 HA conformational epitope in the stem region formed by amino acid positions 318 to 322 in the HA1 subunit and by amino acid positions 47 to 58 in HA2 (Dreyfus et al., 2013). Overlapping binding sites would lead to a decrease in the signal of the compounds in the binding assay. As shown in Figure 17.C, addition of an equivalent amount of MAb C179, with respect to HA, significantly decreased the binding of MBX2329. The average reduction of MBX2329 resonance intensities was $52\% \pm 11\%$ ($n = 8$; $P = 0.001$), suggesting that the antibody is displacing the compound. Likewise, an equivalent amount of MAb C179 similarly decreased the binding of MBX2546 to H5 HA observed by WaterLOGSY (Figure 17.D), with an average reduction of the MBX2546 resonance intensities of $81\% \pm 5\%$ ($n = 8$; $P = 0.0001$). The results once again suggest that the antibody is also displacing MBX2546. These results are consistent with the notion that both inhibitors inhibit influenza A viruses with group 1 HA by binding to a group 1 HA-specific conformational epitope in the stem region of HA.

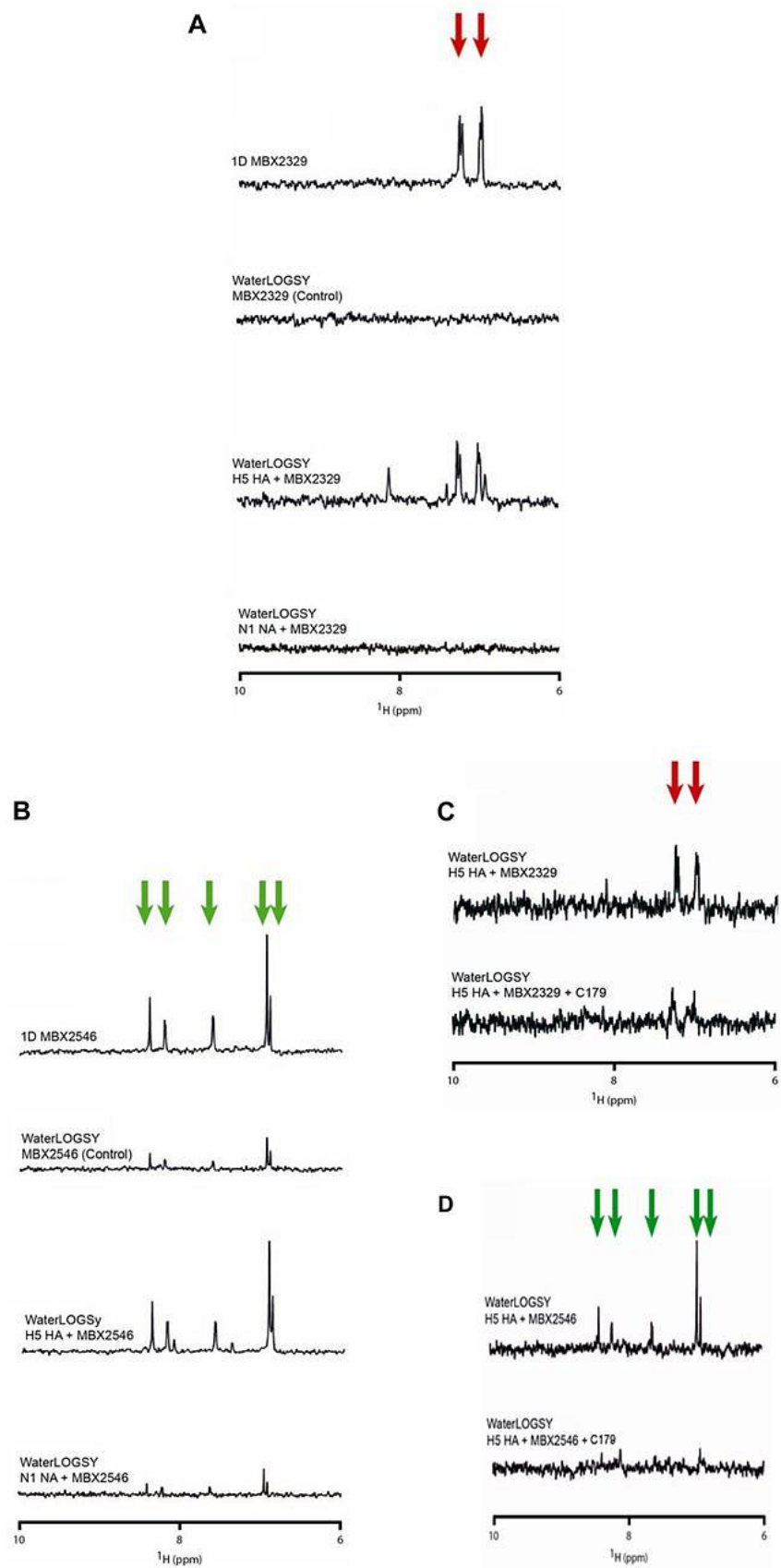


Figure 17. (see previous page) MBX2329 and MBX2546 bind to the conserved conformational epitope in the HA stem region. (A and B) Detection of binding of MBX2329 (A) and MBX2546 (B) to recombinant H5 HA by WaterLOGSY NMR. Red arrows represent the aromatic peaks of MBX2329, while green arrows represent the aromatic peaks of MBX2546. For this set of experiments, the conditions were 50 μM MBX2329 or MBX2546 with or without 0.2 μM HA in 20 mM PBS (pH 7.2) at 25°C, using a 900-MHz spectrometer with a mixing time of 2 s. (C and D) Competition WaterLOGSY of MBX2329 (C) and MBX2546 (D) binding to H5 HA in the absence (top spectrum) and in the presence (bottom spectrum) of MAb C179. For this set of experiments, the conditions were 20 μM MBX2329 or 10 μM MBX2546 with or without 0.2 μM HA and with or without 0.4 μM C179 in 50 mM PBS (pH 7.3) at 25°C, using a 900-MHz spectrometer with a mixing time of 2 s.

The binding to H5 HA was quantified using SPR. After standard amine coupling immobilization of recombinant H5 HA to the CM5 chip, compound solutions were run over the chip and steady-state binding results were determined (Figure 18.). Both, MBX2329 and MBX2546 display binding to immobilized H5 HA with the K_d values of $5.4 \pm 0.9 \mu\text{M}$ and $0.53 \pm 0.21 \mu\text{M}$, respectively. The binding constants match the corresponding IC50 values very well (4.4 μM for MBX2329 and 1.5 μM for MBX2546). For raw SPR data, see Appendix C.

We next investigated whether MBX2329 and MBX2546 bind to overlapping sites on HA using a WaterLOGSY-based competition assay. In this experiment, equal amounts of compound were added in the WaterLOGSY experiment, with the notion that overlapping binding sites would lead to a decrease in the signal of one or both compounds. Based on the absence of a change in signal intensity (Figure 19.A), the compounds appear to be able to simultaneously bind to HA, suggesting that they bind to different regions of HA. Furthermore, we used a NOESY experiment to examine the relative proximity of the compound binding sites. In this experiment, the absence of intermolecular NOEs in the presence of H5 HA (Figure 19.B) further suggests that MBX2329 and MBX2546 bind to sites that are $>6 \text{ \AA}$ apart. We further examined the binding epitopes of MBX2329 and MBX2546 for H5 HA by an STD NMR

experiment, which identifies ^1H in closest proximity to the protein surface. The relative STD for the interaction between MBX2329 and H5 HA is shown in Figure 19.C. In this representation, the red spheres and numbers represent the relative STD signal. The contact is relatively uniform, with the aromatic ring of MBX2329 in closest contact. Similarly, Figure 19.D shows the relative STD for the interaction between MBX2546 and H5 HA. Here, the green spheres and numbers represent the relative STD signal (the gray spheres represent STD signals that are too weak to be quantified). In this case, the contact is relatively non-uniform, with the most important contacts being in the center of the molecule and surprisingly little contact with the methyl groups.

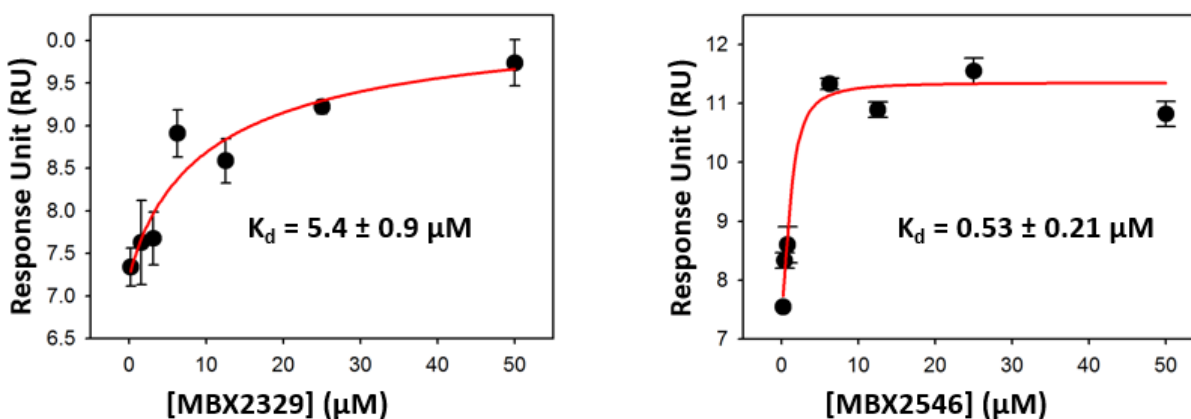


Figure 18. Surface plasmon resonance experiments with H5 HA and the two inhibitors. Steady-state results were used to determine the affinities of MBX2329 and MBX2546 for H5 HA (immobilized on a CM5 chip). Buffer conditions were: 50 mM phosphate, pH 8.3, 50 mM NaCl, 0.05 % Tween20, 2 % DMSO. Experiments repeated three times for each compound. K_d values are shown on each graph.

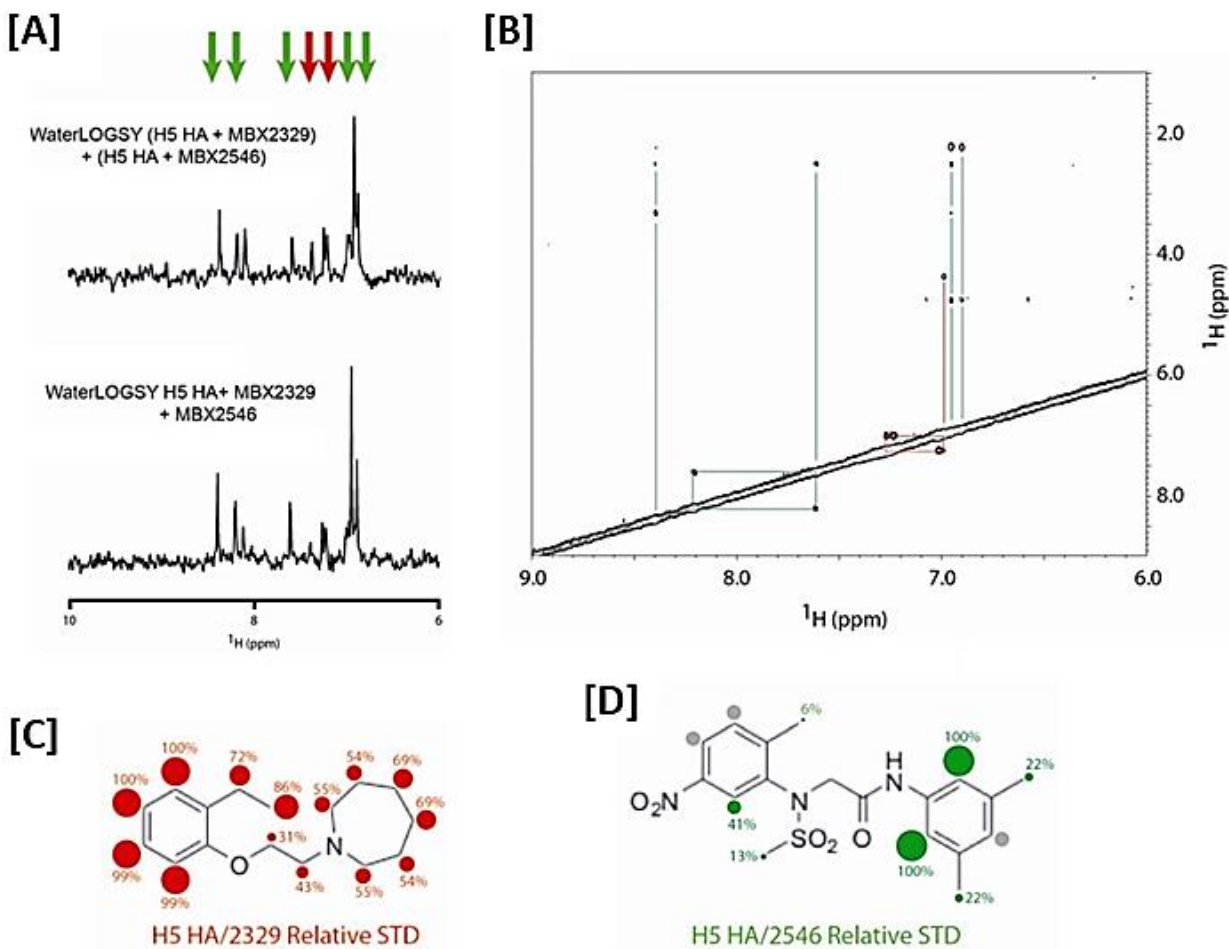


Figure 19. MBX2329 and MBX2546 bind to nonoverlapping sites on HA. (A) Competition assay performed between MBX2329 and MBX2546 for binding to influenza virus H5 HA by WaterLOGSY NMR. The top spectrum represents the sum of the WaterLOGSY of MBX2329 and H5 HA with the WaterLOGSY of MBX2546 and H5 HA. The bottom spectrum represents the WaterLOGSY signal in the presence of MBX2329, MBX2546, and H5 HA. The experimental conditions were 50 μM MBX2329 and/or 20 μM MBX2546 plus 0.2 μM HA in 20 mM PBS (pH 7.2) at 25 $^\circ\text{C}$, using a 900-MHz spectrometer with a mixing time of 1 sec. (B) Two-dimensional NOESY of MBX2329 and MBX2546 in the presence of H5 HA. The lines represent the intramolecular NOE connectivities. The experimental conditions were 50 μM MBX2329, 50 μM MBX2546, and 0.2 μM HA in 20 mM PBS (pH 7.2) at 25 $^\circ\text{C}$, using a 900 MHz spectrometer with a mixing time of 1 sec. (C and D) STD NMR studies to characterize the binding epitopes of MBX2329 (C) and MBX2546 (D) for H5 HA. The numbers and sizes of the spheres represent the intensity of the STD signal, which is related to the distance to the protein surface. For this set of experiments, the conditions were 50 μM MBX2329/MBX2546 with or without 0.2 μM HA in 20 mM PBS (pH 7.2) at 25 $^\circ\text{C}$, using a 900 MHz spectrometer with a saturation time of 1 sec.

Based on the C179 competition experiments both compounds appear to be having overlapping binding sites with the antibody. Mutagenesis was applied to further characterize the binding sites of MBX2329 and MBX2546. Point mutations in the stem-loop region of H5 HA that were described in previous chapters were applied in combination with pseudovirus entry assays. We determined the IC50 values for both compounds against 15 mutants (Table IV).

Based on our results the mutants can be divided into several groups. Mutations: HA1-I28V, HA2-D57E, HA2-I55V, HA2-T41A, HA2-Q42A and HA2-T49A do not seem to cause any significant effect on the inhibition by the two compounds. The effect on IC50 values is lower than two-fold which was chosen as the cutoff given the experimental limitations of the pseudovirus entry assays. Mutants HA2-L99A, HA2-V52A and HA2-N53A resulted in a strong decrease (> 10-fold) in activity of both, MBX2329 and MBX2546. In contrast, HA1-M31A, HA1-I28A and HA2-M102A showed a significant increase in activity (> 2-fold) for both compounds. On the other hand, 3 mutations affected the inhibitory properties of just MBX2329 or MBX2546. HA2-M102L caused a ~10-fold increase in IC50 of MBX2546 with very little effect on MBX2329, while HA2-S54R and HA2-I45A decreased the inhibitory capacity of MBX2329 with only subtle effect on MBX2546. These results are summarized in Figure 20. The binding site of C179 is highlighted in gray. The mutations affecting MBX2329 only are shown in black while the mutations unique for MBX2546 are shown in green. The mutations common for both compounds are highlighted in red. This data clearly confirms the C179-competition experiments and further strengthens the idea of the stem-loop region being the binding site of the two compounds.

Moreover, the differential effects of the mutants to compound inhibition is consistent with the notion that they bind unique sites which are in relatively close proximity (but >6 Å apart based on the NOE studies presented above).

TABLE IV

IC50 results for MBX2329 and MBX2546 against H5 HA mutants

Mutant	MBX2329		MBX2546	
	IC50 / μ M	Ratio to WT IC50	IC50 / μ M	Ratio to WT IC50
WT	4.4 \pm 0.6	1.00	1.5 \pm 0.2	1.00
D57E	6 \pm 1	1.36	2.5 \pm 0.4	1.67
I55V	6.8 \pm 0.9	1.55	1.5 \pm 0.1	1.00
I28V	6 \pm 1	1.36	1.0 \pm 0.3	0.67
Q42A	4.0 \pm 0.7	0.91	1.4 \pm 0.2	0.93
T49A	5.1 \pm 0.9	1.16	1.0 \pm 0.2	0.67
T41A	3.5 \pm 0.9	0.80	1.7 \pm 0.2	1.13
M31L	0.23 \pm 0.06	0.05	0.23 \pm 0.03	0.15
I28A	0.29 \pm 0.09	0.07	0.095 \pm 0.009	0.06
L99A	>50	>11	43 \pm 8	28.67
V52A	>50	>11	20 \pm 5	13.33
N53A	>50	>11	>50	>33
M102A	1.2 \pm 0.3	0.27	0.7 \pm 0.1	0.47
M102L	2.4 \pm 0.3	0.55	0.17 \pm 0.02	0.11
S54R	>50	>11	2.0 \pm 0.3	1.33
I45A	50 \pm 6	11.36	2.9 \pm 0.8	1.93

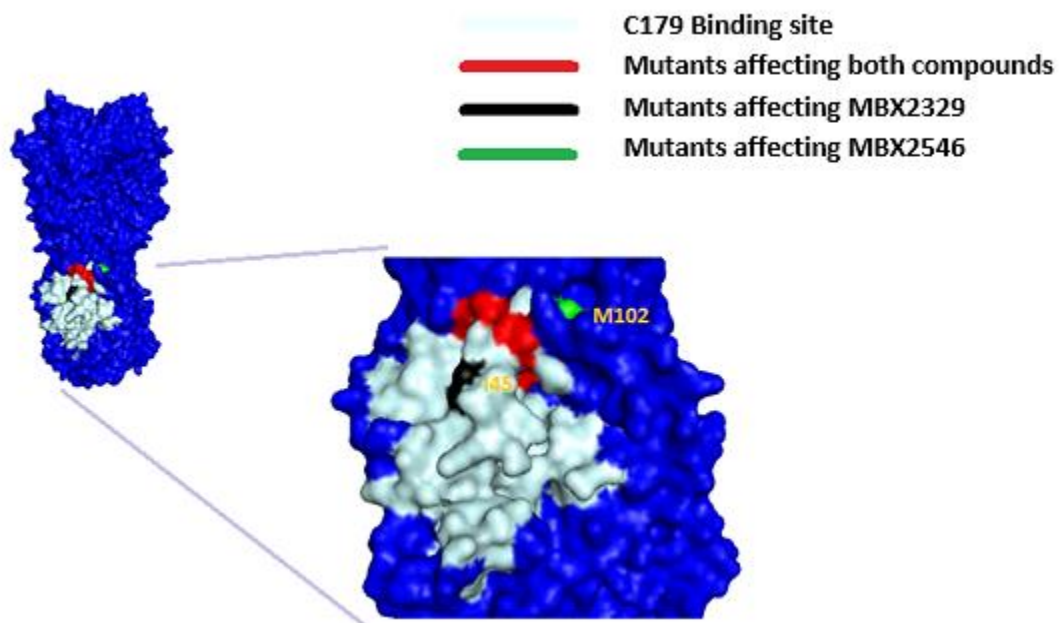


Figure 20. Mutations affecting the inhibitory properties of MBX2329 and MBX2546. C179 epitope is highlighted in gray. Mutations that affect the activity both compounds are shown in red. Mutants showing difference in inhibition by MBX2329 only are highlighted in red. Mutation that affects MBX2546 alone is shown in green.

Based on the C179 competition data, 10 ns molecular docking simulations were performed for MBX2329 and MBX2546 (work of Dr. Rama Mishra, Northwestern University). The details of the experiments are described in the Methods section. Importantly, the docking followed by the MDS was performed without any input from the mutagenesis data. The predicted binding modes for the two compounds are shown in Figure 21., and the amino-acid residues that are important for interaction with the inhibitors are labeled.

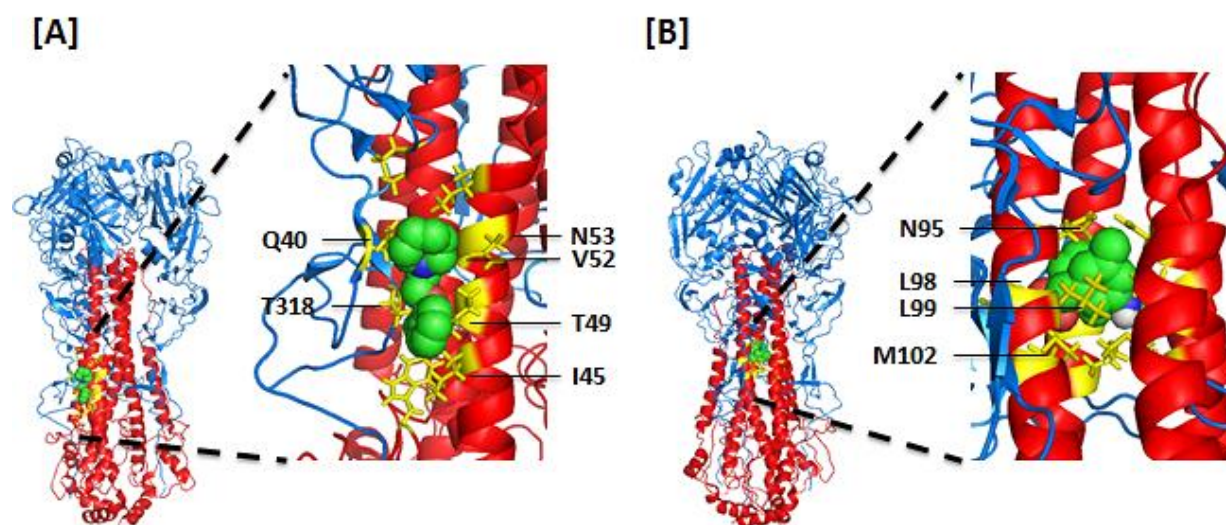


Figure 21. Molecular dynamics models of the MBX2329 and MBX2546 interactions with H5 HA. MBX2329 (A) and MBX2546 (B) are shown in the space-filling representation and the H5 HA side chains in closest proximity to the compounds are highlighted in yellow.

The MBX2329 ligand binding site (Figure 21.A) is found to be in a similar location to that of the TBHQ site within the stem loop (Russell et al., 2008). Notably, MBX2329 shows interactions with the side chains of HA1-Q40, HA1-T31, HA2-I45, HA2-V48, HA2-T49, HA2-V52, and HA2-N53. On the other hand, MBX2546 appears to be binding in the middle of the HA trimer interacting strongly with the residues HA2-N95, HA2-L98, HA2-L99, HA2-M102 (Figure 21.B). In this binding mode, two aromatic groups face one another with strong π - stacking effect. Significant side-chain rearrangement is taking place in the amino acids of the binding site in order to accommodate the compound.

Strikingly, there is an excellent agreement between the mutagenesis data and molecular docking results, given that both experiments were performed independently. Multiple residues found to be important for the activity of MBX2329 and MBX2546 by mutagenesis are in the proposed binding sites determined by molecular dynamics simulations.

Next, we attempted to co-crystallize H5 HA in complex with MBX2329 and MBX2546. We had some limited success with MBX2546 (Figure 22.). The crystallization conditions and refinement strategies are described in the Methods section while the refinement statistics are given in Table III. In the structure there is a very strong electron density at the identical location predicted to be the MBX2546 binding site by molecular docking and mutagenesis experiments (i.e. in the interior of the HA trimer). The density is roughly cone-shaped and does not offer enough structural detail to unambiguously confirm the presence of MBX2546 in the area. This is not very surprising given the unique binding mode of this compound, where it is expected to exist in at least 3 different orientations (a consequence of the threefold symmetry of H5 HA trimer). Importantly, this density is not present in the structure of protein alone. The compound is modeled in a conformation that provides the best fit to the electron density. Similarly to the molecular dynamics simulations result, MBX2546 interacts strongly with the HA2 residues: N95, L98, L99 and M102, that are all facing towards the inside of the H5 HA trimer.

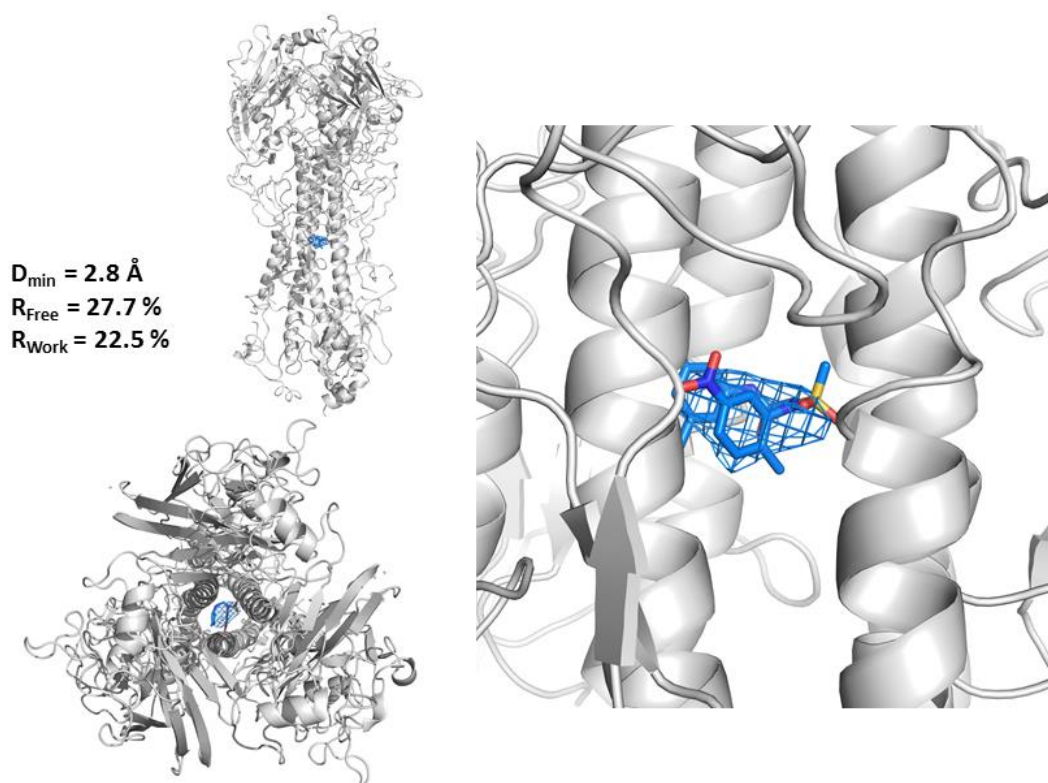


Figure 22. Crystal structure of H5 HA with MBX2546. Side- and top-view of the MBX2546 binding site in the H5 HA trimer are shown on the left (top and bottom, respectively). Enlarged side-view of the binding site with the compound modeled in is shown on the right. In all cases a cartoon representation of the protein was used. Unbiased $F_o - F_c$ difference map (blue mesh) is shown with the contour level at 3σ .

In order to verify the very unusual binding conformation of MBX2546 where the two aromatic groups seem to face one another, with a significant π -stacking effect, we applied NOESY NMR experiments to determine the compound structure in the H5 HA bound state (Figure 23.). The acquired NOESY spectrum was of very good quality with a high number of correlated ^1H , offering sufficient information for structure determination (Figure 23.A). The resulting lowest energy structure is shown in Figure 23.B (left). For comparison, MBX2546 structures obtained via molecular docking and x-ray crystallography are also shown (Figure 23.B, center and right, respectively). The NOESY structure appears more open compared to the other two structures, but still in cis-conformation with the two aromatic chains across one another. All the data combined strongly suggest the validity of the MBX2546 binding site and its binding conformation.

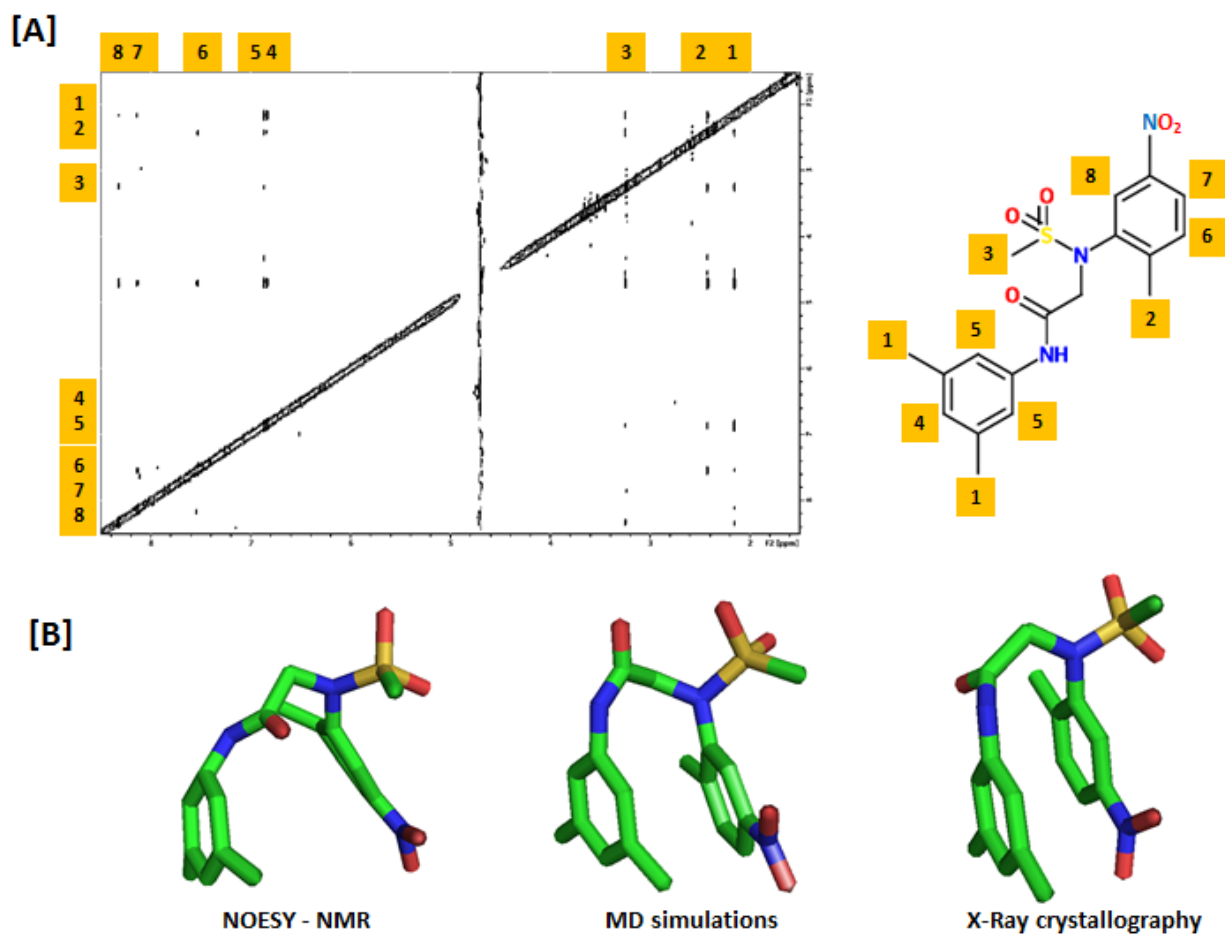


Figure 23. NOESY-based determination of the structure of MBX2546 in the bound state. (A) NOESY spectrum was acquired with 100 μM MBX2546 and 1 μM H5 HA in the sample. Mixing time was set to 300 ms. Peak assignment was performed on 1D NMR spectrum of the compound using Topspin 3.2 and is illustrated with orange labels. The structure determination was done in CNS software using experimental NOE data as restraints. (B) Comparison of the MBX2546 structures in bound state determined by NOESY (left), molecular docking (center) and x-ray crystallography (right).

Next tested the effect the inhibitors have on hemagglutinin-mediated fusion. To assay the effects of the compounds on the HA conformational change, limited proteolysis experiments at different pH shown in previous chapter were repeated in the presence of 100 μM MBX2329 or MBX2546. Both compounds displayed the ability to fully stabilize H5 HA even at lowest pH used in the tests (pH 4.5) as shown in Figure 24.A. Raw SDS PAGE results are shown on the left and the quantified data plots on the right. Additionally, the experiments were repeated with constant pH of incubation (pH 4.5), but in the presence of increasing inhibitor concentrations. The goal was to determine the dose dependency for the fusion inhibition process and the respective IC₅₀ values. pH 4.5 incubation was chosen because it provides the largest dynamic range between neutral and low pH conformation. As shown in Figure 24.B and C, both MBX2329 and MBX2546 are providing dose dependent protection to H5 HA from pH induced conformational rearrangements and subsequent proteolysis by trypsin. Interestingly, the IC₅₀ values determined in the limited proteolysis assay (1.3 μM and 1.6 μM for MBX2329 and MBX2546, respectively) match the biologically more relevant IC₅₀ values determined by pseudovirus entry assay.

In addition to these datasets, in the Rong laboratory it was shown that the two compounds do not inhibit the receptor binding step of the entry process (using hemagglutination assays) and that they inhibit hemolysis of the red blood cells when infected with H5 virus in a pH dependent hemolysis assay (Basu et al., 2014). Altogether, the data suggests that MBX2329 and MBX2546 inhibit the low-pH induced fusogenic conformational change in HA and act as fusion inhibitors.

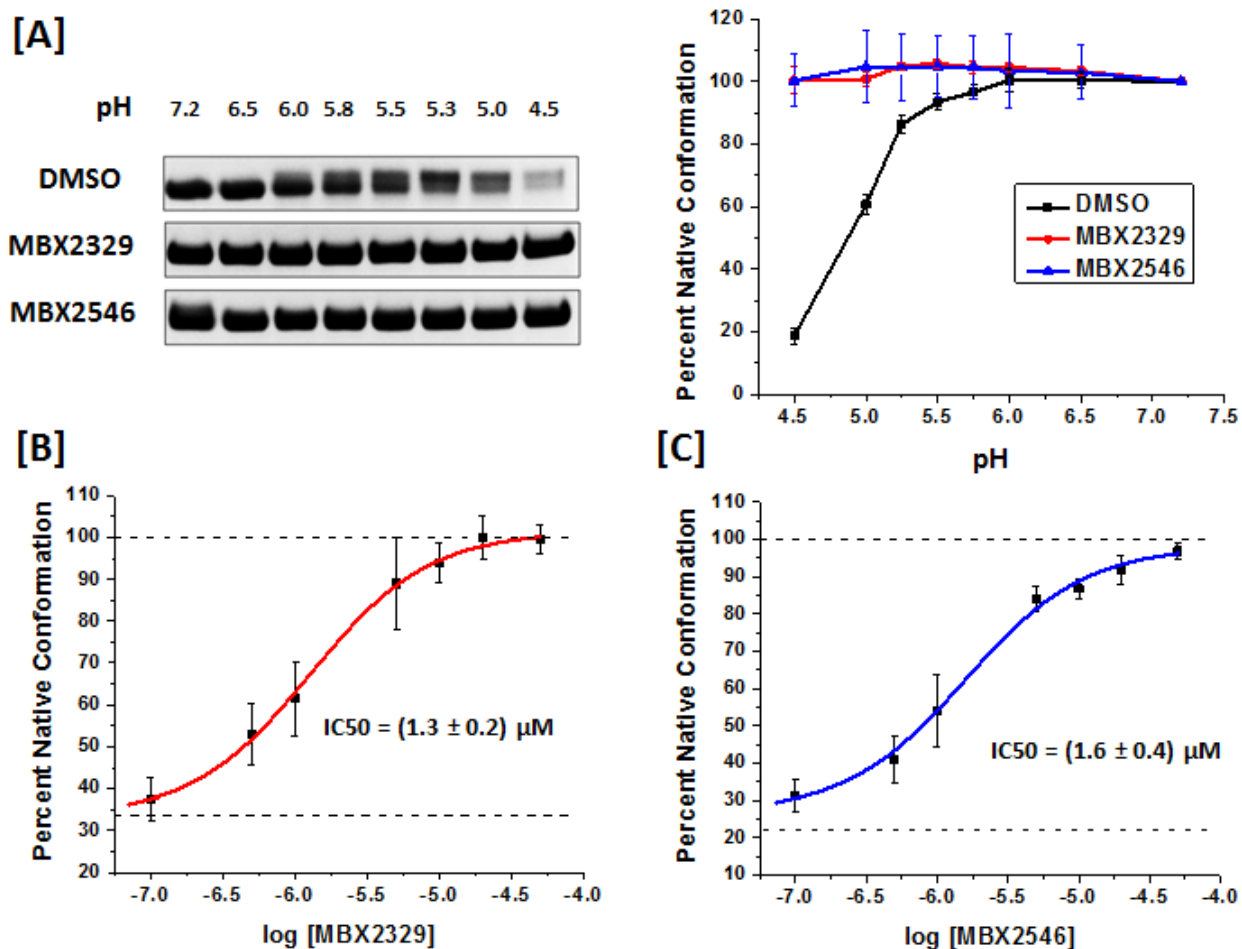


Figure 24. pH-based limited proteolysis assays confirm that MBX2329 and MBX2546 act as fusion inhibitors. [A] H5 HA was pre-incubated with 100 μ M MBX2329 or MBX2546 (or DMSO as a control) and then subjected to incubation in a phosphate-citrate buffer at different pH for 30 min (37 $^{\circ}$ C). The solutions were neutralized and digested with trypsin for 30 min and subjected to SDS PAGE. The amount of H5 HA in the native conformation was determined based on the amount of HA1 that remained uncleaved. Raw SDS PAGE data is shown on the left and the plots after quantification and normalization (band intensity at pH 7.2 = 100 %) are shown on the right (DMSO control – black, MBX2329 – red, MBX2546 – blue). The data suggests that in the presence of 100 μ M MBX2329 or MBX2546, H5 HA is fully protected from proteolysis. [B] To assess the dose dependency of the compound induced stabilization the same experiments were repeated using different amounts of MBX2329 and MBX2546 in the initial step, and subsequent incubation at pH 4.5 for 30 min (37 $^{\circ}$ C). Control samples (DMSO) were run with incubations at pH 7.2 and 4.5 for the determination of dynamic range (top and bottom asymptote, respectively) and normalization (band intensity at pH 7.2 = 100 %). All experiments repeated at least 3 times. The data was quantified, normalized, averaged and eventually fitted using OriginPro.

Next, we used the thermal shift assays (TSA, differential scanning fluorimetry) to test whether MBX2329 and MBX2546 induce any changes in the stability of H5 HA. Thermal stability of hemagglutinin is correlated very well to its pH-dependent structural conformations and the melting points of HA under different conditions are a good measure of its dynamic states (Remeta et al., 2002).

The experiments were performed in several different ways. In order to measure the effect MBX2329 and MBX2546 have on the stability of H5 HA at different pH, in the first set of assays we would pre-incubate H5 HA with the compounds (30 min at room temperature) and then adjust the pH to the desired value (pH range 8.0 – 4.0). Alternatively, experiments were performed in the opposite order where, either 50 μ M MBX2329 or MBX2546 was added after the incubation of H5 HA in phosphate-citrate buffer of a certain pH (30 min at 37 °C). The results for MBX2329 and MBX2546 are shown in Figure 25.

Thermal shift assays reveal that there is a very significant stabilization effect of the two compounds on H5 HA. At neutral pH, 50 μ M amounts of MBX2329 and MBX2546 result in an increase of the melting point of hemagglutinin by ~ 9 °C and ~ 10 °C, respectively. The comparison of the datasets from pre- and post-incubation experiments (red and blue curves) reveals two very important points. (1) Both compounds can stabilize H5 HA even at very low pH values, if added prior to the low pH incubation. In the presence of MBX2329 and MBX2546 the protein is more stable at pH 4.75 than it is without the compounds at neutral pH. (2) Both compounds provide stabilization to H5 HA only if added at pH 6.00 or higher. From the post-incubation datasets (blue curves in Figure 25.) it can be concluded that the compound capacity to stabilize H5 HA is diminished at pH 5.5 and lower, most likely due to the pH induced rearrangement of the compound binding site. Upon neutralization the binding site is reestablished and the compounds can interact with hemagglutinin again (data not shown).

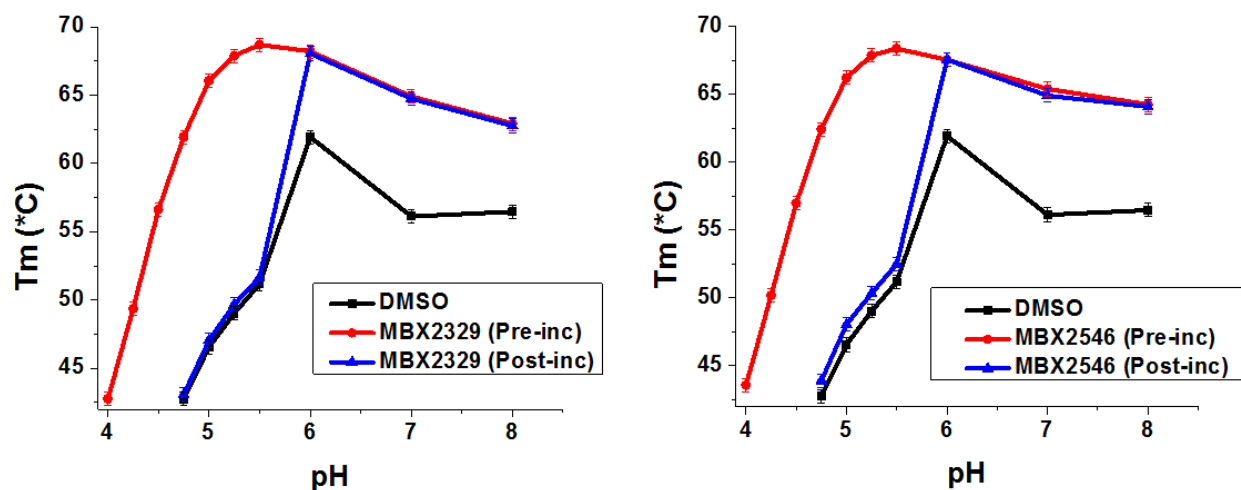


Figure 25. Thermal shift assay results for H5 HA with MBX2329 (left) and MBX2546 (right). Melting point of H5 HA (with DMSO) at different pH is shown in black on both graphs. The results of the experiments with MBX2329 and MBX2546 where the compounds were pre-incubated with the protein prior to pH adjustment are shown in red. For experiments with post-incubation (compounds added after the pH adjustment) the data is shown in blue. The data points at pH 4.50, 4.25 and 4.00 could not be acquired in certain cases (blue and black curves) due to significant background signal which is a consequence of the irreversible conformational change in H5 HA resulting in the exposure of hydrophobic domains that SYPROOrange dye can bind to.

Chapter 3.4 - Group 1 inhibitors: Determining the binding site and mode of action of RLC

Anti-influenza properties of compound RLC were first identified in the Rong lab. The precursor of this compound was discovered in an HT screen of over 20,000 compounds. During the chemical optimization of the initial hit, RLC showed the most promising properties compared to all other daughter inhibitors. This compound is very well behaved in terms of stability and solubility and it shows nanomolar activity against the entry of H5 HA and H1 HA based viruses (IC₅₀ values are 200 and 50 nM, respectively). Early data from the Rong lab suggested that RLC might act as a fusion inhibitor of Group 1 viruses. We have applied X-ray crystallography and NMR to give us some further insight into the mechanisms of binding and activity of this compound to H5 HA.

The crystal structure of RLC in complex with H5 HA was obtained by crystal soaking. The details are described in the Methods section and the structure statistics are given in Table III. The structure of the complex with H5 is shown in Figure 26. RLC appears to be binding on the interface of HA1 and HA2 subunits in HA monomer. Consequently, there are 3 binding sites for the compound and they are all populated in the structure obtained. RLC is sitting in a binding pocket that's highly conserved among all group 1 HA and consists of residues HA1: H18, W21, H38, Q40 and HA2: I45, V48, T49, V52. The carbonyl group of RLC is forming a hydrogen bond with HA1 – T325. Interestingly, the binding of RLC induces very little structural changes in the side chains of the amino acids it interacts with (RMSD value of 0.259 Å for all atoms of 32 residues that constitute the binding site).

This site and the histidine residues in it have already been identified in the previous Chapters as the potential regulators of the early stages of H5 HA fusion. It has been shown that residue H38 (Figure 14.) undergoes the conformational change upon protonation at lower pH. The presence of RLC restricts the movement of H38 and prevents any structural rearrangements in the region (Figure 27.). We

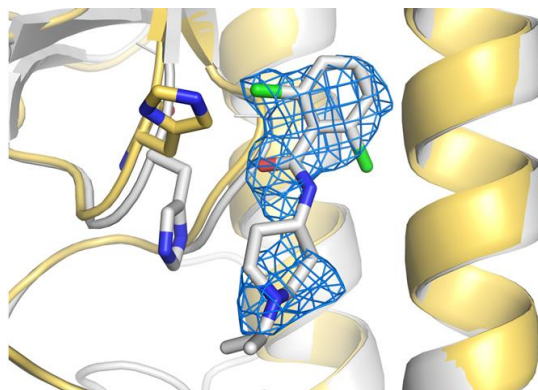


Figure 27. Overlay of the low pH structure of HA and the structure of H5 HA complex with RLC. Structure of H5 HA at pH 5.5 is shown in gold. Structure of H5 HA complex with RLC is shown in gray, with the compound density displayed in blue. Change in conformation of H38 occurring at pH < 6.0, results in a significant perturbation of the compound binding site. Unbiased $F_o - F_c$ difference map (blue mesh) is displayed, with the contour level at 2.5σ . Structure was determined to the resolution of 2.2 Å.

The sequence alignment of the RLC binding site reveals some major differences that explain the group and strain specificity of this compound (Figure 28.A). RLC inhibits only group 1 HA based viruses (i.e. H1 and H5), but not group 2 viruses (i.e. H3 and H7). The reason for this lies in the amino acid sequence of the RLC binding site. H38, which is highly conserved in group 1 HA, is one of the key residues for the interaction with RLC. However, in H3 and H7 HA, it is substituted by asparagine that is glycosylated. The presence of sugar chains in that location is expected to diminish any interaction with the compound and any inhibitory activity (Figure 28.B).

On the other hand, RLC shows a slight preference towards H1 HA in comparison to H5 HA (IC50 values are 50 nM and 200 nM, respectively). The structure analysis reveals that H1 HA has a more hydrophobic binding pocket that can achieve better interaction with the compound's aromatic head (Figure 28. C). The primary changes when comparing H5 to H1 HA are HA1: Q40 to V and HA2: V48 to I.

These residues are in direct contact with the inhibitor. Also, the importance of the aromatic part of the RLC for binding to HA has been verified by STD NMR experiments (see the text below). Hence, the increase in hydrophobic interaction with the aromatic head of the molecule may explain the increase in potency observed experimentally.

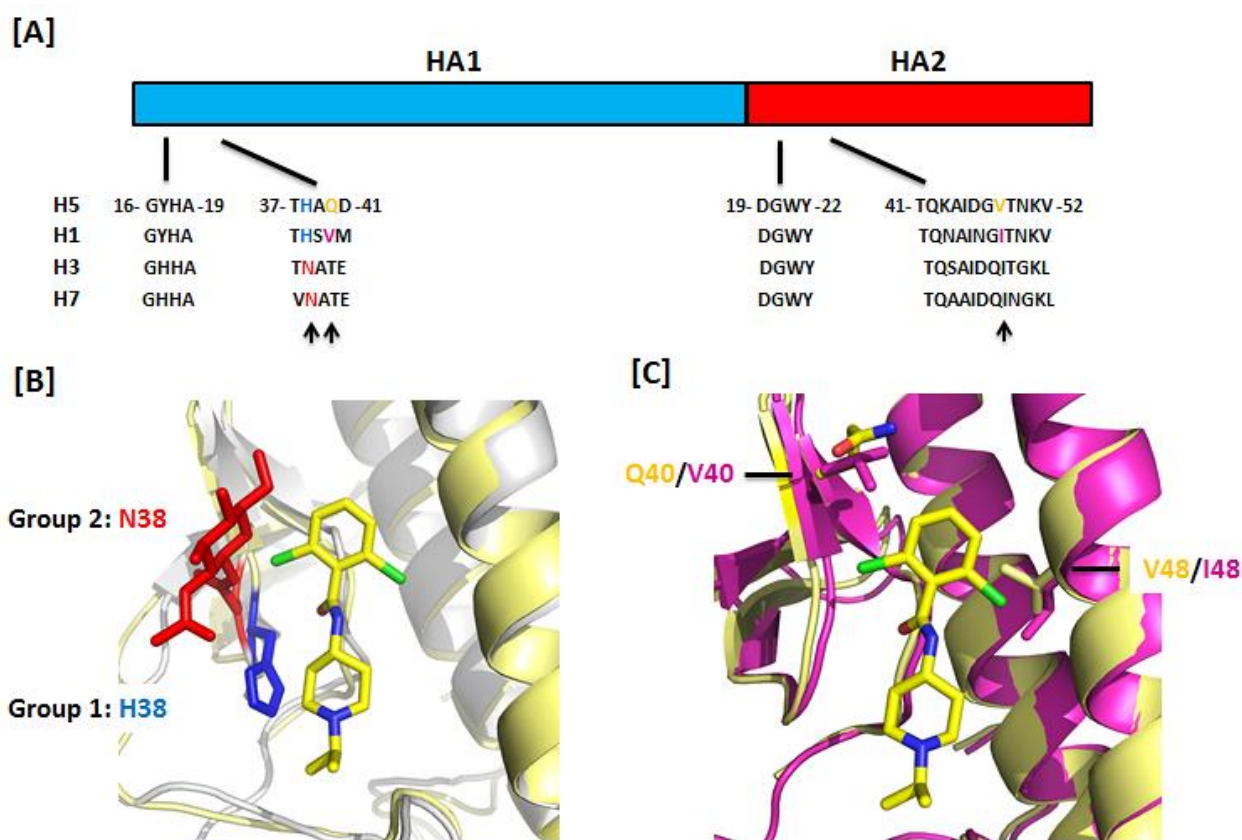


Figure 28. Sequence and structure alignment in the vicinity of RLC binding site. (A) Sequence comparison between group 1 (H1 and H5) and group 2 (H3 and H7) hemagglutinin; (B) Structure alignment between H5 HA (yellow) and H7 HA (gray) in the vicinity of RLC binding site (PDB entry: 4R8W). Residue 38 is shown in blue for H5 and red for H7 (together with N-acetyl-glucosamine). (C) Structure alignment between H5 HA (yellow) and H1 HA (magenta, PDB entry: 1RU7).

The overlay of pH 5.5 structure of H5 HA described in previous chapters and the structure of the H5 HA complex with RLC (Figure 27.) suggests that the low pH conformation of H38 would perturb the binding site significantly and at least partially prevent the compound from interacting. To test this hypothesis, WaterLOGSY NMR experiments were applied. The binding of RLC to H5 HA was measured in several different ways. First we acquired WaterLOGSY spectrum for the sample consisting of 100 μ M RLC + 5 μ M H5 HA, in phosphate buffer at pH 7.4. Then the measurement was done in acetate buffer at pH 5.5, where the compound was added after a 15 min incubation of H5 HA at low pH. Finally, we also determined the WL spectra in the same acetate buffer but this time with the pre-incubation of H5 HA and RLC at neutral pH (15 min), prior to the introduction of low pH buffer. The aromatic portions of the WL spectra are shown in Figure 29.A.

WaterLOGSY data indicates that there is a very strong interaction between RLC and H5 HA at pH 7.4 which is agreement with the proposed mode of action for this compound. After incubation of H5 HA at low pH and subsequent introduction of the compound there is a strong decrease in the amount of WaterLOGSY signal, suggesting less binding of RLC to the protein. However, the interaction is preserved if the compound is pre-incubated with H5 HA at pH 7.4, before the pH was lowered to 5.5. RLC seems to stabilize HA, but only if added before the low-pH treatment. At pH 5.5, the compound does not bind very well to the protein indicating the partial rearrangement of its binding site. Altogether, WL data strongly supports the mechanisms of binding and activity for RLC that were proposed based on the crystal structure of the compound in complex with H5 HA.

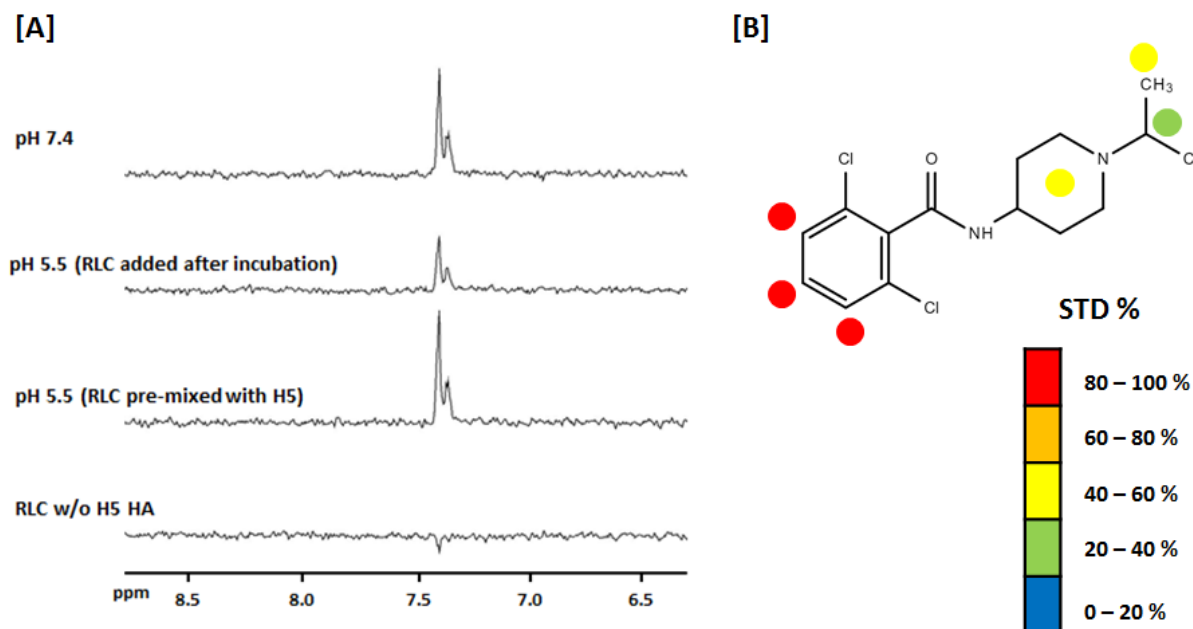


Figure 29. NMR studies on RLC interactions with H5 HA. (A) Aromatic portions of the WaterLOGSY spectra of RLC under different conditions. The first WL spectrum from the top is for 100 μM RLC + 5 μM H5 HA in 20 mM phosphate buffer (pH 7.4) + 150 mM NaCl (10% D_2O). Second WL spectrum is obtained for the same sample but in a 20 mM d-acetate buffer (pH 5.5) + 150 mM NaCl (10% D_2O). In this case the compound was added after a 15 min incubation of H5 HA in the acetate buffer. The third spectrum is acquired at pH 5.5 but with the pre-incubation of RLC and H5 HA, prior to the addition of d-acetate buffer. The bottom spectrum is a control with 100 μM RLC and without any protein. Experimental parameters were: $t_{\text{sat}} = 2$ sec, $d1 = 2.5$ sec and $\text{NS} = 1024$, which corresponds to a ~ 2 hour experiment. (B) Results of the STD analysis of the RLC interactions with H5 HA. Circle color indicates the STD % from a defined range. STD was acquired for 100 μM RLC \pm 10 μM H5 HA in 50 mM phosphate buffer (pH 8.2) + 50 mM NaCl (in 100% D_2O). Saturation time was 1 sec, and the on-resonance frequency was set to -1 ppm. Total experimental time was ~ 12 hours. Data quantification and analysis was done as described in the Methods section.

Additionally we applied STD to determine which parts of the RLC are more involved in the interaction with the binding pocket on the HA surface (Figure 29.B). Piperidine ^1H are very difficult to assign so we used the average STD signal for the entire group based on all observable resonances. The final data clearly indicates that the aromatic portion of the molecule is closer to the hydrophobic residues on the protein surface. On the other hand, the piperidine and isopropyl groups in the molecule are generating significantly less hydrophobic interaction. This data is in excellent agreement to the crystal structure, where we can see several Val and Ile residues in immediate proximity to the aromatic ^1H (Figure 26.). The STD findings also support the suggested reasons behind the increase in affinity towards H1 HA in comparison to H5 HA.

Altogether, our data clearly supports the fusion inhibition as the mechanism of action. Additionally, X-ray structure reveals the molecular details of this mechanism and together with STD data provides valuable resource for chemical optimization of RLC.

Chapter 3.5 - Characterization of Group 2 inhibitors: TBHQ

(Adapted from Antanasijevic et al., 2013; see Appendix A)

As noted in the introduction, the small molecule TBHQ has been initially reported to inhibit H3 HA-mediated influenza entry (Bodian et al., 1993; Russell et al., 2008), a Group 2 HA that is phylogenetically related to H7 HA. Accordingly, we first tested the inhibitory properties of TBHQ using pseudovirions containing H3 HA. As shown by Figure 30., TBHQ inhibits H3 HA-mediated entry with an $\text{IC}_{50} \sim 7 \mu\text{M}$ (purple triangles), which is in agreement with the previously reported IC_{50} for inhibition of H3 influenza infection. Next, we tested the inhibitory properties of TBHQ using pseudovirions containing H7 HA. As shown by Figure 30., TBHQ inhibits H7 HA-mediated entry with an $\text{IC}_{50} \sim 6 \mu\text{M}$ (black squares). In a next step, specificity to HA is shown by the lack of detectable inhibition for VSVG-mediated entry, pseudovirion containing an unrelated envelope protein (Figure 30., red circles). Finally,

the toxicity of TBHQ was determined to be $CC_{50} > 100 \mu\text{M}$ as shown in Figure 30. (blue triangles). Taken together, these experiments show that the small molecule TBHQ inhibits H7 HA-mediated entry with a similar potency to that of influenza H3 infection.

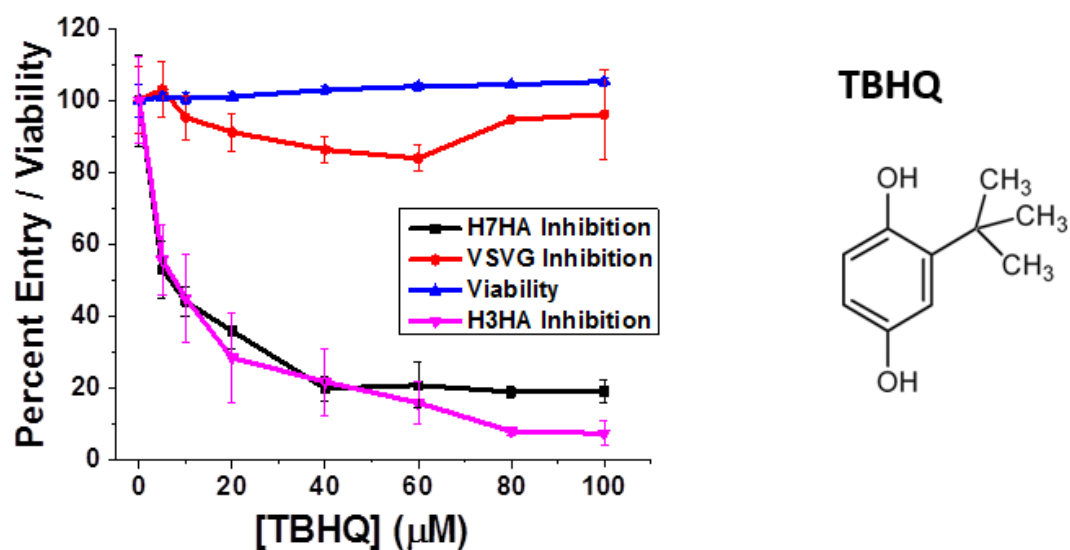


Figure 30. TBHQ inhibits H3 and H7 HA-mediated entry. Each concentration point was performed in triplicate. TBHQ structure is shown on the right.

WaterLOGSY NMR has previously been shown to be useful for the detection of small molecule interactions with large protein complexes (Dalvit et al., 2001), including the 200 kDa trimer of influenza HA (Ramirez et al., 2013). Accordingly, we first tested whether TBHQ binds to recombinant H3 HA using the WaterLOGSY experiment. As shown in Figure 31., the presence of positively phased TBHQ resonances in the NMR experiment clearly indicates that TBHQ binds to H3 HA. Previously, TBHQ was shown to bind to the stem loop of H3 HA by x-ray crystallography (Russell et al., 2008). Moreover, the monoclonal antibody F49 has been reported to bind to the stem loop of H3 HA (Ueda et al., 1998). Consequently, we tested TBHQ binding to the H3 HA stem loop using a WaterLOGSY-based competition assay in the presence of antibody F49. As shown in Figure 31.A, the addition of monoclonal antibody F49 significantly decreases the observed binding of TBHQ (the average reduction of TBHQ resonance intensities was 79 ± 22 %), suggesting that the antibody is displacing the compound. Next, we characterized the binding of TBHQ to H7 HA. As shown in Figure 31.B, TBHQ binds to H7 HA and, based on the competition NMR experiment in the presence of antibody F49, TBHQ binds to the stem loop region of HA (the average reduction of TBHQ resonance intensities was 69 ± 23 %). We further characterized the TBHQ interaction with H3 and H7 HA using the STD NMR experiment, which gives insight into the small molecule ^1H in closest contact with the protein surface (Meyer et al., 2003; McCullough et al., 2012). A summary of the relative intensities of the TBHQ STD spectrum is shown in Figures 31.C and 32.D, for the HA of H3 and H7, respectively. Based on this analysis, the TBHQ contacts to the H3 and H7 HA surfaces are similar with the aromatic ^1H in closest contact. Interestingly, in both cases the tert-butyl methyl ^1H exhibit significantly less STD intensity, suggesting that they are more distant from the protein surface and thus they may present attractive sites for modifications designed to increase affinity. Taken together, the NMR experiments indicate that TBHQ binds to the stem loop of H3 and H7 HA with a similar mode of binding.

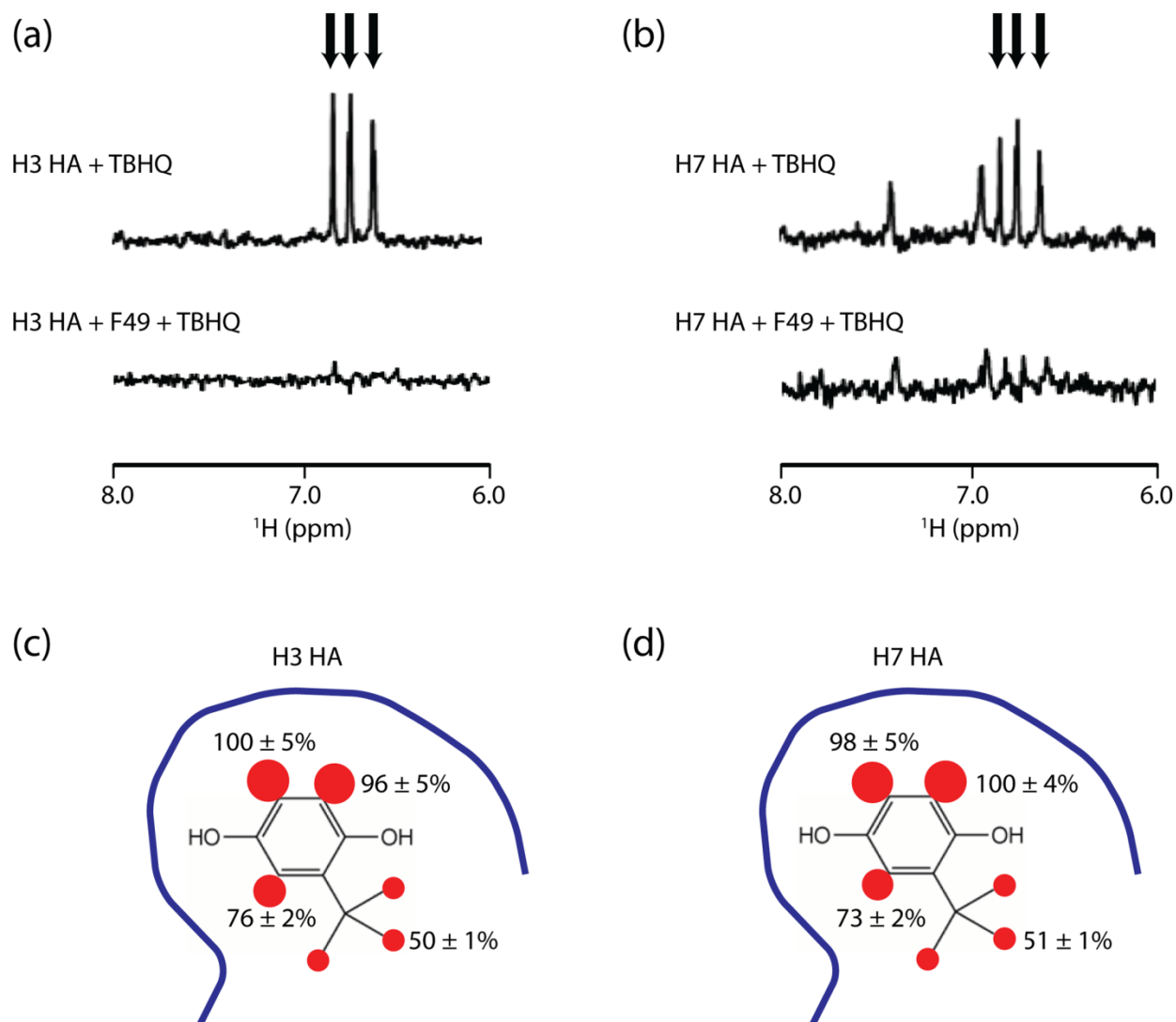


Figure 31. TBHQ binds to the H3 and H7 HA stem loops. (A) WaterLOGSY NMR of TBHQ binding to H3 HA in the presence and absence of monoclonal antibody F49. (B) WaterLOGSY NMR of TBHQ binding to H7 HA in the presence and absence of monoclonal antibody F49. In (A) and (B) the aromatic resonances of TBHQ are denoted by arrows. (C) Relative STD signals of TBHQ in the presence of H3 HA. (D) Relative STD signals of TBHQ in the presence of H7 HA. The blue line represents the protein surface. The size of the red spheres represent the magnitude of the observed STD for each ^1H .

As discussed above, during influenza entry, the low pH of the endosome triggers a large, irreversible conformational change in HA, which is necessary for membrane fusion. Previously, TBHQ has been shown to inhibit H3 HA-mediated entry by stabilization of the HA neutral pH conformation (Bodian et al., 1993). Accordingly, we used a limited proteolysis assay and bis-ANS fluorescence to test the stability of H7 HA at different pH in the presence and absence of TBHQ. As shown in Figure 32.A, H7 HA becomes more susceptible to proteolysis at a midpoint corresponding to $\text{pH} \sim 4.9$ (filled circles, solid line), which is similar to that previously described for a cell-cell fusion assay of H7 HA (Ilyushina et al., 2007). A similar observation can be made when using bis-ANS fluorescence to detect the onset of conformational change (Figure 32.B, black lines). Interestingly, the addition of TBHQ appears to stabilize H7 HA to conformational change by shifting the midpoint to $\text{pH} \sim 4.5$ (open squares, dotted line in Figure 32.A, and red line in Figure 32.B). We note that a similar sized shift to lower pH has been observed for an unrelated fusion inhibitor of H1 HA influenza using a cell-based assay (Zhu et al., 2011). In summary, the fusion assays performed using proteolysis and bis-ANS fluorescence as the means for detection, suggest that TBHQ inhibits H7 HA-mediated entry by stabilizing the neutral pH conformation and thereby disallows the conformational change necessary for membrane fusion.

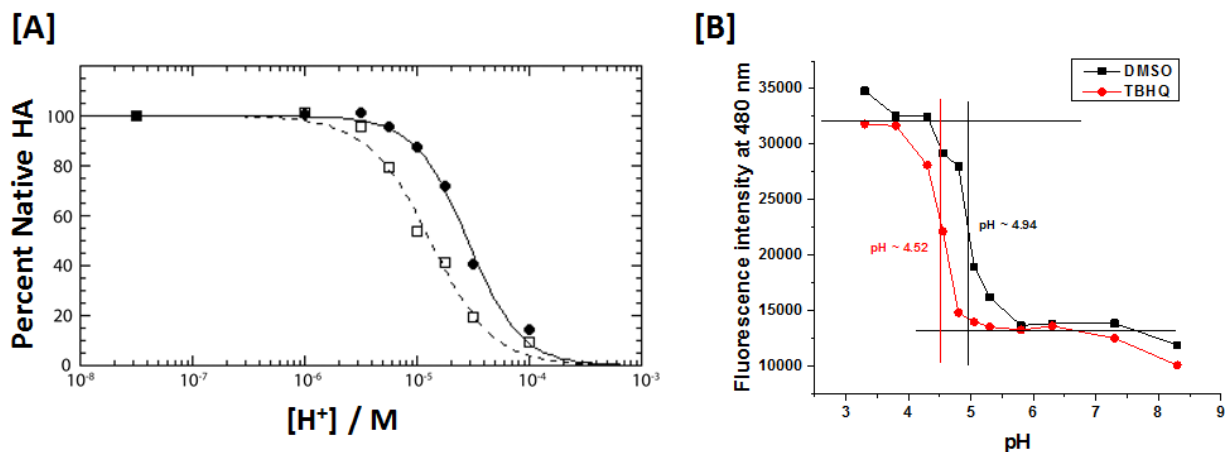


Figure 32. TBHQ stabilizes the neutral pH conformation of H7 HA. (A) Limited proteolysis experiment for H7 HA in the presence (open squares, dotted line) and absence (filled circles, solid line) of TBHQ at different pH. The curves correspond to fits using $pH_{mp} = 4.89$ and $n = 1.6$ in the absence of TBHQ and $pH_{mp} = 4.45$ and $n = 1.8$ in the presence of TBHQ. (B) Fusion assays performed using bis-ANS fluorescence for detection of conformational change. In the absence of any compounds the protein undergoes the conformational change freely, with the midpoint at $\sim pH 4.9$ (black). In the presence of TBHQ the midpoint of the transition curve shifts to $\sim pH 4.5$ (red).

Chapter 3.6 - Chemical optimization of TBHQ

After characterizing the TBHQ mechanisms of binding and action, we went on to attempt to improve the activity and stability of this compound. In the chemical optimization trials we have used all of the results described in the previous section as well as the data available in the literature (Bodian et al., 1993; Russell et al., 2008). Interestingly, TBHQ is an FDA-approved antioxidant (van Esch, 1986) and thus its low toxicity makes it an attractive lead compound. However, the antioxidant properties of TBHQ diminish enthusiasm due to potential oxidation-reduction reactions (e.g. reduction of disulfide bonds) or

covalent attachment to host proteins. Indeed, hydroquinone derivatives are generally considered to be pan assay interference compounds (PAINS), which promiscuously bind to targets and consequently should be removed from the "hit" list of industrial screens (Baell and Holloway, 2010; Dahlin and Walters, 2015). In the first part of the optimization process we first show that the antiviral properties of TBHQ are not related to oxidation-reduction reactions. We then describe modulation of the TBHQ potential reactivity and the enhancement of the derivative's antiviral activity through a structure-activity study. Finally, we use NMR and Molecular Dynamics to characterize the interaction between the most promising compounds and H7 HA. The entire list of compounds with their information (chemical structure, chemical name, origin, IC50 values against H7 HA, H5 HA and VSVG based virus) is shown in Table V.

TABLE V

TBHQ and its derivatives

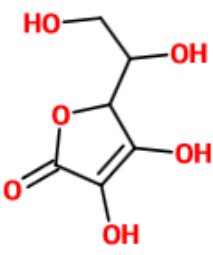
Compound Structure	Name and Source	Compound Number	Activity against H7 - IC50 -	Activity against H5 - IC50 -	Activity against VSVG - IC50 -
	Ascorbic Acid Sigma: A7506-25G	1	> 100 μ M	> 100 μ M	> 100 μ M

TABLE V (continued)

TBHQ and its derivatives

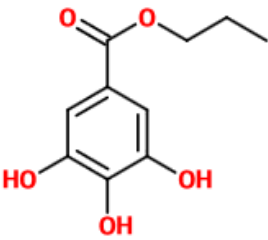
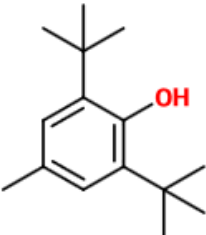
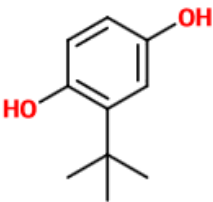
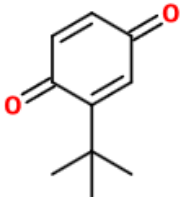
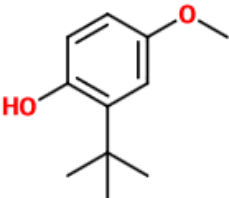
Compound Structure	Name and Source	Compound Number	Activity against H7 - IC50 -	Activity against H5 - IC50 -	Activity against VSVG - IC50 -
	Propyl gallate Sigma: P3130-100G	2	> 100 μM	> 100 μM	> 100 μM
	2,6-Di-tert-butyl-4-methylphenol Sigma: B1378-100G	3	~ 60 μM	> 100 μM	> 100 μM
	2-tert-Butyl-1,4-hydroquinone Sigma: 112941-100G	4	6 μM	> 50 μM	> 50 μM
	2-tert-Butyl-1,4-benzoquinone Sigma: 429074-5G	5	> 50 μM	> 50 μM	> 50 μM
	4-methoxy-2-tert-butylphenol Fluka: PHR1306-500MG	6	~ 50 μM	> 50 μM	> 50 μM

TABLE V (continued)

TBHQ and its derivatives

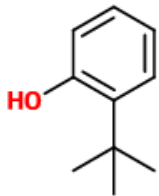
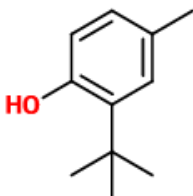
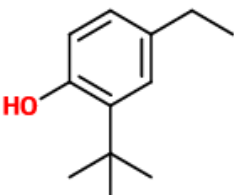
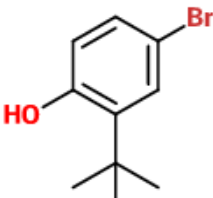
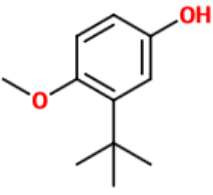
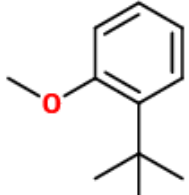
Compound Structure	Name and Source	Compound Number	Activity against H7 - IC50 -	Activity against H5 - IC50 -	Activity against VSVG - IC50 -
	2-tert-Butylphenol Fisher: AC10799-0025	7	25 μM	20 μM	75 μM
	2-tert-butyl-4-methylphenol Enamine: BBV-60752135	8	> 50 μM	> 50 μM	> 50 μM
	2-tert-butyl-4-ethylphenol Enamine: EN300-20846	9	> 50 μM	> 50 μM	> 50 μM
	4-bromo-2-tert-butylphenol Enamine: BBV-40206820	10	> 50 μM	> 50 μM	> 50 μM
	4-methoxy-3-tert-butylphenol USP: 1083008	11	0.6 μM	> 50 μM	> 50 μM
	2-tert-butyl-anisole Wardrop lab: NH-E1-220	12	> 100 μM	> 100 μM	> 100 μM

TABLE V (continued)

TBHQ and its derivatives

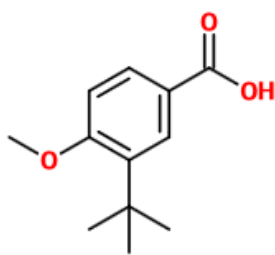
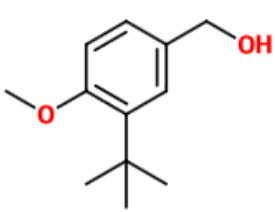
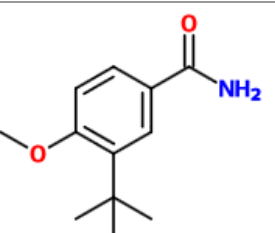
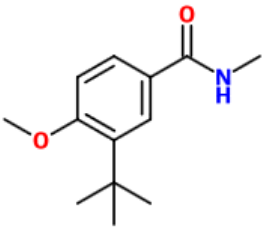
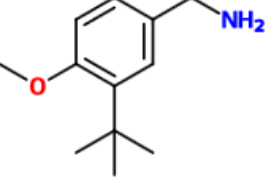
Compound Structure	Name and Source	Compound Number	Activity against H7 - IC50 -	Activity against H5 - IC50 -	Activity against VSVG - IC50 -
	3-tert-butyl-4-methoxybenzoic acid Wardrop lab: NH-E1-227	13	> 50 μM	> 50 μM	> 50 μM
	(3-tert-butyl-4-methoxy-phenyl) methanol Wardrop lab: NH-E1-229	14	10 μM	50 μM	> 50 μM
	3-tert-butyl-4-methoxybenzamide Wardrop lab: NH-E1-233	15	> 50 μM	> 50 μM	> 50 μM
	3-tert-butyl-4-methoxy-methylbenzamide Wardrop lab: NH-E1-231	16	> 50 μM	> 50 μM	> 50 μM
	3-tert-butyl-4-methoxybenzylamine Wardrop lab: NH-E1-237	17	30 μM	> 50 μM	> 50 μM

TABLE V (continued)

TBHQ and its derivatives

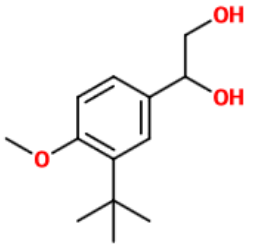
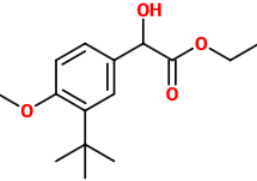
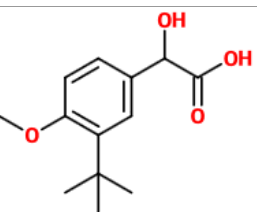
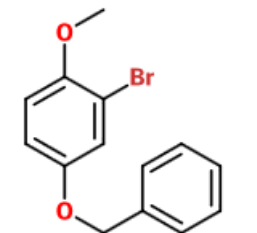
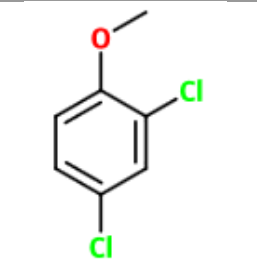
Compound Structure	Name and Source	Compound Number	Activity against H7 - IC50 -	Activity against H5 - IC50 -	Activity against VSVG - IC50 -
	Wardrop lab: NH-E1-244	18	> 50 μM	> 50 μM	> 50 μM
	Wardrop lab: NH-E1-245	19	> 50 μM	> 50 μM	> 50 μM
	Wardrop lab: NH-E1-246	20	> 50 μM	> 50 μM	> 50 μM
	Wardrop lab: NH-E1-10	21	~15 μM	>25 μM	>25 μM
	Wardrop lab: NH-E1-46	22	~15 μM	>25 μM	>25 μM

TABLE V (continued)

TBHQ and its derivatives

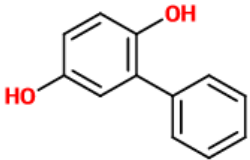
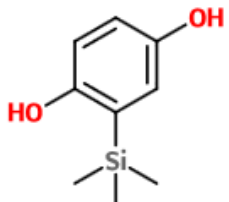
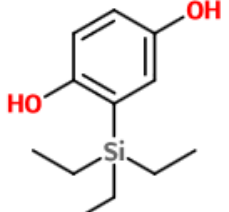
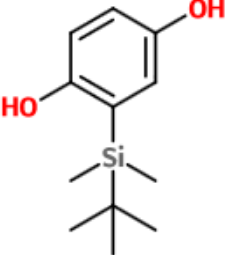
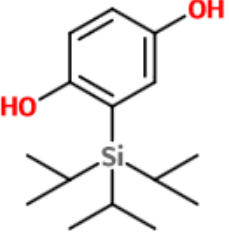
Compound Structure	Name and Source	Compound Number	Activity against H7 - IC50 -	Activity against H5 - IC50 -	Activity against VSVG - IC50 -
	2-Phenylhydroquinone Sigma: 227811-25G	23	> 100 μM	> 100 μM	> 100 μM
	(trimethylsilyl)hydroquinone Wardrop lab: DW-01-02	24	0.6 μM	> 50 μM	> 50 μM
	(triethylsilyl)hydroquinone Wardrop lab: NH-E1-08B	25	0.4 μM	~ 45 μM	> 50 μM
	(tert-butyl dimethylsilyl)hydroquinone Wardrop lab: NH-E1-03B	26	0.6 μM	> 50 μM	> 50 μM
	(triisopropylsilyl)hydroquinone Wardrop lab: NH-E1-06B	27	6 μM	12 μM	~ 35 μM

TABLE V (continued)

TBHQ and its derivatives

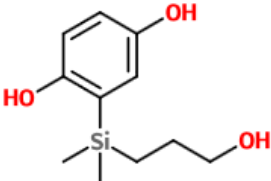
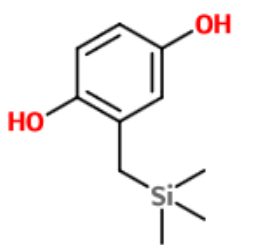
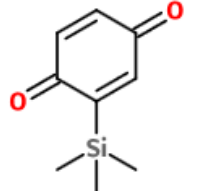
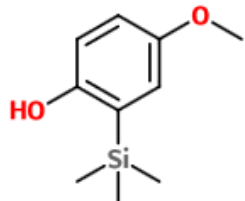
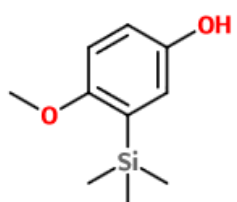
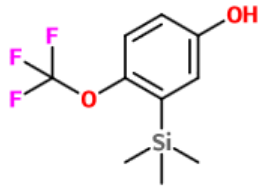
Compound Structure	Name and Source	Compound Number	Activity against H7 - IC50 -	Activity against H5 - IC50 -	Activity against VSVG - IC50 -
	Wardrop lab: NH-E1-31	28	0.6 μM	> 50 μM	> 50 μM
	Wardrop lab: NH-E1-29	29	1 μM	> 50 μM	> 50 μM
	(trimethylsilyl)-benzoquinone Wardrop lab: DJW-01-003	30	> 50 μM	> 50 μM	> 50 μM
	4-methoxy-2-(trimethylsilyl)-phenol Wardrop lab: DJW-01-006	31	> 50 μM	> 50 μM	> 50 μM
	4-methoxy-3-(trimethylsilyl)-phenol Wardrop lab: NH-E1-19B	32	0.1 μM	> 50 μM	> 50 μM
	Wardrop lab: NH-E1-45	33	0.1 μM	> 25 μM	> 25 μM

TABLE V (continued)

TBHQ and its derivatives

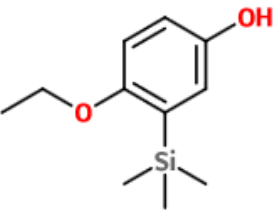
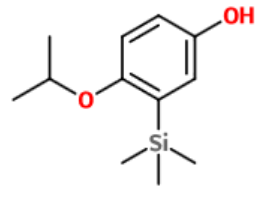
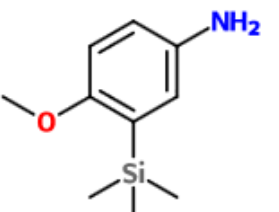
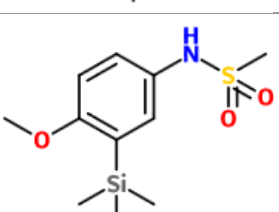
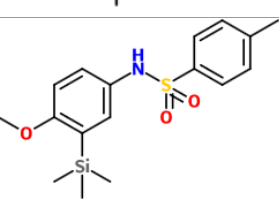
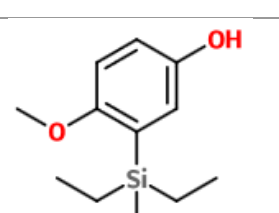
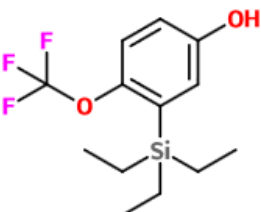
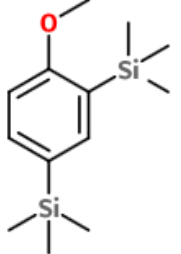
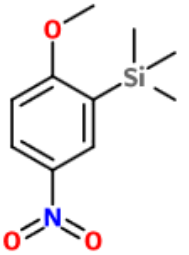
Compound Structure	Name and Source	Compound Number	Activity against H7 - IC50 -	Activity against H5 - IC50 -	Activity against VSVG - IC50 -
	Wardrop lab: NH-E1-43	34	0.6 μM	> 25 μM	> 25 μM
	Wardrop lab: NH-E1-48	35	0.8 μM	20 μM	30 μM
	Wardrop lab: NH-E1-52	36	15 μM	> 25 μM	> 25 μM
	Wardrop lab: NH-E1-55	37	> 25 μM	> 25 μM	> 25 μM
	Wardrop lab: NH-E1-59	38	20 μM	30 μM	30 μM
	Wardrop lab: NH-E1-65	39	0.8 μM	> 25 μM	> 25 μM

TABLE V (continued)

TBHQ and its derivatives

Compound Structure	Name and Source	Compound Number	Activity against H7 - IC50 -	Activity against H5 - IC50 -	Activity against VSVG - IC50 -
	Wardrop lab: NH-E1-66	40	4 μM	15 μM	25 μM
	Wardrop lab: NH-E1-49	41	~10 μM	>25 μM	>25 μM
	Wardrop lab: NH-E1-50	42	~10 μM	>25 μM	>25 μM

To test whether the antioxidant properties of TBHQ are related to its antiviral activity, we assayed the activity of three other common antioxidant food additives: ascorbic acid (compound **1**), propyl gallate (compound **2**), and 2,6-di-*tert*-butyl-4-methylphenol (compound **3**), using a H7 HA-based pseudovirus entry assay (Antanasijevic et al., 2013). In this assay, pseudovirus is prepared with the viral envelope protein of choice, H7 HA in the present case, contained on the background of the HIV core. In addition, we assayed compound activity against VSVG-mediated entry, an unrelated viral envelope protein, to assess specificity and cytotoxicity (Antanasijevic et al., 2013). As shown in Table V, the antioxidants exhibit little inhibition of HA-mediated entry ($IC_{50} > 10X$ that of TBHQ), which strongly suggests that TBHQ oxidizing properties are not responsible for its antiviral activity. Nonetheless, we note that the compound that exhibits measurable activity, compound **3** with $IC_{50} \sim 60 \mu M$, is structurally closest to TBHQ (compound **4**).

Under physiological conditions of pH, temperature and oxygen concentration, TBHQ (compound **4**) undergoes a reversible oxidation to form tert-butylbenzoquinone (TBBQ) (Figure 33.), which forms the basis of its antioxidant properties (Ooi et al., 2013). This transformation happens even in the standard PBS buffer (20 mM phosphate pH 7.4 + 150 mM NaCl) at room temperature as shown in Figure 34. (top left plot). In these experiments starting compound concentration was 200 μM . The time of half-life is ~ 20 hours for this compound. The process is somewhat inhibited by the addition of 0.5 μM H7 HA. Binding to protein most likely partially protects it from oxidation. Interestingly, the oxidation of TBHQ does not occur at pH 4.7 (20 mM acetate buffer + 150 mM NaCl), suggesting that the oxidation process under the assay conditions goes through phenoxy radical pathway (Figure 33. Bottom). At lower pH the probability of formation of phenoxide ion intermediates is much lower, resulting in higher compound stability in the reduced state.

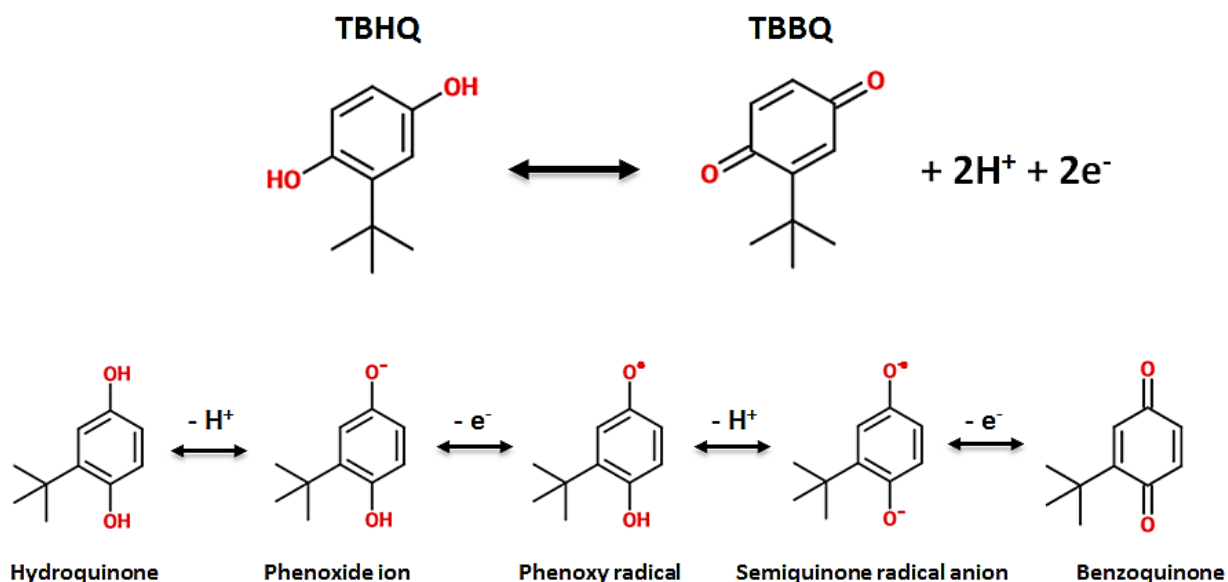


Figure 33. Redox chemistry of TBHQ. TBHQ undergoes reversible oxidation to form benzoquinone (top). One possible mechanism by which this reaction can take place (phenoxy radical pathway) is shown on the bottom.

On the other hand, the oxidized version of TBHQ (TBBQ, Compound **5**) is also unstable and it degrades over time into insoluble products through an unknown pathway. The presence of protein and pH 4.7 buffer did not seem to have any effect on the process (Figure 34. top right).

Thus, we compared the antiviral activity of TBHQ (compound **4**) to TBBQ (compound **5**). As shown in Table V, compound **5** exhibits little activity in the assayed concentration range, suggesting that one or more of the hydroxyl groups form critical interactions with HA. The crystal structure of TBHQ in complex with H3 HA supports this idea (Figure 35., adapted from Russell et al., 2008). Both hydroxyl groups are involved in formation of hydrogen bond network, where 1-OH acts as a hydrogen bond

acceptor (through its interaction with the main chain amide of HA2: Leu98) and 4-OH is a hydrogen bond donor (interacting with HA2: Glu57). The lack of activity in the case of TBBQ can be explained by its inability to form proper interactions with these residues.

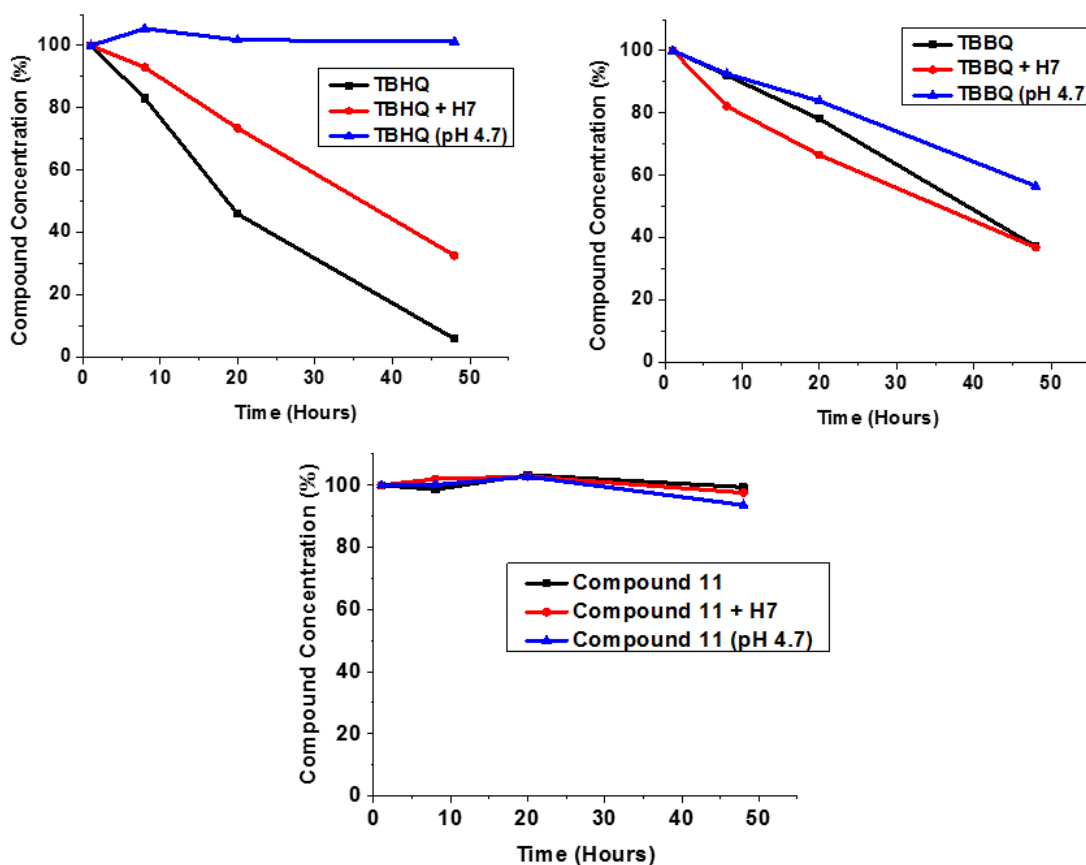


Figure 34. Stability of TBHQ, TBBQ and Compound **11**. 200 μ M solutions of TBHQ (top left), TBBQ (top right) and Compound **11** (bottom center) were used to test the stability of these compounds over time. The intensities of tert-butyl resonances in 1D NMR spectra were used to estimate the compound amounts at different time points. The stability was tested at pH 7.4 (black), in the presence of 0.5 μ M H7 HA (red) and at pH 4.7 (blue).

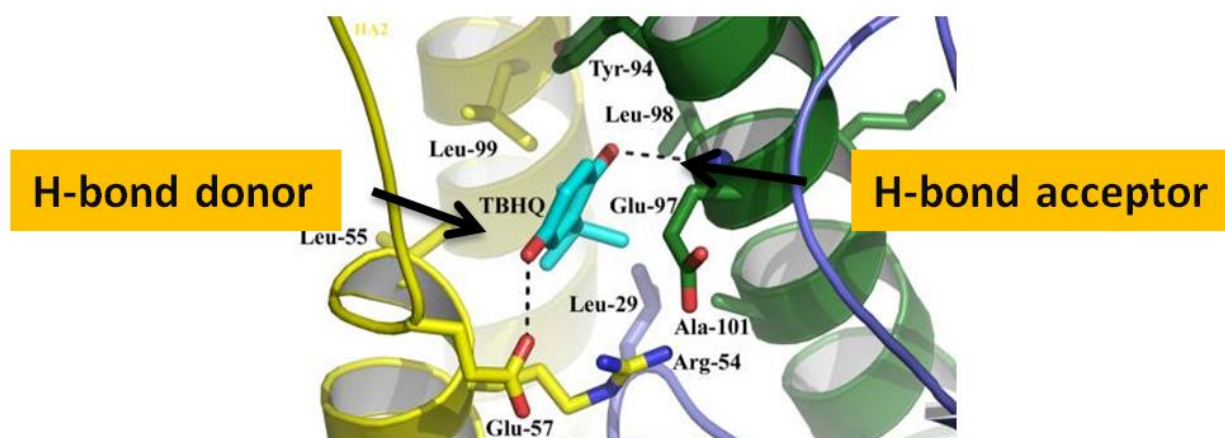


Figure 35. Structure of TBHQ in complex with H3 HA (adapted from Russell et al., 2008). In this figure the hydrogen bonding pattern of TBHQ in its binding site is shown.

In the next step, we assayed the importance of the 1-hydroxyl, and 4-hydroxyl groups of TBHQ for its antiviral activity. First, substitution of the 4-hydroxyl group with a methoxy group to form an anisole (compound **6**) significantly attenuates inhibition of virus entry (Table V), suggesting that the 4-hydroxyl group forms important contacts with HA. This notion is further supported by the decreased potency exhibited by compounds **7**, **8**, **9**, and **10**, in which the 4-hydroxyl group is substituted by hydrogen, methyl, ethyl and bromo groups, respectively (Table V). Next, replacement of the 1-hydroxyl group with a methoxy substituent to form an anisole (compound **11**) improves the IC₅₀ by ~10X, suggesting that the 1-hydroxyl group is not critical and that the newly introduced *O*-alkyl group makes significant favorable contacts with HA. Moreover, the importance of the 4-hydroxyl group is further supported by the observation that its substitution in the most active anisole derivative (compound **11**) by hydrogen, carboxylic acid, hydroxymethyl, amidyl, methylamidyl, and ethylamidyl groups (compounds **12**, **13**, **14**, **15**, **16** and **17**, respectively) exhibit significantly decreased activity. The same is also true for compounds with alcohol-like substituents at that position (compounds **18**, **19** and **20**). In conclusion, the data suggests that 1-hydroxyl group is a good site for substitutions that increase potency, while the 4-hydroxyl group seems to be essential for the activity of this compound. These findings are in excellent agreement with the crystal structure of TBHQ with H3 HA. In the structure, 1-OH group acts as a hydrogen bond acceptor while 4-OH group is a hydrogen bond donor.

Additionally, the stability of compound **11** was tested under identical conditions as done with TBHQ and TBBQ. The results are shown in Figure 34. (bottom center). The compound appears to be fully stable over long periods of time and under all conditions tested (pH 7.4, pH 4.7, ± H7 HA).

Given the increase in stability of TBHQ derivatives compared to the original compound we then wanted to test the effect this has on the cytotoxicity of the select group of compounds. For these

experiments, the CellTiter Glo kit was used to measure CC50 values for TBHQ (Compound **4**), TBBQ (Compound **5**), 1M-TBHQ (Compound **11**) and 4M-TBHQ (Compound **6**). The data is shown in Figure 36.

TBBQ (compound **5**) is the most toxic of the four compounds tested with a CC50 value of 72 ± 8 μM . Compound **4** (TBHQ) was at 270 ± 20 μM . Two methoxy-derivatives of TBHQ, compounds **6** and **11**, exhibited CC50 at 367 ± 25 μM and 335 ± 32 μM , respectively. The ~ 1.3 -fold decrease in cytotoxicity observed with these two compounds is most likely a consequence of the increased stability (Figure 34.).

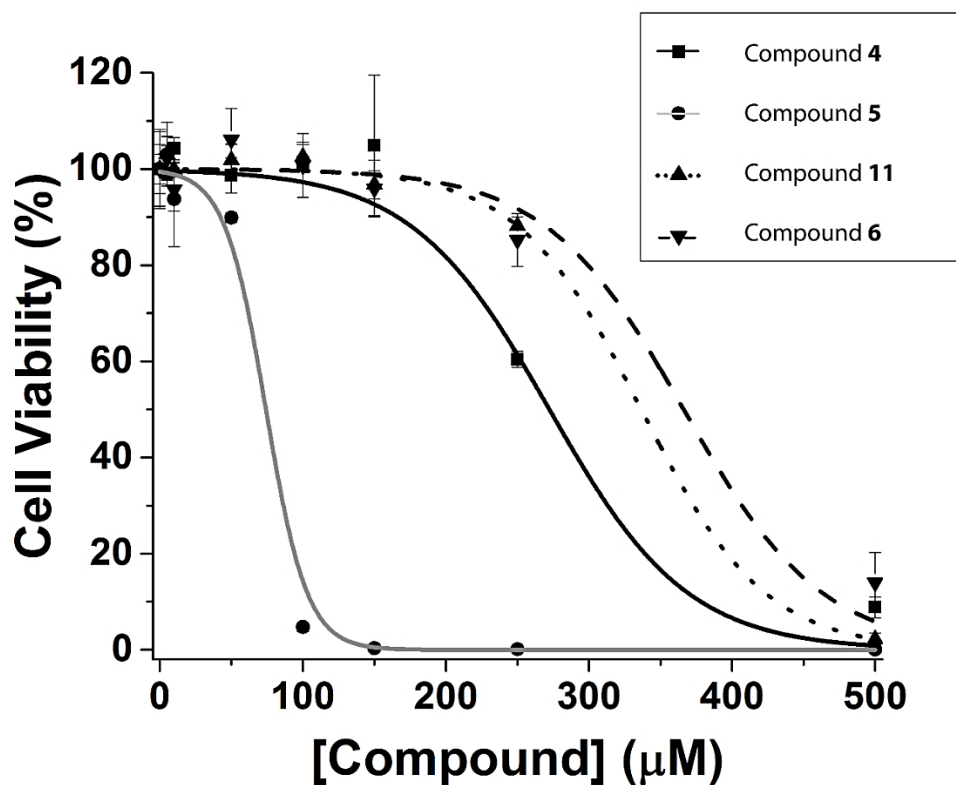


Figure 36. Cytotoxicity of compounds **4**, **5**, **6** and **11**. The cytotoxicity effect was measured on HEK293T cells using CellTiter-Glo kit, as described in the methods section. Three independent experiments were performed.

In a next step (in collaboration with Dr. Rama Mishra of NWU), we used 10 ns MDS to analyze the interaction patterns for several compounds of this series with the HA stem loop region of H7 HA. As shown in Figure 37.A, the model predicts that the 1-OH and 4-OH groups of TBHQ (compound **4**) form hydrogen bonds with the HA2-R54 main chain and the HA2-E97 side chain, respectively. In addition, the tert-butyl group forms hydrophobic interactions with the side chains of HA2-L55, HA2-L98 and HA2-L99 (Figure 37.A). In the case of our most active compound (compound **11**), the model predicts an almost identical orientation of the aromatic ring and tert-butyl groups with the most significant difference being the addition of hydrophobic interactions between the 1-methoxy group and the side chains of HA1-P284, HA1-F285, HA2-L55, HA2-L99 (Figure 37.B). In contrast, the predicted binding mode of compound **6**, a relatively inactive derivative of TBHQ, is very different. Specifically, the model predicts that the 1-OH of this compound forms a hydrogen bond with the HA2-E97 side chain and that the tert-butyl group loses the hydrophobic interaction with the HA2-L99 side chain (Figure 37.C). Finally, the predicted binding mode of compound **5**, another inactive derivative of TBHQ, is again very different (Figure 37.D). Specifically, the 1-carbonyl loses the ability to hydrogen bond, the carbonyl forms a new hydrogen bond with the HA2-Y94 side chain, and the tert-butyl group loses hydrophobic interactions with the side chains of HA2-L55 and HA2-L99.

Interestingly, a comparison between the x-ray structure of TBHQ with H3 HA and our model of TBHQ with H7 HA shows significant differences. The hydroquinone part of the molecule appears to have rotated by $\sim 180^\circ$ with respect to the tert-butyl tail (it remains in the same position). The 1-OH and 4-OH groups are facing in the opposite directions and forming hydrogen bonds with different residues (when comparing the structure and the model). Consequently, the predicted binding modes for compounds **6** and **11** would be very different between H3 HA and H7 HA, which should reflect on the activity. However, in our work we find excellent correlation between the H7 HA pseudovirus inhibition data and H3 HA pseudovirus and infectious virus inhibition data (see results below). Also, STD analysis of TBHQ

interactions with recombinant H3 and H7 HA didn't reveal any differences in binding modes (Figure 31. C and D). Altogether, our data suggests that the MD results should be taken with caution. However, until the X-ray structures of H7 HA with TBHQ daughter compounds are available (work in progress), these models provide valuable resources for chemical optimization process.

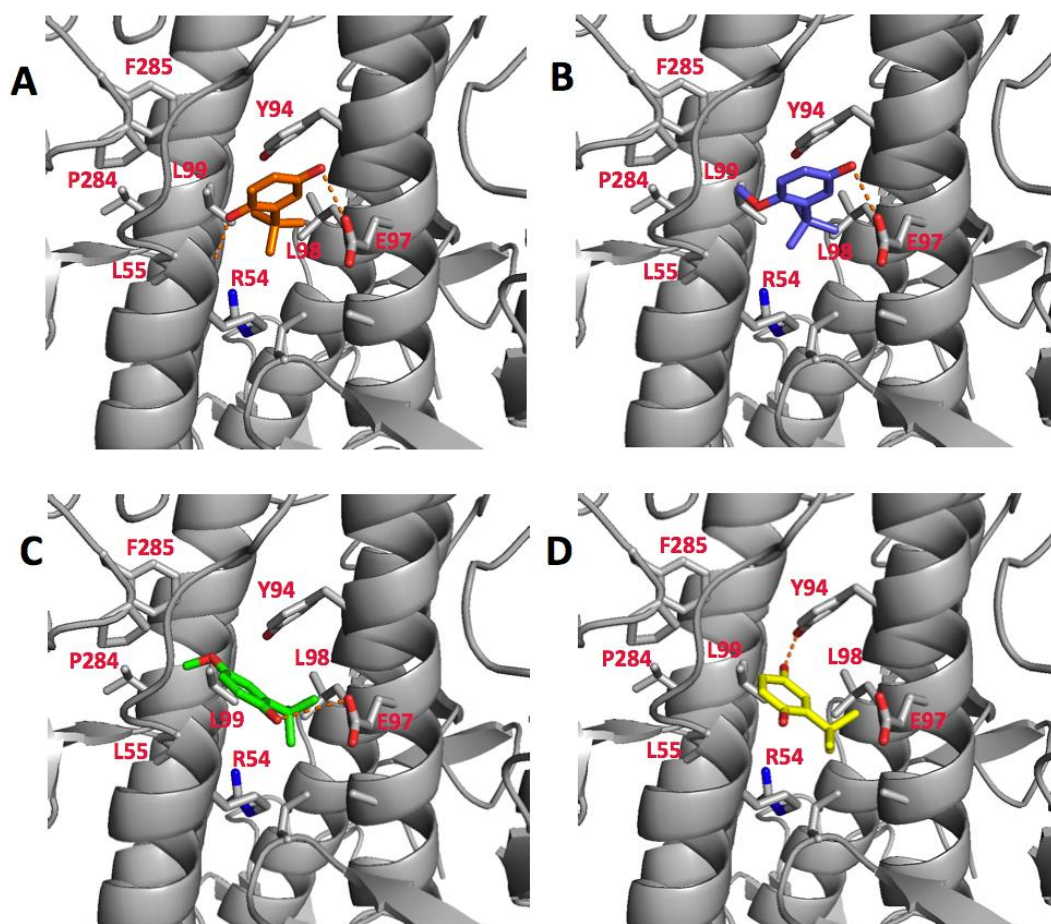


Figure 37. Molecular dynamics models of compounds with H7 HA highlighting important hydrogen bonding and hydrophobic interactions. The models shown include compound 4 (A), compound 11 (B), compound 6 (C) and compound 5 (D). Hydrogen bonding and hydrophobic contacts have been defined as $<4 \text{ \AA}$ distance between appropriate heavy atoms.

In the next steps, we decided to focus on the tert-butyl group. STD data for TBHQ interaction with H3 HA and H7 HA (Figure 31. C and D) shows that this group is not in a very good contact with the hydrophobic core of the binding pocket (it receives only $\sim 50\%$ STD, with respect to the aromatic ring ^1H). The crystal structure of TBHQ with H3 HA supports this idea and suggests that a slightly larger substituent would achieve much better hydrophobic interaction with the residues HA2: Leu98, Leu99, Ala101, and HA1: Leu29 (Figure 35.).

The first substituent tested was a phenyl group (compound **23**). This compound didn't show any detectable activity against H7 HA in the concentration range tested ($\text{IC}_{50} > 100\ \mu\text{M}$). This is most likely due to a very different nature of the phenyl group compared to tert-butyl. While the former has a more planar conformation caused by sp^2 hybridization, the latter is roughly cone-shaped (sp^3). Thus, we proceeded by introducing aliphatic modifications into the tert-butyl group.

Instead of the canonical aliphatic chain extension we decided to first substitute the tertiary carbon with silicon. Silicon has been used in place of carbon as a part of several different functional groups and in many drug candidates (Franz and Wilson, 2013). A number of Si-containing small molecule derivatives have passed into clinical trials and some of them went as far as phase III, proving their safety and appropriate pharmacokinetic properties (Franz and Wilson, 2013). Nevertheless, to this date none of these drug candidates have been approved for human application by the FDA.

Here we substituted the tert-butyl with a tri-methyl-silyl functional group. Silicon has a larger covalent radius and the C-Si bond is longer by $\sim 0.3\ \text{\AA}$ than the corresponding C-C bond (Table VI). Overall, the diameter of the resulting substituent group is increasing by $\sim 1\ \text{\AA}$ with the introduction of silicon, without a significant change in shape. Additionally, a decrease in electronegativity is expected stabilize the hydroquinone reactivity to a certain extent.

TABLE VI
The comparison of chemical properties of silicon and carbon

Property	Carbon	Silicon
Covalent Radius	0.77 Å	1.11 Å
Bond length	1.54 Å (C – C)	1.87 Å (C – Si)

Strikingly, the resulting compound **24** showed a 10-fold increase in activity against H7 HA compared to TBHQ with the IC50 value at 0.6 μ M. We tested if this increase was a consequence of a better hydrophobic contact of the tri-methyl-silyl group with the H7 HA binding pocket (compared to tert-butyl) by STD NMR. The results for both compounds are shown in Figure 38. In the case of the methyl groups the STD percentage values have increased from 51 % for tert-butyl to 73 % for tri-methyl-silyl substituent suggesting better hydrophobic contacts in the latter without disrupting the contacts of the aromatic ring.

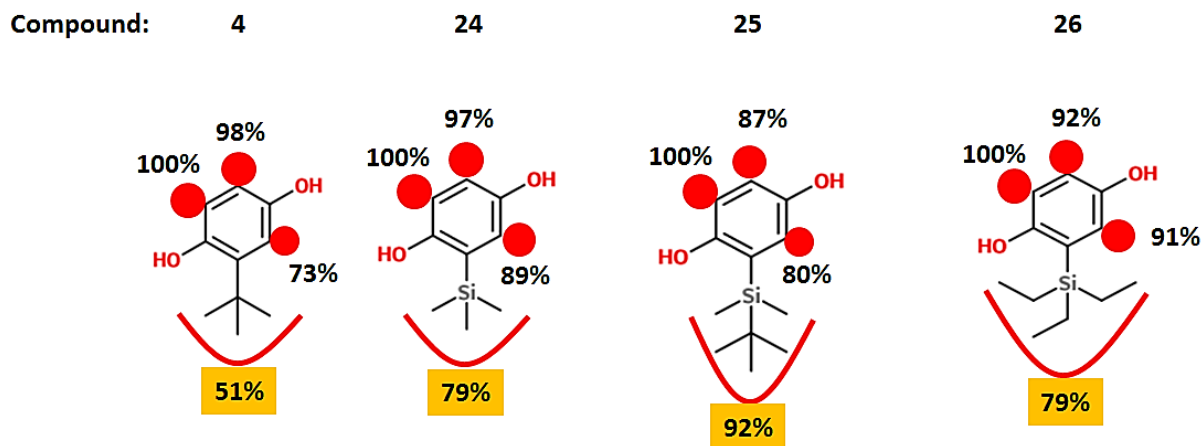


Figure 38. STD comparison of the interactions of H7 HA with compounds **4**, **24**, **25** and **26**. Experimental conditions were 50 μM compound + 0.5 μM H7 HA (buffer: 20 mM phosphate pH 7.4 + 150 mM NaCl in 100 % $^2\text{H}_2\text{O}$). Experiments performed with the on-resonance excitation at -2 ppm, while off-resonance excitation was at 45 ppm.

Encouraged by these results we wanted to test if we can increase the affinity and potency by further extension of the substituent group to tri-ethyl-silyl, tert-butyl-di-methyl-silyl and tri-isopropyl-silyl (compounds **25**, **26** and **27**, respectively). While compounds **25** and **26** maintained a very similar level of activity to compound **24** (IC_{50} values of 0.4 and 0.6 μM), compound **27** was already 10-fold less active compared to the former three compounds. Additionally, this compound displayed very unfavorable solubility properties and it showed higher cytotoxicity (based on the VSVG data). The stability data for the four compounds is shown in Figure 39. Introduction of silicon instead of carbon appears to reduce the tendency towards oxidation for all compounds (shown in black). For example, with respect of the parent compound TBHQ the $t_{1/2}$ of Compound **24** goes from ~ 20 h to ~ 50 h, under

identical conditions. The presence of protein further stabilizes the compounds (red) and low pH completely inhibits the oxidation process (blue) similarly to what was observed with TBHQ (Figure 34.).

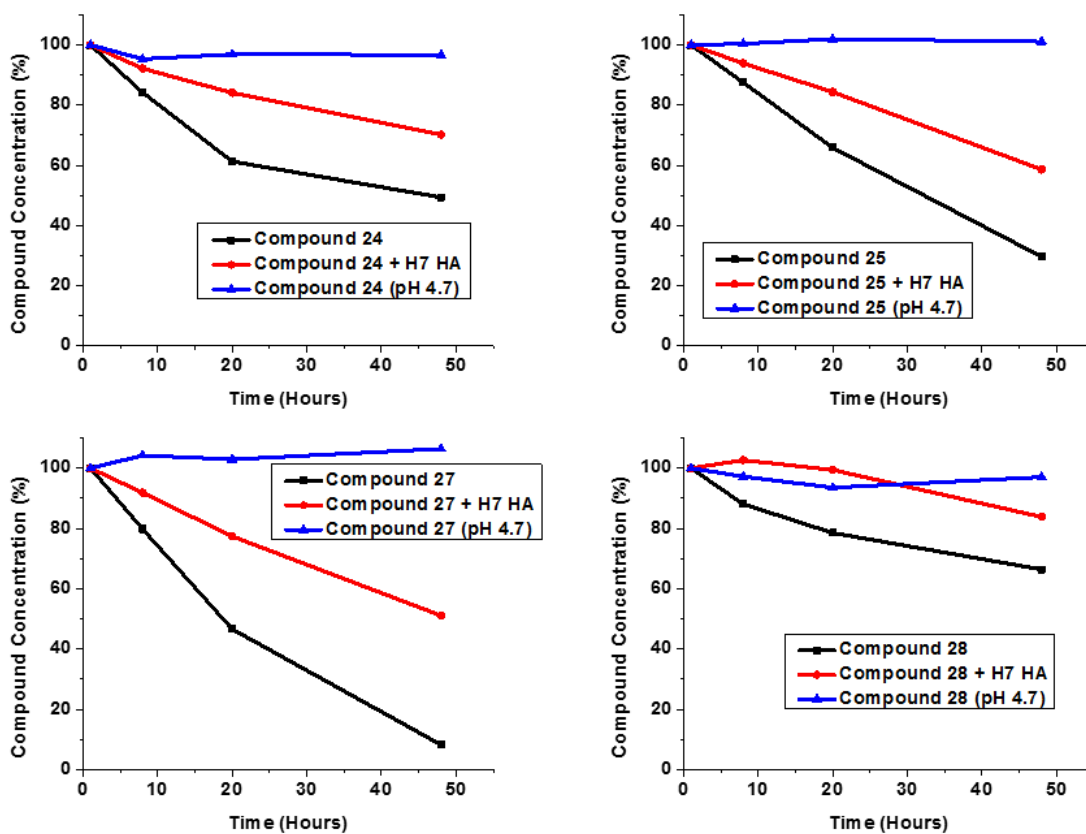


Figure 39. Stability of compounds **24**, **25**, **26** and **27** over time. The assay performed as described previously for TBHQ. 1D NMR experiments used to detect the amount of compound left in the sample.

We also determined STD percentages for compounds **25** and **26**. Data shown in Figure 38. implies a slightly better hydrophobic interaction with the substituent groups compared to compound **24** and a significantly better interaction than tert-butyl group (compound **4**). However, the increase in antiviral activity is only minor, suggesting that hydrophobic interaction is only a part of the interaction network giving the compounds their inhibitory action. For example, the longer chains of compounds **25** and **26** could be clashing with the binding pocket residues, which could neutralize the increased hydrophobic effect.

Two unstable precursor compounds (**28** and **29**), were also tested for their activity against H7 HA. These compounds display increased self-reactivity (compared to the other compounds from the TBHQ series), leading to the creation of insoluble products. Surprisingly, both of them showed very good inhibition of viral entry (IC₅₀ values ~ 0.6 – 1 μM) in a slightly modified version of the pseudovirus assay where the compounds were incubated with the cells and viruses for only ~ 4 hours. Despite the very informative nature of these datasets, the compounds were not considered further because of their poor chemical properties.

In the next step we wanted to test the importance of the hydroquinone OH groups for the inhibitory activity of TMSHQ (compound **24**), similarly to the tests done on TBHQ. Benzoquinone, 4-methoxy and 1-methoxy derivatives of TMSHQ were generated (compounds **30**, **31** and **32**). Their activities showed the same general trend as previously observed with tert-butyl versions of these compounds. Benzoquinone (compound **30**) was inactive and very cytotoxic. 4-methoxy derivative (compound **31**) was less active compared to its precursor compound **24**. On the other hand compound **32** (1M-TMSHQ) displayed very good activity against H7 HA virus that is higher than any other compound. The IC₅₀ value was 0.1 μM. Compound **32** was fully stable and showed 1.5 times lower cytotoxicity compared to the TBHQ parent (Figure 40. A and B). The CC₅₀ value determined after 24-

hour incubation with the compound was $(403 \pm 30) \mu\text{M}$. The therapeutic index for this compound is > 4000.

The STD binding mode (Figure 40.C) suggests that O-methyl group is susceptible to further extension, given that the STD % value was only 68 %. Three different options were tested in place of the methyl group: tri-fluoro-methyl, ethyl and isopropyl groups (compounds **33**, **34** and **35** respectively). Compound **33** showed the same activity as compound **32** ($\text{IC}_{50} \sim 0.1 \mu\text{M}$). Compound **34** was 6 times less active, suggesting that the ethyl group has less favorable steric properties when it comes to binding to H7 HA. Similarly, compound **35** was 8 times less active than compound **32**. Based on the activity data methyl and tri-fluoro-methyl groups appear to be the most suitable substituent groups in this position.

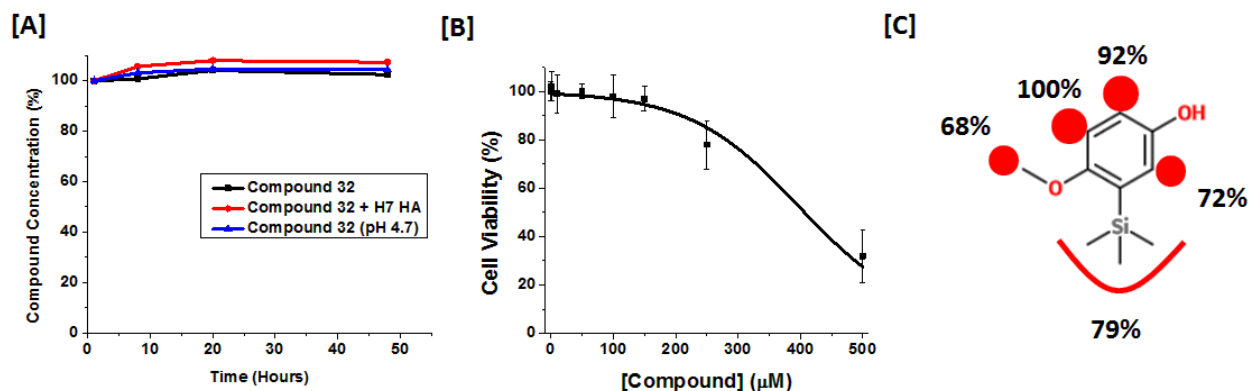


Figure 40. Stability and mode of binding of compound **32**. (A) Stability of compound **32** over time was monitored using 1D NMR experiments as previously described for other compounds. Compound shows full stability over 50 hours at room temperature and under all conditions (compound alone – black line, compound + H7 HA – red line, compound at pH 4.7 – black line). (B) Cytotoxicity of compound **32** was determined using CellTiter Glo kit. (C) STD percentages for compound **32** interacting with H7 HA. The conditions for were 50 μM compound **32** + 0.5 μM H7 HA.

Several other combinations of functional groups at positions 1-,2- and 4- (TBHQ numbering) were tested (compounds **36 – 42**) but the final products were always significantly less active compared to our best two derivatives (compounds **32** and **33**).

Several of the compounds from the TBHQ series were chosen to be tested for activity against the infectious H3 N2 virus (strain HK68). This work was done in collaboration with the lab of Dr. Balaji Manicassamy at the University of Chicago. The chosen compounds were: TBHQ parent (**4**), 4-methoxy derivative of TBHQ (**6**), 1-methoxy derivative of TBHQ (**11**), tri-methyl-silyl-hydroquinone (**24**), and the two most potent compounds (**32** and **33**). The experiments were done with the short incubation times corresponding to single cycle entry. We chose these types of assays for 2 reasons, (1) we wanted to see if there is a correlation between the infectious virus and pseudovirus data (pseudovirus experiments are also single cycle) and (2) compounds prone to oxidation, like TBHQ and TMSHQ, can also be tested in these assays. Nucleoprotein staining was used for detection of viral entry. The results are shown in Figure 41. and Table VII.

All 6 compounds displayed a dose dependent inhibition of the entry of H3 N2 virus. The activities determined here are in a relatively good correlation with the pseudovirus data (Table VII). IC50 values for each compound are generally higher compared to the IC50 values determined with non-infectious virus but still within the same order of magnitude for all compounds tested. The largest difference was observed for compound **11** where we see ~ 10 times less activity against the infectious virus. These discrepancies can be due to a number of factors including assay conditions and differences between H3 HA and H7 HA. Nevertheless, the good general agreement between the IC50 values is very encouraging.

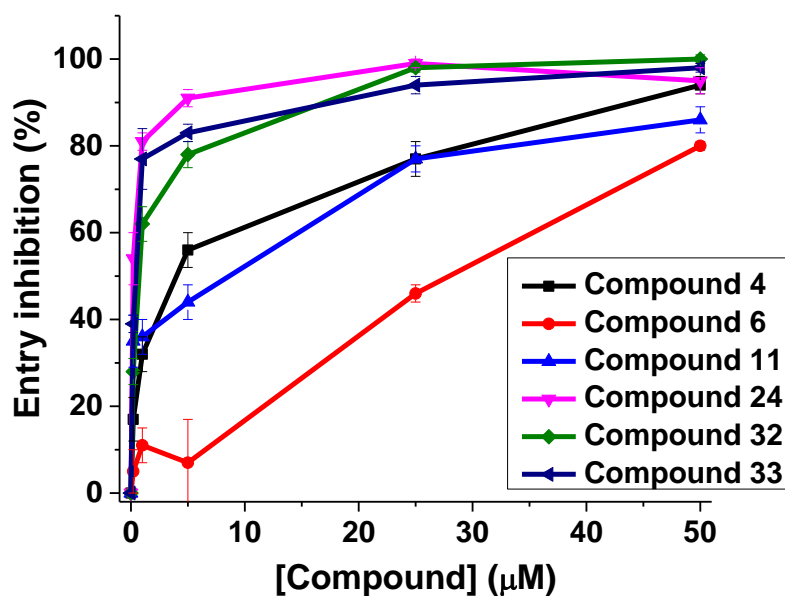


Figure 41. Activity of the compounds from TBHQ series against infectious H3 N2 virus. The experiments were performed as described in the Methods section. Entry inhibition plots for all 6 compounds are shown in different colors.

TABLE VII

Comparison of the results from the infectious virus and pseudovirus entry inhibition assays

Compound	IC50 (infectious H3N2) (μM)	IC50 (H7N1 pseudovirus) (μM)
4	4.8 ± 0.4	6 ± 1
6	27 ± 9	30 ± 10
11	6 ± 1	0.6 ± 0.2
24	0.20 ± 0.02	0.6 ± 0.1
32	0.7 ± 0.1	0.12 ± 0.03
33	0.35 ± 0.08	0.13 ± 0.02

Finally, we wanted to confirm that the derivative compounds are still binding to the same site as the parent TBHQ. We used the WaterLOGSY competition experiment for these tests. The binding of TBHQ to H7 HA was determined in the absence and presence of a select group of compounds. TBHQ was at 50 μM and the compounds (if present) were at 0.5 mM concentrations (10X excess). The competition data is shown in Figure 42.

The competition assays (Figure 42.) clearly show that the compounds from this series (at least the ones that were tested) are all sharing the same binding site on the H7 HA surface with the TBHQ parent. With the exception of compound **32**, there is a very good correlation between the predicted affinities of the tested compounds (based on their IC50 values) and the ability to compete with the TBHQ (based on the amount of WaterLOGSY signal).

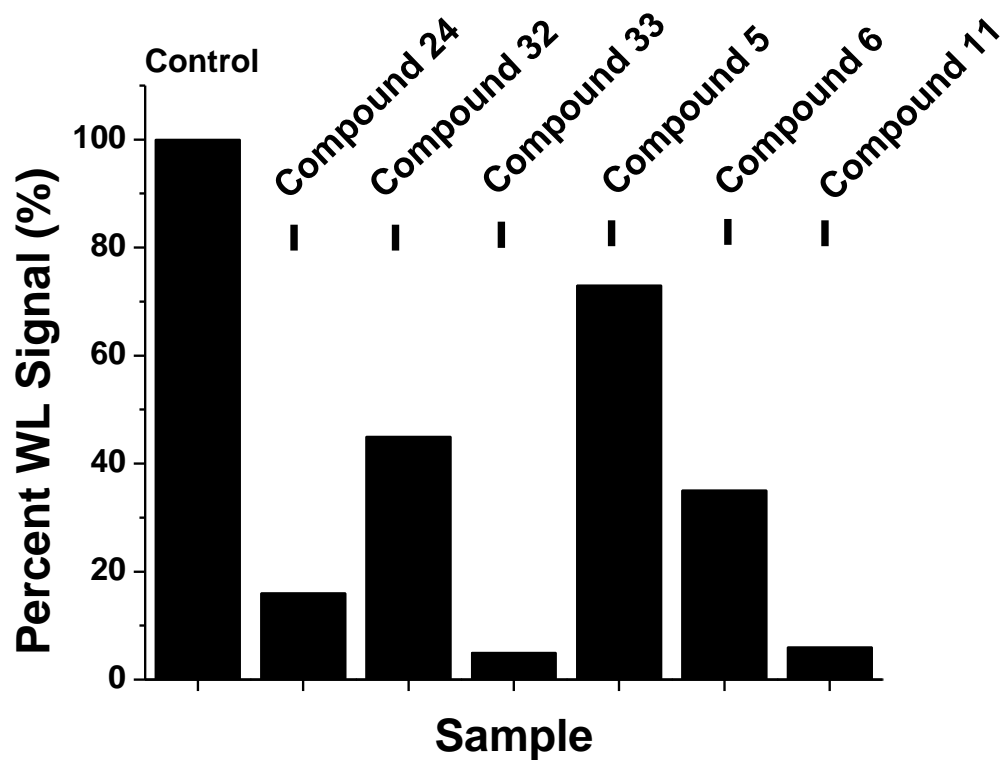


Figure 42. TBHQ competition assays. The binding of TBHQ to H7 HA was tested by WaterLOGSY. The signal intensity in the absence of any other compound was set to 100% (Control). Compounds **24**, **32**, **33**, **5**, **6**, and **11** were added in 10-fold excess and the amount of TBHQ signal in each case was normalized based on the control measurement.

Chapter 3.7 - NMR methods development: Comparison of the sensitivities of WaterLOGSY and STD NMR experiments

(Adapted from Antanasijevic et al., 2014b; see Appendix A)

To compare the sensitivities it is important to present the details for the WaterLOGSY and STD NMR experiments. For these experiments we chose standard pulse sequences depicted in Figure 43.A (Dalvit et al., 2001; Mayer and Meyer, 2001), which we have found to be relatively easy to implement and robust for studies designed to discover drug-like ligands, characterize their interaction, and guide chemical improvement (McCullough et al., 2012; Antanasijevic et al., 2013; Basu et al., 2013; Ramirez et al., 2014). It is also important to determine the experimental protocol to be used to fairly compare the two experiments. In this case we chose to make the total experimental time periods of the WaterLOGSY and STD experiments to be the same (i.e. each experiment was set up to take a total time of 12 hrs) with identical relaxation times, saturation times, and receiver gain values. As noted in the introduction, STD is a difference experiment that requires acquisition of one scan “on” resonance (i.e. selective excitation of the biomolecule ^1H) and a second scan “off” resonance (i.e. excitation in a region far from any biomolecule ^1H). Accordingly, we chose to run the WL experiments in a difference mode in which 50% of the experimental time used a sample containing the ligand and biomolecule (6 hr total) and 50% of the experimental time used a second sample containing only the ligand (6 hr total). We note that this approach is generally useful in the WL experiment because the ligand resonances, in the absence of biomolecule, are often of the opposite sign of those in the presence of the biomolecule and thus this control experiment is useful to avoid confusion between ligands that bind and those that do not bind (c.f. Ramirez et al., 2014). Moreover, in WL the exchangeable ^1H of the ligand are often the opposite sign of the nonexchangeable ^1H in the absence of biomolecule and thus the difference spectra removes them from consideration. For these studies we have chosen three ligand-biomolecule systems, in which the

molecular weights of the biomolecules are >50 kDa, a realm where ligand-based methods present distinct advantages to target-based methods (Carlomango et al., 2005). Moreover, both the WL and STD experiments are based on an intermolecular NOE and the maximum NOE is expected to occur at $\tau_c > 10$ nsec and thus all three systems are expected to exhibit optimal NOE efficiency. The first system under study is that of the KET-BSA interaction. This interaction is of physiological significance because KET is a widely prescribed NSAID, which is transported in plasma via its interaction with HSA, the human analog of BSA (Bi et al., 2010). BSA is a 67 kDa monomer with an estimated $\tau_c \sim 40$ nsec and the K_d of its interaction with KET is $\sim 0.3 \mu\text{M}$ (Sowell et al., 2001). The second system under study is that of the TBHQ-HA interaction. As noted above, TBHQ is a promising small molecule inhibitor of influenza entry that binds to the stem loop region of HA (Antanasijevic et al., 2013). HA is a 210 kDa trimer with an estimated $\tau_c \sim 120$ nsec and the K_d of its interaction with TBHQ is $\sim 6 \mu\text{M}$ (Antanasijevic et al., 2013). The final system under study is that of the CAM-70S interaction. This interaction is of physiological significance in that CAM is considered as the prototypical broad-spectrum antibiotic that targets the peptidyl transferase site of the ribosome (Schlünzen et al., 2001). In contrast to the other systems under study, 70S is a complex of RNA and protein subunits with a molecular weight of 2500 kDa, an estimated $\tau_c \sim 1500$ nsec, and the K_d of its interaction with CAM is $\sim 2 \mu\text{M}$ (Mamos et al., 2013). For reference, the structures of the ligands and ^1H nomenclature used herein are shown in Figure 43.B.

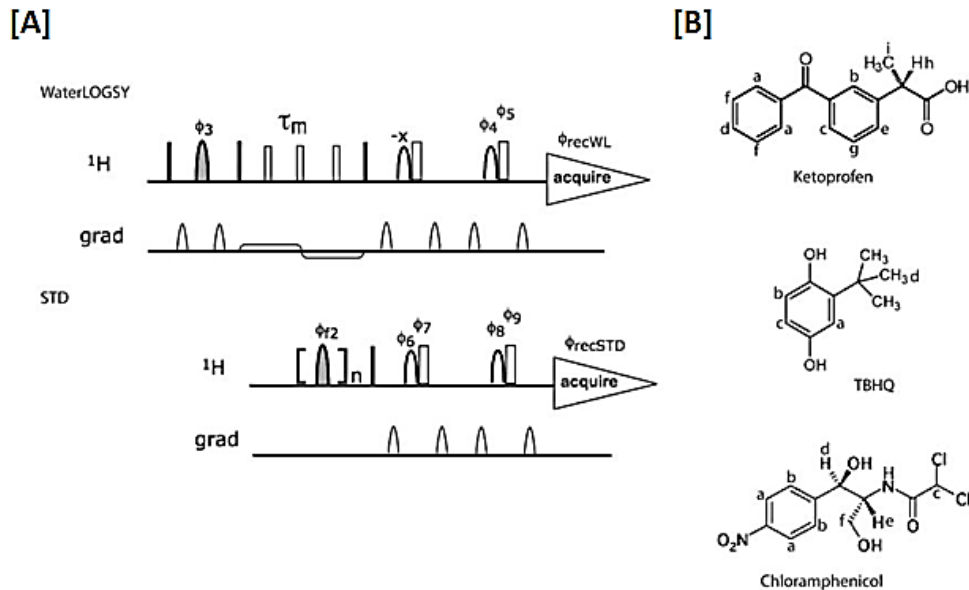


Figure 43. WaterLOGSY and STD pulse sequences and the compounds used in the experiments. [A] Pulse sequence diagrams for the STD and WaterLOGSY experiments with water suppression by the double-pulsed field gradient spin echo method. The solid bars and boxes represent hard 90° and 180° rf pulses, respectively. For STD after the initial d_1 relaxation delay, proton magnetization is saturated either on or off resonance by a train of 50 msec Gauss pulses, indicated by the shaded shaped pulse in brackets. Typical saturation times are 1-2 sec. In the final two echo periods, the shaped 180° pulse has a sinc shape with a duration of 2.2 msec; gradient strengths are 12 and 15 G/cm, respectively. For WaterLOGSY, these same parameters are used. The shaded shaped pulse is a 10 msec iBurp2 pulse that selectively inverts water magnetization; the gradients surrounding this pulse have a strength of ~ 20 G/cm. The mixing period (τ_m) is usually 1 or 2 sec in duration; during this period a weak bipolar gradient is applied to suppress radiation damping. Also, hard 180° pulses are applied in the mixing period to remove artifacts. For both experiments, d_1 , the relaxation delay, is 2.5 sec, and the total acquisition time is ~ 4 sec. Phase cycling: $\phi_2 = x$; $\phi_3 = x,x,y,y$; $\phi_4 = -x,-x,-y,-y$; $\phi_5 = x,x,x,x,y,y,y,y$; $\phi_6 = -x,-x,-x,-x,-y,-y,-y,-y$; $\phi_{recSTD} = x,-x,-x,x,-x,x,x,-x$; $\phi_7 = x,-y,-x,y$; $\phi_8 = -x,-x,-x,-x,y,y,y,y,x,x,x,x,-y,-y,-y,-y$; $\phi_9 = x,x,x,x,-y,-y,-y,-y,-x,-x,-x,-x,y,y,y,y$; $\phi_{recWL} = x,-x,x,-x,-x,x,x,-x$. All other rf pulses are applied with phase along the x-axis. The pulse sequence program for the WaterLOGSY experiment is available from the authors by request. [B] Ligands used in this study with the 1H nomenclature shown.

Finally, it is of interest to consider the protein saturation to be achieved in the STD experiment, which will be a function of frequency and field strength of the selective saturation pulses (Mayer and Meyer, 2001; Cutting et al., 2007; Ley et al., 2014). With respect to the frequency we have chosen a standard value of -0.5 ppm for the “on” frequency, which is a balance between achieving selective saturation of protein ^1H (and not ligand ^1H) at a particular saturation field strength. Recently it has been shown that the STD signal is insensitive to the pulse angle at a given field strength (Cutting et al., 2007). To test this observation, we compared the relative signal intensities of the downfield and upfield spectral regions of BSA using different Gaussian pulse angles at a field strength of 100 Hz in the STD experiment without ligand. As shown in Figure 44.A, no significant differences in protein saturation are observed for pulse angles ranging from 90° to 720° . We next tested the use of higher power selective pulses, which have recently been shown to increase S/N of the STD experiment in select cases (Cutting et al., 2007; Ley et al., 2014). Consequently, we compared the saturation of BSA in the STD experiment using selective Gaussian pulses with a field strength of 240 Hz versus the 100 Hz power used in the above experiment. We found that increasing the power to 240 Hz did indeed increase the protein saturation by a factor of ~ 3.5 (data not shown); however, as shown in Figure 44.B the increased power resulted in an unacceptable amount of ligand excitation, which would require an additional STD control experiment on ligand alone, thereby increasing experimental times by a factor of 2. Thus, we feel that selective pulses with field strengths of 100 Hz offer the optimal combination of saturation efficiency and selectivity in the STD experiment.

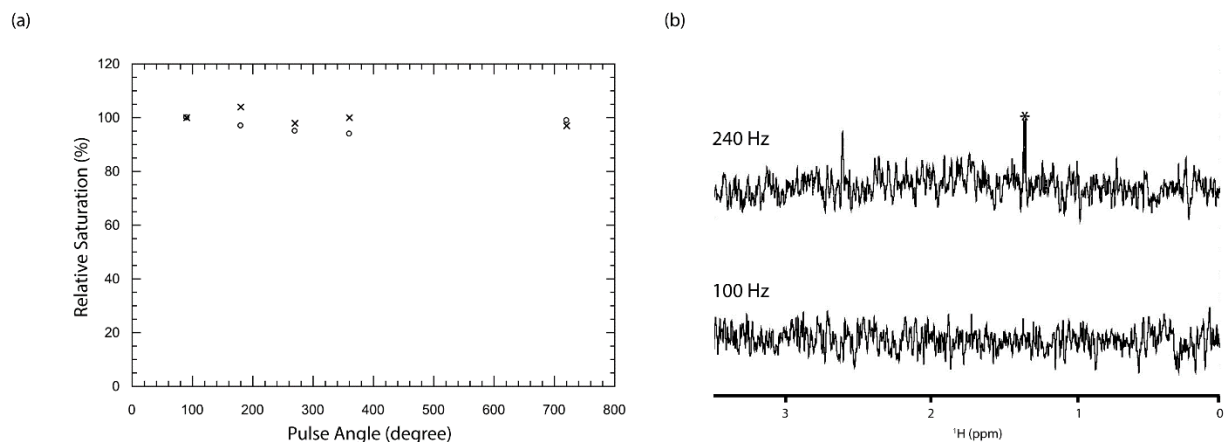


Figure 44. Optimization of the STD parameters. (A) Protein saturation using Gaussian selective pulses of various angles at field strength of 100 Hz and 2 sec of total saturation time. The saturation pulses correspond to 6.25, 12.5, 18.75, 25, and 50 msec, which correspond to pulse angles of 90°, 180°, 270°, 360° and 720°, respectively. Relative saturation for the downfield (>4.7 ppm,) and upfield (<4.7 ppm) spectral regions were estimated using the TopSpin 3.2. The experimental conditions were 40 μM BSA in 20 mM PBS/pH 7.4, 150 mM NaCl and 10% $^2\text{H}_2\text{O}$ at 25°C. (B) STD saturation of ligand in the absence of biomolecule at field strengths of 100 and 240 Hz with the KET resonance denoted by an asterisk. Experimental conditions were 300 μM KET in 20 mM PBS/pH 7.4, 150 mM NaCl and 10% $^2\text{H}_2\text{O}$ at 25°C.

In the next step, we carefully compared the STD and WL signals for biomolecule-ligand interactions for our 3 systems. In Figure 45., we give examples of the STD and WL spectra with 1 sec and 2 sec saturation or mixing times, respectively. First note that increasing the saturation or mixing time from 1 sec to 2 sec does appear to only modestly increase the signal intensities observed in both the STD and WL experiments, suggesting that by 1 sec we are observing optimal signals. Importantly, it is obvious that for a given amount of experimental time that the WL experiment is significantly more sensitive than the STD experiment for all 3 systems, which range from 67 kDa to 2500 kDa.

We next quantified the differences in the S/N of the STD and WL spectra for different ligand resonances in Figure 46. and Table VIII. Note that we assume that we are monitoring the same binding event in both experiments (i.e. the same site with the same ligand residence time). Consequently, individual differences in T₁, T₂ and intramolecular spin diffusion for ¹H within a particular ligand are expected to not be relevant when comparing the ratio of the 2 experiments at the same saturation or mixing times. In the case of KET-BSA, the ratio of WL to STD sensitivity ranges from 3.3 to 3.7 with averages of 3.2 ± 0.1 and 3.5 ± 0.2 for the 1 and 2 sec experiments, respectively. In the case of TBHQ-HA, the ratio of WL to STD sensitivity ranges from 11 to 19 with averages of 16 ± 4 and 12 ± 5 for the 1 and 2 sec experiments, respectively. In the case of CAM-70S, the ratio of WL to STD sensitivity ranges from 8.9 to 23 with averages of 16 ± 9 and 14 ± 6 for the 1 and 2 sec experiments, respectively. Recently, it has been shown that “off” saturation at 50 ppm may not be appropriate for very large biomolecules (e.g. viruses) due to large ¹H linewidths (Rademacher et al., 2008). Accordingly, we performed an additional STD experiment on the CAM-70S system using “off” saturation at 300 ppm. In this case, there were no significant differences in the intensities of the ligand resonances, suggesting that the STD experiment was not attenuated by the use of an inappropriate “off” frequency (data not shown).

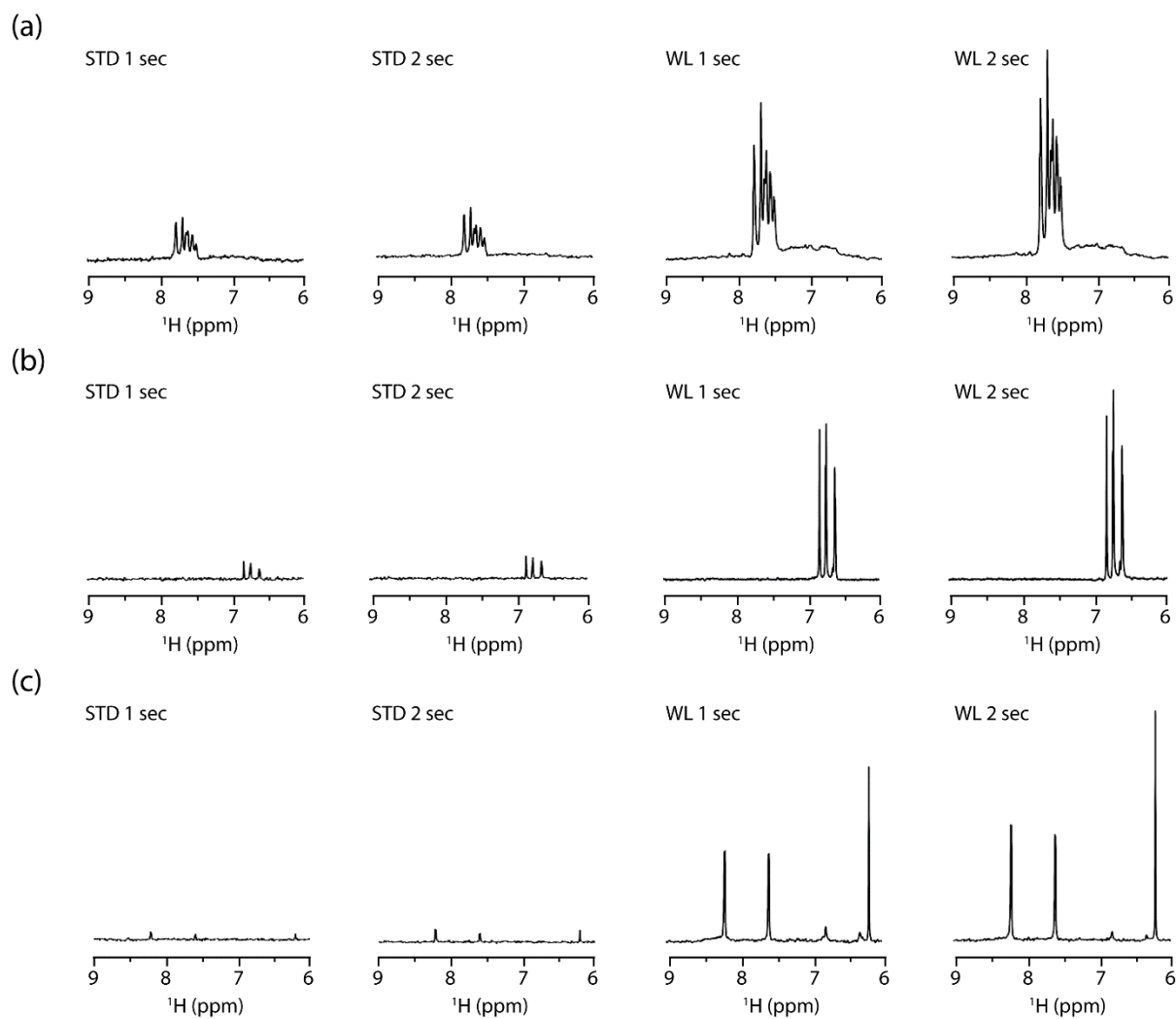


Figure 45. Comparison of WaterLOGSY and STD spectra. Examples of WaterLOGSY and STD spectra used to compare sensitivities for (A) KET-BSA, (B) TBHQ-HA and (C) CAM-Ribosome 70S. In all cases the relaxation delays, saturation/mixing times, receiver gain and total experimental times were identical

Interestingly, the sensitivities of the KET-BSA signals are relatively uniform in contrast to the TBHQ-HA and CAM-70S sensitivities. As noted in the introduction, the STD signal comes from magnetization transfer from biomolecule ^1H and the WL signal comes from magnetization transfer from transiently bound water ^1H or indirectly via nonexchangeable and exchangeable ^1H of biomolecules. Consequently, relatively lower WL to STD sensitivity would be expected for ligand ^1H in close proximity to hydrophobic regions of the biomolecule (e.g. with methyl or aromatic groups) and relatively higher WL to STD sensitivity would be expected for ligand ^1H in close proximity to transiently bound water or exchangeable groups of the biomolecule (i.e. hydrophilic regions). Thus, it is not surprising that the ratio of sensitivities varies for the ^1H of a particular ligand. Nonetheless, we find that WL is more sensitive than STD for all ligand ^1H in all of the model systems studied. We note, however, that the STD signal has been reported to be increased on the order of $\sim 2\text{X}$ by running the experiments in 100% $^2\text{H}_2\text{O}$, due to reduced spin diffusion between the biomolecule ^1H and bulk water ^1H (Mayer and James, 2002; Cutting et al., 2007). Accordingly, we performed the STD experiments in 100% $^2\text{H}_2\text{O}$ for our larger 2 systems (TBHQ-HA and CAM-70S). We found that the STD signals increased by a factor of $\sim 6\text{-}7\text{X}$ (data not shown); however, the WL experiments remain significantly more sensitive, suggesting that only part of the sensitivity difference can be achieved in 100% $^2\text{H}_2\text{O}$. Moreover, a number of recent improvements to the WL experiment have been reported to achieve S/N gains of $\sim 2\text{X}$ (Gossert et al., 2009). Finally, we note that buffer substitution will not always be feasible for labile or *ex vivo* systems (e.g. viruses or cells).

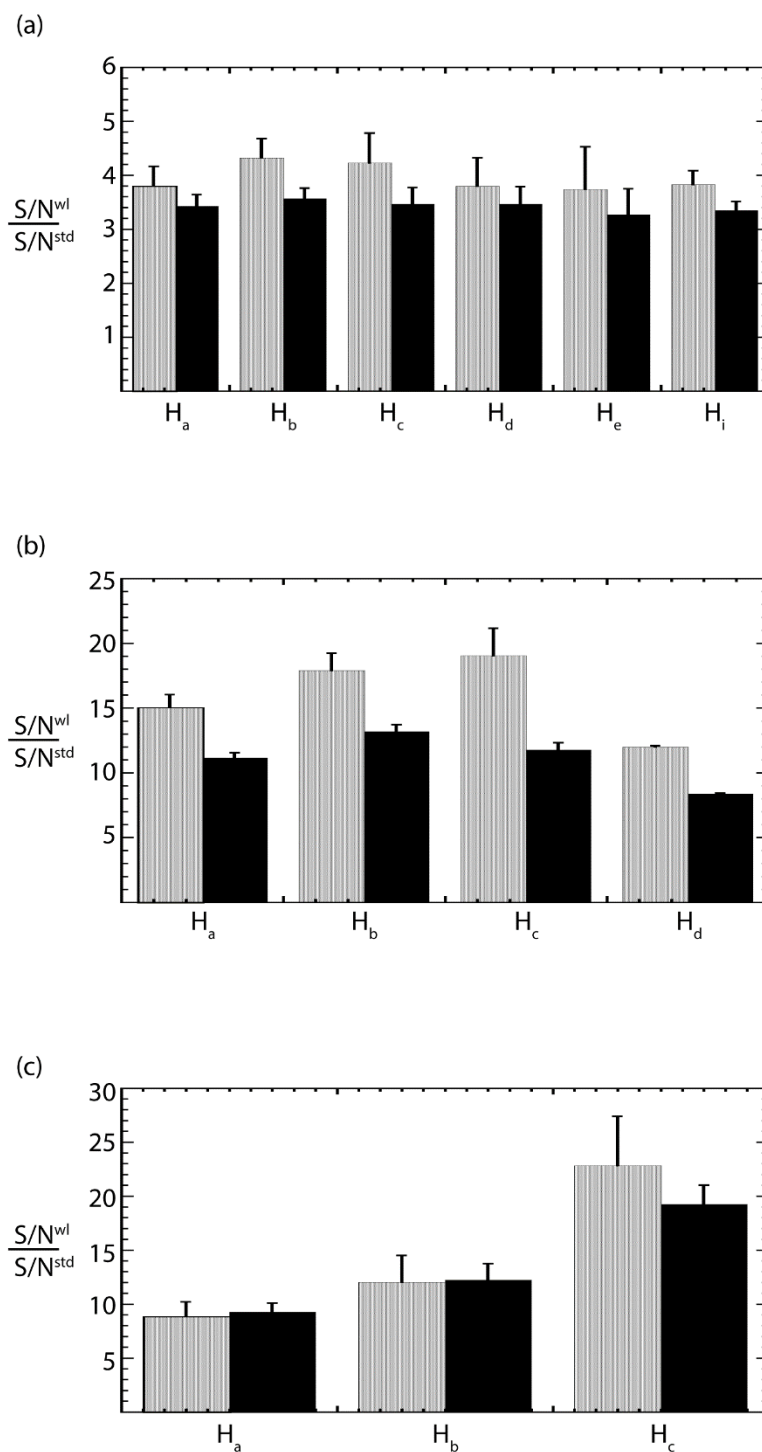


Figure 46. Quantified differences in sensitivities of individual resonances in the WaterLOGSY and STD NMR experiments. Resonances follow the nomenclature presented in Figure 43.B. Light bars represent 1 sec saturation/mixing times and dark bars represent 2 sec saturation/mixing times. Error bars have been estimated from the noise of the final spectra as described in the methods section.

Table VIII
Average $S/N^{wl}/S/N^{std}$.

System	$S/N^{wl}/S/N^{std}$ (1 sec)	$S/N^{wl}/S/N^{std}$ (2 sec)	n
KET-BSA	3.22 ± 0.12	3.45 ± 0.17	6
TBHQ-HA	15.6 ± 4.1	11.8 ± 5.4	4
CAM-Ribosome 70S	16.2 ± 8.6	14.2 ± 5.9	3

The differences in relative sensitivity between WL and STD could be due to a number of factors including the efficiency of protein saturation or partial excitation of biomolecule ^1H that resonate near $^1\text{H}_2\text{O}$ (e.g. $^1\text{H}\alpha$). To test the relative efficiency of protein saturation we compared the STD signal of BSA in the absence of ligand to the difference spectra between a WL experiment in which water ^1H were inverted to the $-z$ axis and a second WL experiment in which water ^1H remained along the $+z$ axis. As shown in Figure 47.A, the upfield spectral region of BSA exhibits significantly more saturation in the WL experiment than the STD experiment for identical experimental conditions. Moreover, the WL experiment appears to achieve more uniform saturation within the biomolecule. Taken together, this observation suggests that the higher S/N of the WL is at least partially due to indirect magnetization transfer via biomolecule ^1H to ligand ^1H . Next, we assessed the effect of partial saturation of $^1\text{H}\alpha$ in the WL sequence by performing the experiment in 100% $^2\text{H}_2\text{O}$. As shown by Figure 47.B, no detectable saturation of BSA is achieved in the absence of $^1\text{H}_2\text{O}$ and thus the protein saturation of the WL experiment is clearly mediated by $^1\text{H}_2\text{O}$ (and possibly exchangeable ^1H), as previously noted by Dalvit and co-workers (2001).

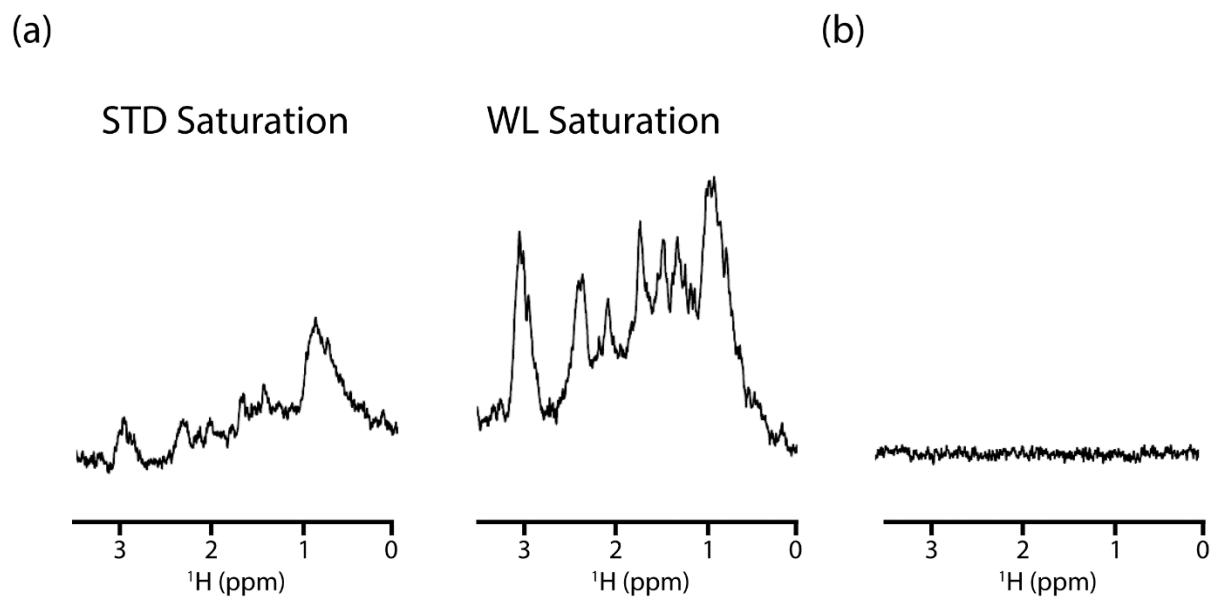


Figure 47. Protein saturation in WL and STD experiments. Comparison of BSA saturation efficiencies. (A) Relative protein saturation using STD saturation at 100 Hz power and WaterLOGSY saturation. (B) Relative protein saturation using WaterLOGSY saturation in the absence of water ^1H . The experimental conditions were 40 μM BSA in 20 mM PBS/pH 7.4, 150 mM NaCl and 10 % $^2\text{H}_2\text{O}$ in (A) and 100 % $^2\text{H}_2\text{O}$ in (B) at 25 $^\circ\text{C}$.

Chapter 3.8 - NMR Methods Development: Application of virus-like particles (VLP) to NMR characterization of viral membrane protein interactions

(Adapted from Antanasijevic et al., 2016; see Appendix A)

As discussed above, we characterized the interaction of a small molecule inhibitor of influenza entry, MBX2329, with recombinant H5 HA by WL and STD NMR (Basu et al., 2014). MBX2329 is a fusion inhibitor that selectively disrupts the entry of Group 1 HA influenza viruses, like H1 and H5 HA, with IC50 values in the low μM range by binding to HA and inhibiting a critical pH dependent conformational change (Antanasijevic et al., 2014a; Basu et al., 2014). In the present work we wanted to extend our NMR studies using HA embedded in VLP to ascertain the potential use of VLP for drug discovery and optimization studies; however, we had concerns about potential small molecule interactions with contaminants present in VLP preparations. For example, standard cell media contains 10 % Fetal Bovine Serum (FBS), which results in ~ 4 mg/ml of total protein added. The relatively high levels of added protein could potentially form detectable non-specific interactions with the small molecule of interest. Consequently, we first tested whether MBX2329 exhibits binding to proteins present in FBS. For this assay we chose to use WL NMR, which we have shown to be significantly more sensitive than STD NMR (Antanasijevic et al. 2014b). In this experiment, the presence of positively phased signals of the small molecule, in the presence of large molecular weight biomolecules, is due to binding. As shown in Figure 48., MBX2329 exhibits detectable binding to serum proteins at 2 and 10 % levels. Consequently, the relative purity of VLP preparations and the potential presence of contaminating soluble proteins is a significant concern for biochemical and biophysical studies.

In the next step, we prepared VLP containing H5 HA using a HIV core background by co-transfection of plasmids containing H5 HA and the HIV core, as previously described (Antanasijevic et al., 2014a). Note that in these preparations, a small amount of plasmid containing N1 NA was included (final

protein ratio of ~1:10 NA to HA) to enhance production of VLP containing HA (HA binds to sialylactose present on the cell surface, which inhibits virus egress). Subsequently VLP were harvested by collecting the cell supernatant from transfected cells and concentrated using ultrafiltration. Samples were then subjected to purification by sucrose gradient centrifugation, the standard protocol employed for the purification of VLP samples used in biochemical and biophysical studies (Haselhorst et al., 2008; Mohan et al., 2010; Garcia et al., 2014). We then analyzed the proteins present by SDS-PAGE as shown in Figure 49. First, a large amount of protein is present in the starting cell culture media. Moreover, the VLP proteins present in the initial purification step are undetectable at this point and thus are a very small fraction of the total protein. In contrast after the sucrose gradient step, the VLP proteins become detectable after this step; however, they remain a relatively small fraction of the total protein present (typically <15 %). As a consequence, we added gel filtration chromatography as an additional purification step. As shown in Figure 49., the viral proteins have now become predominant, consisting ~70 % of the total protein, and thus this preparation of VLP is clearly more appropriate for biochemical biophysical and biochemical characterizations. Using the 3-step purification protocol (concentration, sucrose gradient centrifugation, and gel filtration), we collect 0.5 ml of purified and concentrated stock from ~80 ml of starting VLP-containing supernatant. In the final preparation, the average p24 levels (i.e. the HIV core) were 10 $\mu\text{g/ml}$ (~400 nM) and the amount of HA was estimated to be 2 $\mu\text{g/ml}$ (~30 nM). One VLP on average has ~3000 p24 molecules (Jennings et al. 2005) and thus using these numbers we calculate that there are approximately ~75 HA trimers per VLP (and ~6 NA tetramers), which is in a good agreement with the literature values reported for different types of VLP with the HIV background (ranging between 10 and 100 viral membrane proteins per VLP (Crooks et al. 2000; Berkower et al. 2004; Zhu et al. 2006)).

In the next step, we purified VLP containing only NA for use as controls and subsequent characterization of membrane embedded NA. In this case the final concentration of NA was 4 $\mu\text{g/ml}$

(~60 nM), which corresponds to ~120 tetramers of NA per VLP. Finally, we note that the relative numbers of viral membrane proteins per VLP may be adjusted, at least to a certain degree, by changing the ratio of the viral membrane protein plasmid with respect to that of the HIV core plasmid.

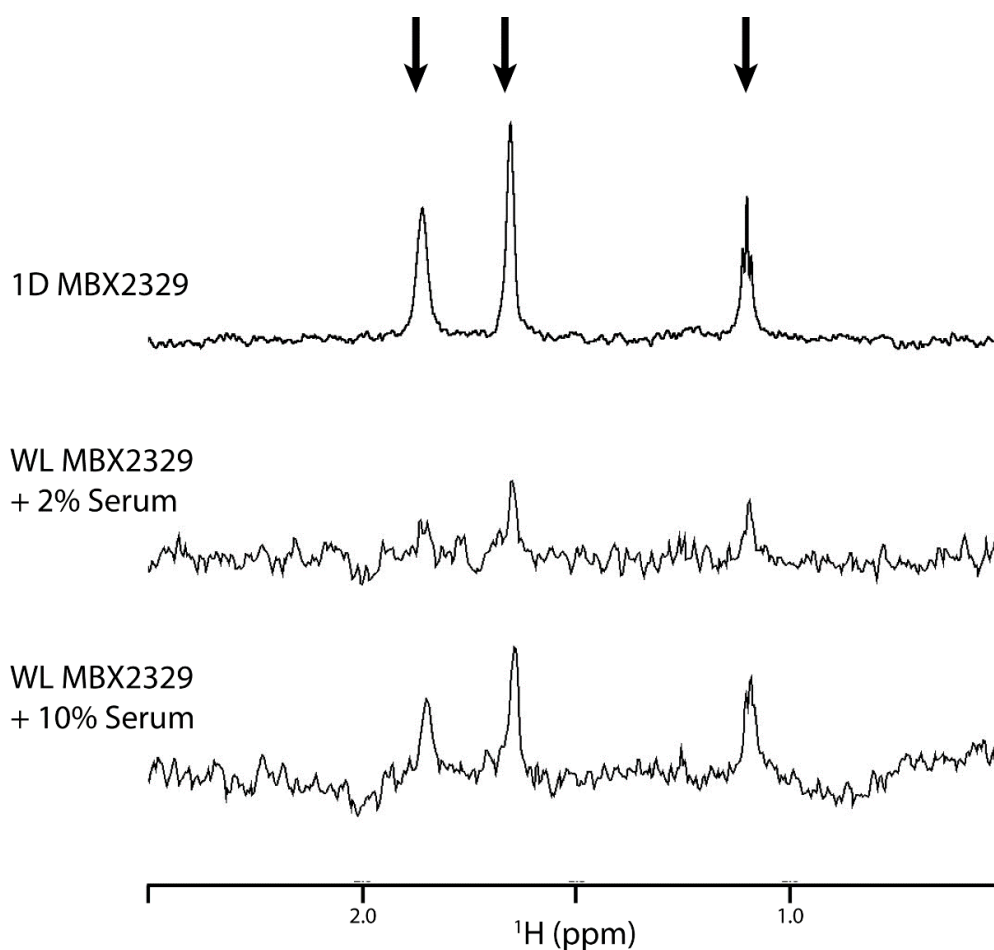


Figure 48. WL NMR detection of small molecule binding to serum proteins present in cell culture media. For reference the 1D NMR spectrum of the downfield region of MBX2329 is shown. Arrows denote ligand peaks used as reporters of ligand binding to serum proteins. Experimental conditions were 100 μM MBX2329 \pm 2 or 10 % Fetal Bovine Serum (FBS) in 50 mM phosphate/pH 8.2, 50 mM NaCl, 10 % $^2\text{H}_2\text{O}$ at 25°C. WL spectra were acquired for ~2 h on an 800 MHz spectrometer equipped with a room temperature probe.

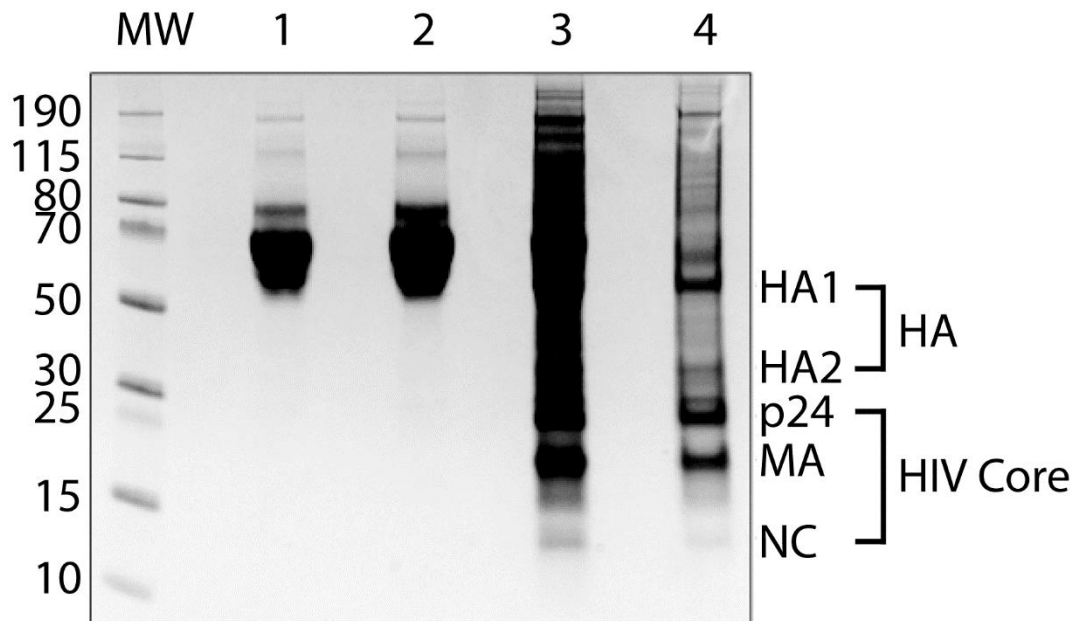


Figure 49. SDS PAGE stained by Coomassie Blue showing purification of HA-VLP. Lanes correspond to: MW molecular weight markers; 1 cell media, 2 VLP in supernatant, 3 VLP after sucrose gradient centrifugation, 4 VLP present after sucrose gradient centrifugation and gel filtration chromatography. For reference the positions of HA composed of HA1 and HA2 and the HIV core components composed of p24, MA and NC are shown to the right.

As noted above, based on studies of recombinant HA, the small molecule MBX2329 binds to HA and inhibits influenza entry by stabilizing the neutral pH conformation (Antanasijevic et al. 2014a; Basu et al. 2014). Consequently, we tested the potential to detect MBX2329 binding to HA embedded in the membrane using HA-VLP by WL NMR. For reference, the 1D NMR spectrum of the ligand is shown at the top of Figure 50. As shown in Figure 50., binding of MBX2329 to recombinant HA is evident from the positively phased peaks of ligand in the presence of 10 μ M recombinant protein. In a similar manner, binding of MBX2329 to HA-VLP is clearly detected (Figure 50.). Note that specificity of the binding to HA is established by performing a control experiment using NA-VLP, as opposed to HA-VLP, normalized to the same concentration of VLP (Figure 50., this control is critical in our case because our HA-VLP contain a small amount of NA, as noted above). In the case of the HA-VLP and NA-VLP experiments the concentrations of HA and NA were \sim 10 nM. As shown in Figure 50., the S/N is similar for identical experimental times using recombinant HA and VLP-bound HA, despite the 1000 fold decrease in HA concentration present in VLP, thereby demonstrating the potential high sensitivity of VLP-based NMR experiments.

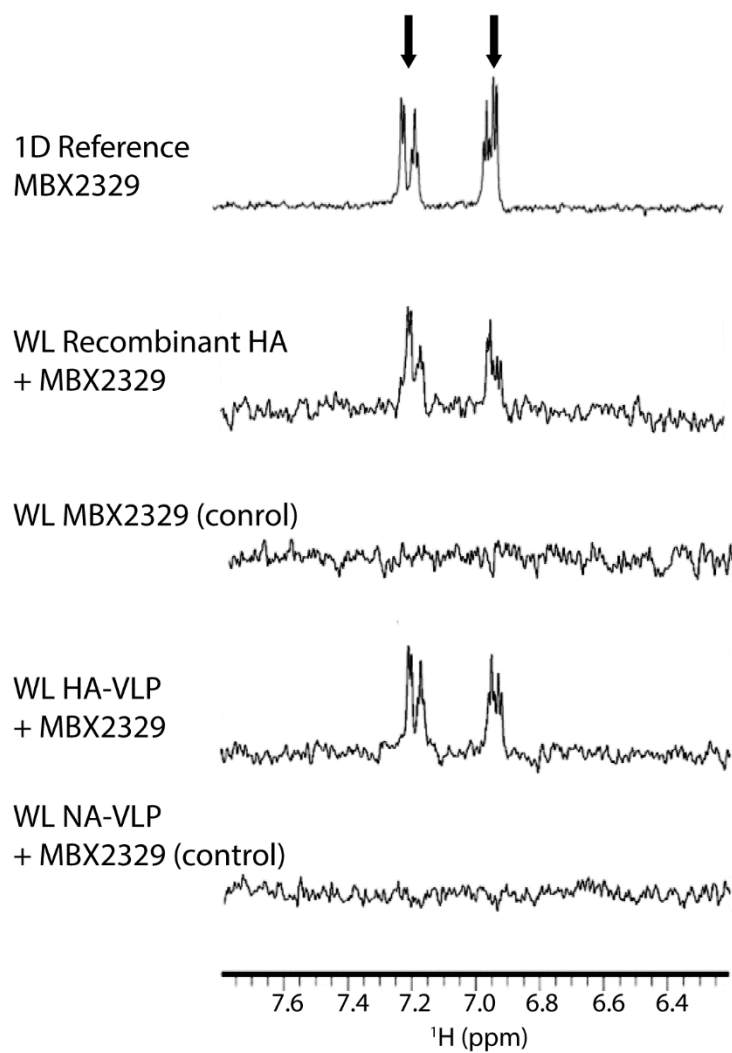


Figure 50. WL NMR spectra of the MBX2329 interaction with recombinant HA and HA embedded in VLP. For reference the 1D NMR spectrum of the downfield region of MBX2329 is shown. Experimental conditions were 100 μM MBX2329, ± 10 μM recombinant HA, ± 10 nM HA or NA in VLP in 50 mM phosphate/pH 8.2, 50 mM NaCl, 10 % $^2\text{H}_2\text{O}$ at 25 $^\circ\text{C}$ with WL spectra acquired for ~ 2 h on a 900 MHz spectrometer equipped with a cryogenic probe.

STD NMR is generally less sensitive than WL NMR (Antanasijevic et al. 2014b); however, STD NMR offers unique information that can be used to characterize the orientation of the ligand and guide chemical optimization (Mayer and Meyer 2001; Antanasijevic et al. 2013). Thus, we tested the potential to characterize MBX2329 binding to HA embedded in the membrane (i.e. HA-VLP) by STD NMR. As shown in Figure 51.A, binding of MBX2329 to HA-VLP is clearly detected by STD NMR and, importantly, no detectable binding is observed to NA-VLP (in both cases the VLP concentrations were normalized using p24). We next quantified the relative intensities of the ligand ^1H , which reflects the relative proximity of the ligand ^1H to the HA surface (Mayer and Meyer 2001; Bhunia et al. 2012; Antanasijevic et al. 2013; Basu et al. 2014). In Figure 51.B, we compare the relative orientation of MBX2329 to membrane bound HA with the relative orientation of MBX2329 to recombinant HA. Note that the recombinant HA experiments were performed at 30 μM and the HA-VLP experiments were performed at 30 nM. Strikingly, the relative proximities of the ligand ^1H are similar, which suggests that the mode of binding is similar between recombinant and membrane bound HA. For example aromatic region of the molecule is in closer contact to hydrophobic residues in the binding pocket and is more involved in binding than the azepane moiety. Accordingly, the linker and azepane groups may represent attractive regions for introducing chemical changes to improve the inhibitory or pharmacokinetic properties of this compound.

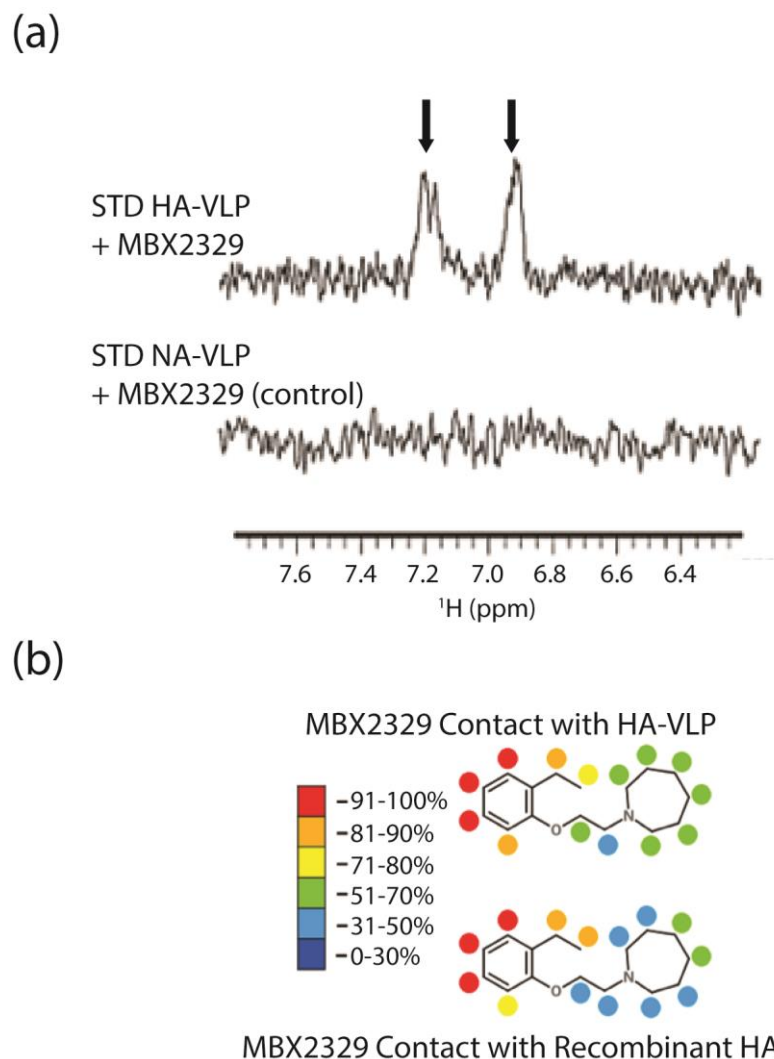


Figure 51. STD NMR characterization of the MBX2329 interaction with recombinant HA and HA embedded in VLP. (A) Downfield region of the STD spectra of MBX2329 interactions with HA-VLP and NA-VLP. The 1D NMR spectrum of MBX2329 is given on top for reference; (B) schematic diagram showing relative STD percentages for recombinant HA and membrane-bound HA. Experimental conditions were 100 μ M MBX2329, \pm 30 μ M recombinant HA, \pm 30 nM HA or NA in VLP in 50 mM phosphate/pH 8.2, 50 mM NaCl, 100 % 2 H $_2$ O at 25 $^{\circ}$ C with STD spectra acquired for 13 h on a 900 MHz spectrometer equipped with a cryogenic probe.

As mentioned above, we observe similar STD intensities for recombinant HA at 30 μM and VLP-bound HA at 30 nM. In the next step, we used the program CORCEMA (Jayalakshmi and Krishna, 2002) and our previously published model of the HA-MBX-2329 complex (Antanasijevic et al., 2014a) to calculate the relative STD signal as a function of correlation time and target protein concentration (Figure 52.). Based on the estimated correlation time of the recombinant HA trimer (~ 100 nsec), the relative STD signal is expected to be $\sim 90\%$ (Figure 52.). On the other hand, the estimated correlation time of VLP-bound HA is estimated to be ~ 1 msec and the relative STD signal is expected to be $\sim 70\%$. Thus, our observation of similar STD signal for HA under very different physical states is in relatively good agreement with the CORCEMA simulations. In summary, STD NMR studies performed with VLP based samples suggest that the mode of binding of MBX2329 to HA is similar in recombinant and membrane bound forms. Importantly, HA-VLP provide the same type and quality of information as the recombinant HA based experiments, using significantly less material.

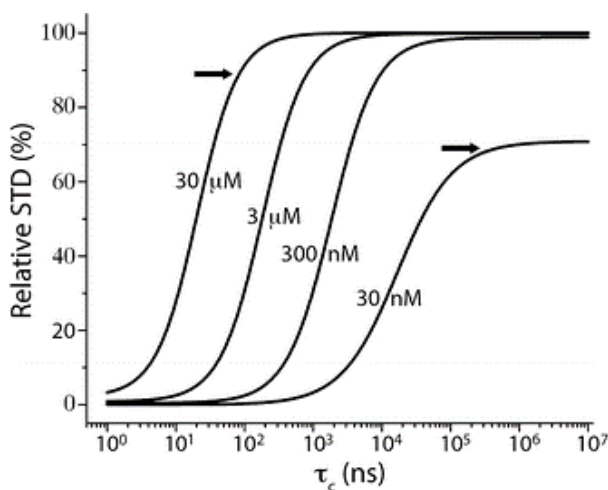


Figure 52. CORCEMA simulations of relative STD signal as a function of correlation time and target protein concentration for the HA-MBX2329 experiments. The expected correlation times of recombinant HA and VLP-bound HA are denoted by arrows, based on the estimated Stokes radii of the HA trimer and HA-VLP.

Current treatments for influenza include inhaled zanamivir (Relenza), oral oseltamivir (Tamiflu) and intravenous peramivir (Rapivab), which were developed as substrate analogs targeting viral NA (von Itzstein et al., 1993; Lagoja and De Clercq, 2008; Cairo, 2014). Previous studies have shown that NA-VLP purified using sucrose gradient centrifugation exhibit enzymatic activity (Mohan et al., 2010; Garcia et al., 2014). Accordingly, we tested whether our NA-VLP, purified with the additional gel filtration step discussed above (Figure 49.) were suitable for kinetic and biophysical studies. First we used 4-Methylumbelliferyl- α -D-N-acetylneuraminic acid (MUNANA), a fluorescent substrate analog of NA (Potier et al. 1979), to measure the activity of NA present in NA-VLP by NMR detection of product formation. As shown in Figure 53.A, product is uniquely formed in the presence of NA-VLP and the enzyme activity is reversed by the addition of the inhibitor DANA (Neu5Ac2en), a transition state analog and the parent compound of FDA-approved NA inhibitors (von Itzstein et al., 1993; Lagoja and De Clercq, 2008; Cairo, 2014). Importantly, control measurements using VLP prepared in the absence of NA expression (native-VLP), in which p24 levels were used to normalize the amount of VLP in the samples, exhibited no activity (Figure 53.A). As shown in Figure 53.B, the Michaelis–Menten plot of VLP-bound NA activity yields $K_m \sim 22 \mu\text{M}$, which is in good agreement with previous fluorescence-based kinetic studies (Rameix-Welti et al., 2006; Collins et al., 2008; Marathe et al., 2013) and support the functionality of the VLP-bound NA. In the next, step we prepared H274Y-NA-VLP, in which the NA possesses the H274Y mutation responsible for resistance to Tamiflu (Bloom et al., 2010; McKimm-Breschkin, 2013). As shown in Figure 53.C, the Michaelis-Menton plot of VLP-bound H274Y-NA activity yields $K_m \sim 36 \mu\text{M}$, which is in good agreement with previous fluorescence-based kinetic studies of the Tamiflu resistant mutant (Bloom et al., 2010; McKimm-Breschkin, 2013) and support the potential of NMR kinetic studies of NA mutations in NA-VLP.

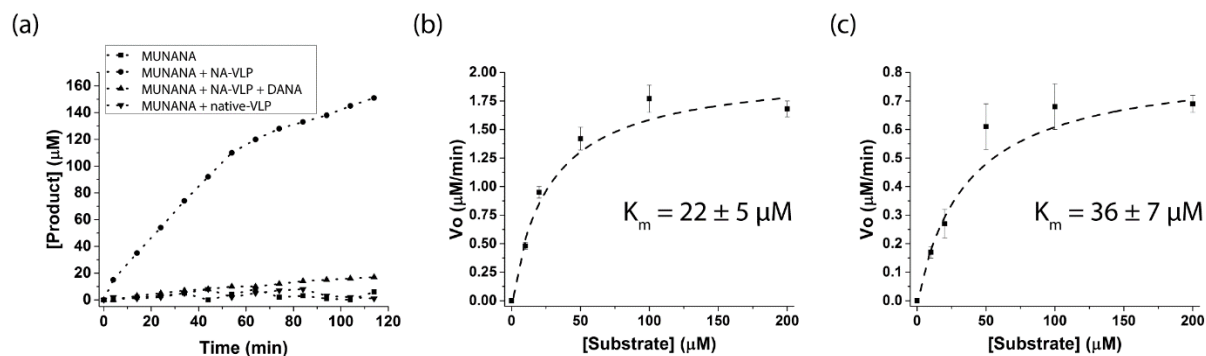


Figure 53. NMR characterization of NA kinetic activity in NA embedded in VLP. (A) Time course of product formation in the presence and absence of NA and DANA. (B) Michaelis–Menten plot of the NA-VLP catalyzed reaction. (C) Michaelis–Menten plot of the H274Y-NA-VLP catalyzed reaction. The product formation was detected by the MUNANA resonance at 2.50 ppm. Experimental conditions were ~ 10 – 20 nM NA in phosphate/pH 7.4, 150 mM NaCl, and 1 mM CaCl_2 at 25 °C with spectra acquired on a 900 MHz spectrometer equipped with a cryogenic probe.

In the next step, WL NMR was applied to detect the interaction between the inhibitor DANA and NA-VLP. In control measurements we used the same amount of VLP prepared in the absence of NA expression (native-VLP), with p24 levels used to normalize the amount of VLP in the samples. As shown in Figure 54.A, binding of DANA to NA-VLP is easily detected by WL NMR. Importantly, the DANA binding is NA-specific as shown by the absence of signal in the native-VLP. We then compared the amount of WL signal from the NA-VLP experiment in the absence and presence of 2.5 mM MUNANA, the substrate analog, using a WL NMR competition assay previously developed for recombinant proteins by our group (Antanasijevic et al., 2013; Basu et al., 2014). As shown by Figure 54.B, the presence of substrate in high excess causes a decrease in the DANA WL signal, which is consistent with the competitive inhibition model previously described for this family of compounds (Meindl et al., 1974).

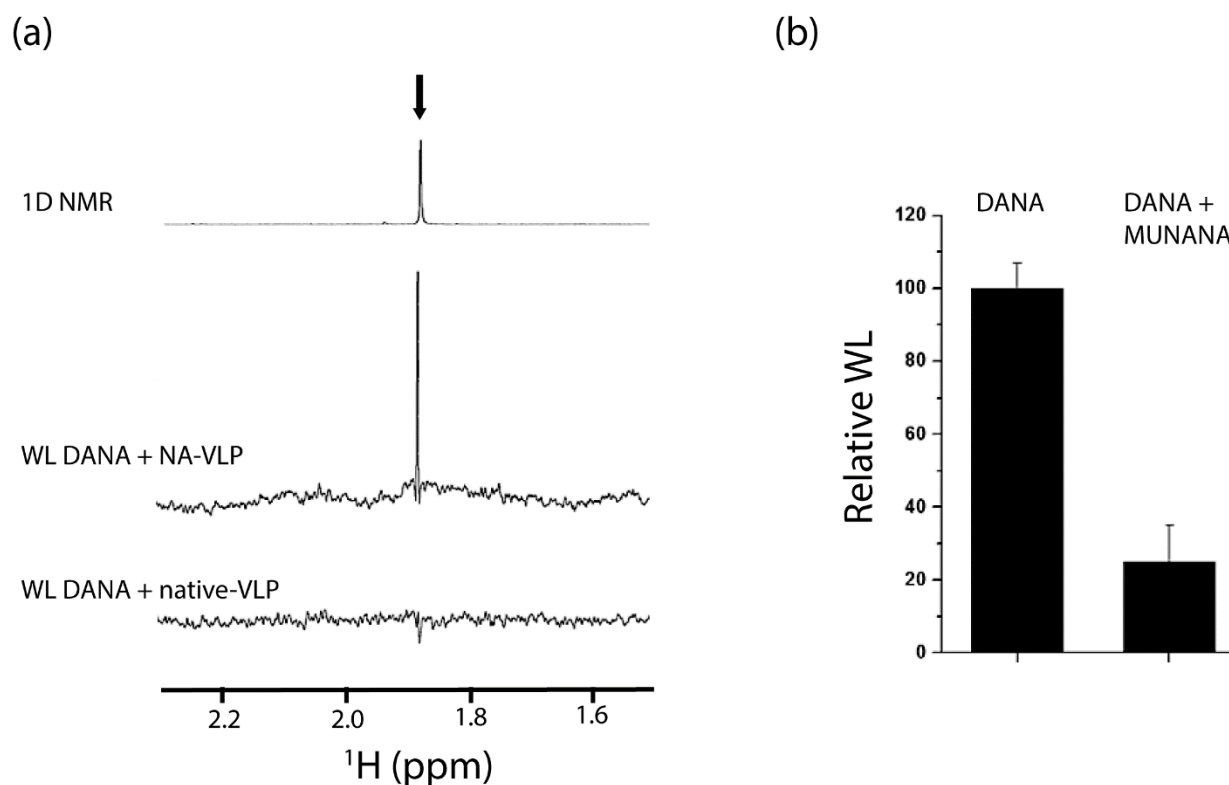


Figure 54. Characterization of inhibitor DANA binding to NA-VLP by NMR. (A) WL NMR spectra of DANA binding to NA-VLP (middle spectrum) and not to native VLP (bottom spectrum). For reference the 1D NMR spectrum of DANA is shown (top spectrum). (B) WL NMR competition assay to demonstrate competitive binding between inhibitor DANA and substrate analog MUNANA. Experimental conditions for the WL NMR were ± 80 nM NA in VLP, 200 μM DANA and ± 2.5 mM MUNANA in 20 mM PO_4/pH 7.4, and 150 mM NaCl, with WL spectra acquired for ~ 2 h on an 900 MHz spectrometer equipped with a cryogenic probe.

Chapter 4 - Conclusions

Chapter 4.1 - Characterization of the stem-loop region

(Adapted from Antanasijevic et al., 2014a; see Appendix A)

In this work we generated 18 site-directed mutations to 14 conserved sites in the H5 HA stem loop region. In the case of 13 mutations, they had very little effect on HA expression, processing, incorporation into virions, and binding to receptor. On the other hand, mutants HA1-D26K, HA1-M102L, HA2-V52A, and HA2-I55A exhibited reduced HA expression and mutants HA1-D26K, HA2-T49A, and HA2-M102L somewhat reduced hemagglutination. In contrast, many of the mutations significantly impaired HA-mediated viral entry. Interestingly, several of the substitutions disrupting entry were relatively conservative in nature (e.g. HA1-I28V, HA2-T41A, HA2-T49A, HA2-N53A, and HA2-D57E, Table II), which underscores the importance of this region to HA function and its sensitivity to structural perturbations for HA-mediated entry.

We also considered the mutational effects with respect to the H5 HA structure. In Figure 11. we show space filling diagrams of the effects on entry and C179 entry inhibition. In this representation, we have considered the outer face (i.e. solvent exposed) and inner face (i.e. contact region with other subunits) of a single HA monomer. The red, blue, and green coloring scheme corresponds to negative, minimal, and enhanced effects on HA-mediated entry, respectively. In the case of the mutational effects on virus entry, substitutions to HA2-Ile45 and HA2-Asn53 of the HA outer face and HA1-Ile28, HA1-Met31, and HA2-Leu99 of the HA inner face had the largest effects (red color, entry <10% of the wild-type). Note that during entry, the depicted inner residues are not in a region that undergoes a large conformational change and thus the mutational effects most likely arise from perturbation of the beginning neutral pH structure. In contrast, the depicted outer residues are in a region that undergoes a

large conformational change and thus mutational effects could arise from perturbation of the beginning structure (i.e. the neutral pH conformation) and/or later structures (i.e. the low pH conformations).

In the case of the mutational effects on entry inhibition by the monoclonal antibody C179, substitutions to HA2-Ile45 of the outer face and HA1-Met31 and HA2-Ile45 of the inner face decreased potency to ≤ 0.5 with respect to the wild-type (Figure 11., red color). In contrast, substitution of HA2-Leu99 enhanced potency of the antibody to >3 with respect to the wild-type (green color). With respect to the neutral and low pH conformations of HA, C179 binds to the neutral pH conformation shown in Figure 11. Consequently, the mutational effects of the residues depicted on the outer face are presumably due to direct interactions with the antibody and the mutational effects of the residues depicted on the inner face are presumably indirect and propagated effects.

In summary, the mutations presented herein underscore the importance of the stem loop region to HA function. Importantly, many of the sensitive sites of the HA stem loop region are highly conserved and solvent exposed and, moreover, they may represent novel target sites for therapeutic intervention of influenza entry. Such sites may be of particular importance in targeting new pandemic outbreaks of influenza including those of avian H5 and H7 HA.

Chapter 4.2 - Studies of the mechanism behind early and intermediate steps of the fusion process

Given that the great majority of influenza fusion inhibitors provide stabilization or destabilization of HA only if bound to neutral and intermediate pH conformations, it is of interest to explore some of the early steps of the fusion process. Most of the inhibitors are thought to function through the inhibition of early and intermediate, reversible structural rearrangements that lead to the irreversible triggering of fusion. Understanding these steps would help us get more insight into the regulation of the fusion process as well as the mechanism of action for different inhibitors.

Based on the limited proteolysis and thermal shift assays (Figure 12.) we concluded that multiple H5 HA intermediates exist between pH 7.5 and 5.5, with very low probability for the full HA extension and subsequent onset of fusion. We then used x-ray crystallography to learn more about these states and the H5 HA crystal structure was determined for several different conditions.

First, we compared a structure from a condition at pH 8.5 and a structure at pH 6.5. One major difference was observed (Figure 13.). The fusion peptide, that is usually hidden inside the trimer interface (due to its hydrophobicity) is displaced and facing towards the outside of the molecule. The first 4 residues of the FP were not present in the density suggesting more dynamic behavior in this conformation. This data is in excellent agreement with the H/D exchange studies done on H3 HA (Garcia et al., 2015), where it was found that the fusion peptide is the most dynamic part of the protein at intermediate pH. However, we note that the two structures (pH 8.5 and pH 6.5) were determined using two very different crystallization conditions (100 mM Tris, pH 8.5 + 20 % PEG 6000 + 10 % Glycerol for pH 8.5 structure and 100 mM Cacodylate buffer, pH 6.5 + 200 mM NaCl + 2 M (NH₄)₂SO₄ + 10 % Glycerol for pH 6.5 structure) and consequently, at this moment we do not know the contributions of the crystallization buffers and crystal packing to the change in conformation we are observing.

In order to study small scale changes induced by pH we used the previously mentioned pH 6.5 crystals grown in cacodylate buffer. The crystals from the same drop were taken and soaked for 15 mins in a selected cryo solution composed of identical components in all cases but with different final pH (7.0, 6.5, 6.0 and 5.5). We find this approach to be ideal for identification of local structural rearrangements caused by protonation at low pH. Of particular interest were the histidine residues and the amino acids surrounding them. Structure comparison revealed multiple His sites affected by the pH. In the case of HA1-H18 (Figure 14.), lowering the pH below 6.5 induces a side-chain flip. The flip is caused by the protonation of this residue and residue HA1-H38 in its close proximity. It should be noted that the two

histidines are highly conserved across Group 1 HA and that their involvement in the onset of fusion has been already discussed elsewhere (Stevens et al., 2004). To our knowledge this represents the first successful effort to characterize pH induced structural changes by crystal soaking at different pH.

Interestingly, structural rearrangements in this region were first observed in the structure of H1 HA from the pandemic 1918 influenza virus (Stevens et al., 2004), very closely related in sequence to H5 HA used in our research. Full length, non-cleaved precursor protein was crystallized under the low pH conditions (pH 5.5) even though the main goal of the study was not to explore low-pH-induced structural changes. The authors found that the tri-histidine region was significantly different compared to other group 1 HA structures, and they suggested this to be a consequence of the crystallization pH (given the high sequence conservation in the region). The overlay of our H5 HA structures at pH 7.0 and pH 5.5 and the H1 HA determined by Stevens et al., 2004 is shown in Figure 55. It is very likely, that the H1 HA conformation determined in their work is one of the intermediate states of the fusion process leading to HA1 – HA2 dissociation and fusion peptide triggering. Significant loop rearrangements follow the translocation of HA2-D19 into the proximity of HA1-H38 and the salt bridge formation between the two. In the case of H5 HA structure crystal packing constraints prevent any such large-scale rearrangements.

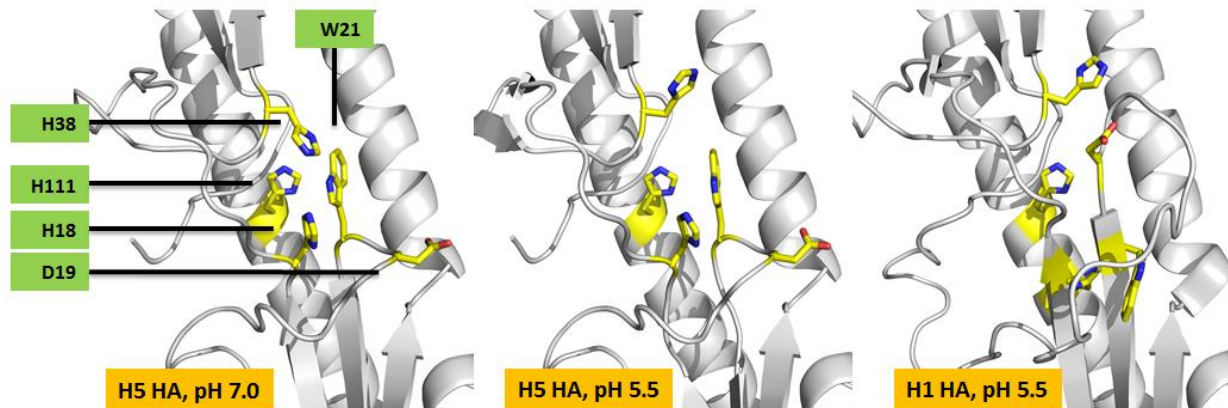


Figure 55. Comparison of H5 HA structure at pH 7.0 and pH 5.5 and H1 HA structure at pH 5.5. H1 HA was crystallized under low pH conditions (Stevens et al., 2004) and the significant structural rearrangement were observed in the triple-histidine region, most likely a consequence of the protonation of H18, H38 and H111. The structure is shown on the right with these residues highlighted. Our H5 HA structures determined after soaks in pH 7.0 and pH 5.5 cryo-solutions are shown on the left and center, respectively.

On the other hand, we also discovered several histidine (HA1-H113, HA1- H120, HA1 – H189 and HA2 – H142) residues that induce local changes in anchoring of highly dynamic, charged amino acids around them (Figure 56.). Stronger or weaker anchoring under certain conditions is reflected by higher or lower occupancy in a conformation proximal to the histidine. In Figure 15. we show how HA1-H113 protonation at low pH causes a significant increase in the electron density and localization of HA2-E69. The interaction between these two residues has already been connected to the fusion process elsewhere (Herfst et al., 2012; Zhang et al., 2013).

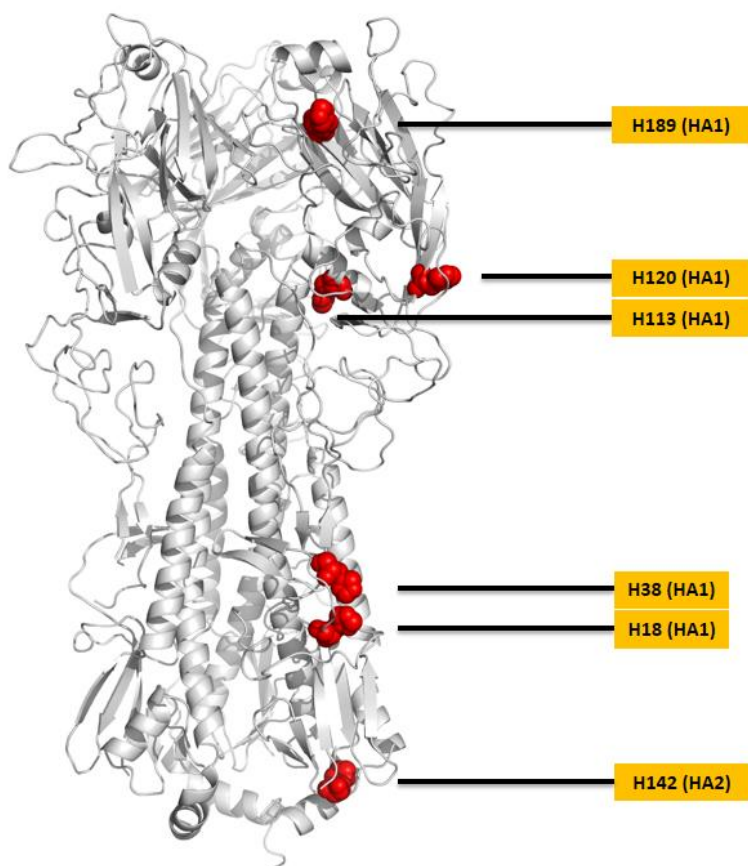


Figure 56. Positions of the His residues presumably undergoing protonation at low pH. For simplicity, residues in only one monomer are indicated. Chains (HA1 or HA2) are indicated in parentheses.

We plan on applying mutagenesis in combination with viral entry assays and fusion assays to verify the importance of the discussed amino acids (and the interaction network they create) for the normal functioning of HA (work in progress). However, it is very encouraging that the two sites discovered using the pH soak methodology have already been identified by others as the important regulatory domains for the fusion process. We believe that this application of x-ray crystallography is something to be further explored for studying pH-responses of all types of HA which might reveal the similarities and differences in the mechanism of fusion regulation. Additionally, this methodology can provide very valuable insights into the mode of action of different fusion inhibitors (as seen in the example of RLC), as well as explain the group and type specificity of some inhibitors.

Chapter 4.3 - Characterization of Group 1 inhibitors: MBX2329 and MBX2546

(Adapted from Basu et al., 2014; Antanasijevic et al., 2014a; see Appendix A)

To identify potential influenza virus entry inhibitors, a high-throughput screening (HTS) assay was used to screen a chemical compound library composed of over 100,000 unique small molecules (work performed by Microbiotix Inc.). Two novel compounds, MBX2329 and MBX2546, were selected based on their potency, and their mechanism of action was characterized.

We first verified the activity of these compounds against H5 N1 pseudovirus (Figure 16.). The compounds showed very strong, low micromolar activity against the entry of H5 N1. In the subsequent steps we applied WaterLOGSY and STD NMR to confirm the H5 HA as the target of MBX2329 and MBX2546 and to determine the mode of binding for these two compounds (Figure 17. and Figure 19.). Surface plasmon resonance (SPR) measurements confirmed the interaction between H5 HA and the two inhibitors (Figure 18.). Importantly, the K_d values determined via SPR (Figure 18.) were in excellent agreement with the IC50 values from the pseudovirus entry assays.

In the next step, we wanted to determine the binding site of MBX2329 and MBX2546 on the surface of H5 HA. WaterLOGSY competition experiments with C179 monoclonal antibody placed the compound binding site in the stem-loop region. Interestingly, competition studies showed that MBX2329 and MBX2546 do not compete with each other (Figure 19.A) and appear to simultaneously bind to different regions of HA. These results were further supported by NOESY experiments, where the absence of signal in the NOESY experiment suggested that the binding sites for MBX2329 and MBX2546 on HA are $>6 \text{ \AA}$ apart (Figure 19. B). It should be noted that while the absence of signals in the NOESY experiment does not prove that the compounds bind to distant sites, it is nevertheless consistent with this notion.

Mutagenesis studies were performed to help narrow down the binding sites for the two compounds. The final results (Table IV, Figure 20.) show a lot of overlap in the effects of different mutations on the activity of the two compounds. Several mutants (HA2-L99A, HA2-V52A and HA2-N53A, HA1-M31A, HA1-I28A, HA2-M102A) caused a similar change in activity for both compounds, suggesting that these mutations might be inducing more serious, long-range perturbations in the stem-loop region.

The studies of stability, processing and viral fitness performed on the same set of mutants in the first part of the work seem to agree with this idea (Figures 8 – 11. and Table II). These findings are not surprising given how highly conserved the stem-loop region is. On the other hand, there were several mutations that altered inhibitory activity of only one or the other compound, but not both (HA2-S54R and HA2-I45A for MBX2329 and HA2-M102L for MBX2546. The locations of these mutants are in excellent agreement with the compound locations in molecular docking simulations performed without any prior knowledge of the mutagenesis data. Somewhat surprisingly, the binding site of MBX2546 seems to be in the middle of the trimer, a location that is not considered to be druggable.

In one of the X-ray crystallography datasets obtained for the crystals of H5 HA with MBX2546 we do see a strong electron density in the exact same location as predicted by MD and mutagenesis studies (Figure 22.). However, the electron density is not sufficient to accommodate the entire molecule. Additionally, the density is deprived of any structural features that can unambiguously connect it to MBX2546. This is somewhat expected given the unique nature of this binding site (three-fold symmetry). The NOESY NMR structure of MBX2546 in the bound state suggests a similar conformation to the MD and crystal structure with the two aromatic rings π -stacked (Figure 23.). We believe this to be the correct binding site and binding conformation for MBX2546. However, more structural evidence needs to be obtained in order to remove any doubt. In the next steps we will attempt to increase the solubility of MBX2546 in the crystallization conditions used and/or generate more soluble analogs of this compound.

Finally, we have applied limited proteolysis experiments and thermal shift assays to tell us more about the mechanism of action of MBX2329 and MBX2546 (Figures 24. and 25.). Based on these experiments, we conclude that the two molecules act by binding to the neutral pH conformation of H5 HA and prevent low-pH induced conformational change.

Chapter 4.4 - Group 1 inhibitors: Determining the binding site and mode of action of RLC

RLC was discovered in the lab of Dr. Lijun Rong. It was demonstrated that this compound can inhibit the entry of group 1 viruses with nanomolar potency. IC50 values against H5 HA and H1 HA in the infectious virus assay were 200 nM and 50 nM respectively. However this compound does not show any inhibition against HA from Group 2.

We have used the crystal soaking approach to determine the structure of RLC in complex with H5 HA. Based on the available published reports, this is the first structure of an avian HA in complex with a small molecule inhibitor and only the second such structure for all HA subtypes discovered to date.

The compound appears to be binding in the stem-loop region, on the HA1 – HA2 interface of each monomer (Figure 26.). The amino acid residues interacting directly with the compound are G16 – A19 and T37-D41 on HA1 side and D19 – Y22 and T41 – V52 on the HA2. The binding site is in immediate proximity of the triple-histidine region described in the previous sections as part of studies on pH-dependent local structural changes. In the low-pH experiments we find that HA1-H38 undergoes a side-chain flip at pH < 6.5 (Figure 14.), presumably as a consequence of protonation. The protonation of these His residues is suggested to lead to the dissociation of HA1 and HA2 subunits and the later onset of fusion (Stevens et al., 2004). Based on these findings we hypothesized that RLC functions by inhibiting these early steps of the fusion process and preventing structural rearrangements in the triple-histidine region. WaterLOGSY binding experiments performed under different conditions strongly supports this idea (Figure 29.).

The alignment of sequences and structures of the most prevalent HAs from group 1 and group 2 reveal the reasons behind the group specificity of RLC (Figure 28.A and B). The substitution of HA1-H38 for Asn38 in group 2 introduces a glycosylation site that would completely destroy any binding of the compound in the area. Besides explaining some of the aspects of RLC activity, this finding is very interesting for two other reasons: (1) First, it provides the potential mechanism for the development of resistance against this compound in group 1 HA; (2) More interestingly, given the results of the low pH studies and the high conservation of these His residues in group 1 HA but NOT in group 2 HA, the data here raises a question of whether the fusion is regulated the same way in all HA types. It is a very intriguing idea that might help explain some of the many discrepancies observed between HA subtypes, including the mechanisms behind the group specificity of fusion inhibitors.

Furthermore, the comparison between H1 HA and H5 HA used in the activity assays provides the explanation for a slight preference towards H1 HA (vs H5 HA) observed in the entry inhibition

experiments (Figure 28.C). We are currently in the process of applying mutagenesis to confirm these findings.

Finally, the STD data are in excellent agreement with the crystal structure and suggests that the aromatic portion of the molecule is generating better contacts with the hydrophobic amino acids on the H5 HA surface while the piperidine ring and the isopropyl group seem to be less involved in binding. In the next steps we will try to chemically optimize RLC to further improve its potency in Group 1 HA.

Chapter 4.5 - Characterization and optimization of Group 2 inhibitors: TBHQ derivatives

(Adapted from Antanasijevic et al., 2013; see Appendix A)

Our work shows for the first time that TBHQ inhibits H7 HA-mediated entry in a similar manner to that of the previously characterized H3 HA (Figure 30.). WL competition experiments suggest that this inhibitor binds to the stem loop of H7 HA (Figure 31.) Moreover, fusion assays performed using limited proteolysis and bis-ANS fluorescence as the means for detection show that TBHQ acts by stabilizing the neutral pH conformation (Figure 32.), thereby delaying conformational changes necessary for fusion of the virus and endosome membranes. Taken together, we suggest that TBHQ is an attractive lead compound for the development of antivirals directed at H7 HA. Notably, the sequence identity between the H7 HA strain used in the present studies and that responsible for the new H7N9 outbreak in China is >96% with 100% sequence identity in the stem loop region. Nonetheless, TBHQ exhibits relatively modest potency and thus it is not suitable as therapeutic agent without further development. However, we note that our STD NMR experiments suggested sites for modification of TBHQ. Moreover, the crystal structure of H3 HA in complex with TBHQ (Russell et al., 2008) is another valuable resource for the chemical optimization of this compound.

In collaboration with the lab of Dr. Duncan Wardrop we have designed and tested >40 different derivatives of TBHQ (Table V). The compounds were all assayed for their activity against the entry of H7 HA, H5 HA and VSVG pseudoviruses. We have also used 1D NMR experiments to monitor the stability of the derivatives, as the starting compounds from this series had some unfavorable redox properties (Figures 34., 39. and 40.). Cytotoxicity effect was measured for the most interesting compounds (Figure 36.). Our work represents the first demonstration that a PAIN can become PAINless.

Importantly, for the chemical optimization we have chosen 3 different sites (Figure 57.). 1-OH and 4-OH groups were chosen for substitution as they are the cause behind the reactivity of TBHQ. On the other hand, the tert-butyl group was suggested to be a good location for optimization of the compound hydrophobic interactions and its affinity for HA.

The optimization trials were successful for positions 1 and 2 and yielded 2 combinations of substituent groups that increased the activity of the resulting compounds by 60-fold while at the same time decreased their reactivity and cytotoxicity (compared to the original parent compound). In order to completely remove the reactivity of the hydroquinone head we have tested a large number of substituents at position 4 (Table V). However, all compounds tested were less potent than the parent, suggesting that 4-OH group might be essential for the activity of the compounds from this series. The crystal structure of H3 HA in complex with TBHQ supports these findings (Figure 35.).

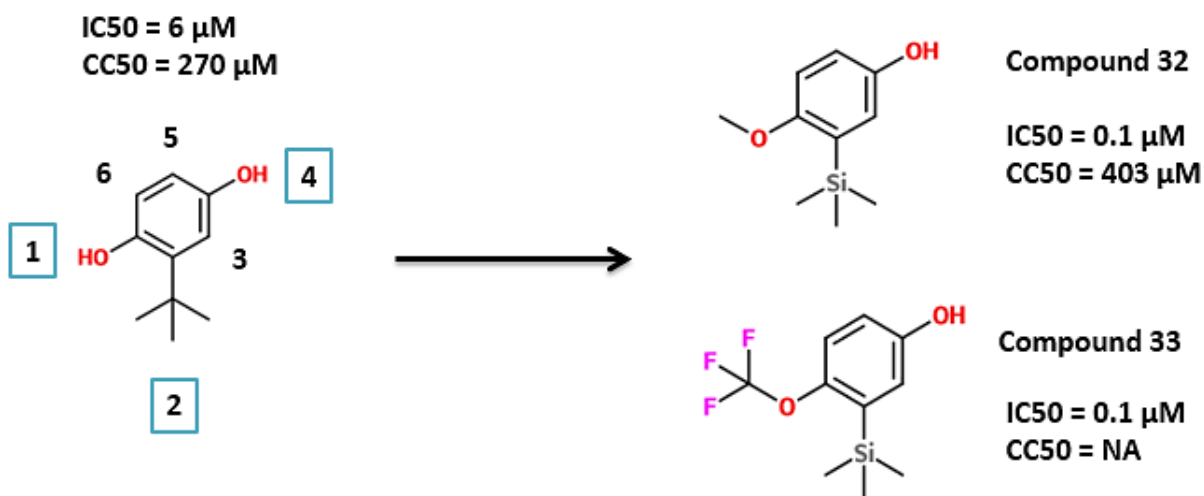


Figure 57. Chemical optimization of the TBHQ. Starting molecule (TBHQ) is shown on the left with the corresponding IC_{50} and CC_{50} values. The sites of substitutions are indicated. Two best molecules are shown on the right. The CC_{50} value was not determined for Compound 33.

Several selected compounds (**4**, **6**, **11**, **24**, **32** and **33**) were subjected to experiments with infectious virus (H3 N2). The IC_{50} values determined in these experiments were very comparable to the corresponding IC_{50} values from the pseudovirus assays performed in our lab. This work represents the first demonstration of the STD guided (assisted) chemical optimization of an inhibitor.

In the next steps we will try to optimize the functional groups at positions 3, 5 and 6 (TBHQ numbering), as well test the anti-influenza activity of some of the compounds *in vivo*.

Chapter 4.6 - NMR methods development

(Adapted from Antanasijevic et al., 2014b; Antanasijevic et al., 2016; see Appendix A)

In the first part of the methods development work we have compared the sensitivities between WaterLOGSY and STD NMR experiments in 3 different protein - small molecule ligand systems. We find that WL is generally more sensitive and importantly requires less attention to saturation power and the determination of the optimal “on” resonance saturation frequency, which is particularly important for NMR-based drug screens. Nonetheless, the STD experiment gives unique insight into the proximity of ligand ^1H to the biomolecule surface and thus STD will continue to be an important component of the spectroscopist’s toolkit. We describe several ways one can use to increase the sensitivity of the STD experiment if the low sensitivity is an issue. Finally, we note that STD has been applied to membrane-bound systems at relatively low concentrations and thus WL experiments on such systems are expected to be >10X more sensitive, thereby allowing increased numbers of membrane systems to be characterized by NMR.

In conclusion, we reiterate that sensitivity in the NMR characterizations of biomolecule interactions with ligands is extremely important. For example, higher sensitivity reduces experimental times, which enables study of unstable systems, increases throughput and spectrometer efficiency, decreases the need for ultrahigh field spectrometer time, and enables kinetic studies. Moreover, the WL and STD experiments are optimal for excess ligands in relatively fast exchange and thus the sensitivity of the experiment is proportional to the biomolecule concentration. This becomes limiting when there are small amounts of biomolecule available due to difficulties in obtaining mg quantities, low natural concentrations, and/or complex systems that are difficult to isolate (e.g. membrane proteins present in a viral or cellular membrane). In addition, increased sensitivity allows characterizations of ligands at

lower concentrations nearer the K_d , which is important when there is the potential for additional lower affinity binding sites.

In the second part of methods development work we demonstrated the high potential of using VLP-based systems to study viral membrane proteins by NMR methods. As the model system we chose VLP prepared with the influenza proteins HA or NA on the surface, potential targets for novel antivirals, and the HIV core. The HIV core used (pNL4-3.Luc.R-E-) allows the expression of VLP with different combinations of viral membrane proteins, as well as VLP containing the native proteins of the host cell (Jacobs et al., 2005; Yermolina et al., 2011; Antanasijevic et al., 2013, 2014a). Importantly, the native-VLP offer the potential to serve as powerful control samples to demonstrate the specificity of small molecule interactions with membrane bound targets. To our knowledge, previous biochemical and biophysical studies of VLP did not utilize native-VLP as controls (Haselhorst et al., 2008; Mohan et al., 2010; Garcia et al., 2014). For our study of HA embedded in VLP, we characterized the HA interaction with MBX2329, a small molecule antiviral that binds to the HA stem loop region and prevents a critical change in conformation (Antanasijevic et al., 2014a, b; Basu et al., 2014). However, non-specific binding of a ligand to a target biomolecule, which may be due to the promiscuity of the ligand and/or target, is a significant concern for ligand based NMR techniques.

Consequently, we first tested the importance of VLP purity for the reduction of non-specific interactions by testing binding of MBX2329 to proteins present in FBS, a routine additive to cell cultures and potential contaminant due to its high protein concentration. For example, 10 % FBS contains ~4 mg/ml total protein and a purification scheme in which 90 % of the serum proteins would be removed would still contain 400 $\mu\text{g/ml}$ compared to target proteins in VLP at concentrations ~ 1 $\mu\text{g/ml}$. As shown in Figure 48., non-specific interactions between MBX2329 and proteins present FBS were indeed observed. Therefore, we made an effort to further purify our VLP preparations from serum proteins, as

well as cellular components. Historically, sucrose gradient centrifugation was the primary method to concentrate and purify viruses and VLP used in biochemical and biophysical studies (Haselhorst et al. 2008; Mohan et al. 2010; Garcia et al. 2014). In the present work, we showed that this treatment alone is not enough to achieve an acceptable level of purity required for NMR studies (Figure 49.). Indeed, after the sucrose gradient centrifugation step, viral proteins accounted for only ~15 % of the total protein present. However, the combination of sucrose gradient centrifugation and gel filtration helped remove the majority of serum (as well as cellular) proteins from the samples, with the viral proteins accounting for more than 60 % of the total protein content in the purified VLP preparations. The quality may be further improved with the application of additional steps (e.g. ion exchange or affinity chromatography); however, additional steps are expected to result in losses in VLP amount and activity. Moreover, many of the remaining proteins present in the VLP are expected to be due to those of the native membranes from which the VLP form and thus they will always remain. Importantly, the activity of the remaining native proteins may be accounted for by preparing native-VLP, or alternatively with VLP containing another membrane protein, as discussed below. After demonstrating the utility of the additional purification step, we characterized the interaction of MBX2329 with HA embedded in VLP, which corresponds to full length HA containing the native C-terminal transmembrane and intracellular domains, by WL NMR. Interestingly, the significantly greater size of the VLP particle (~200 MDa) compared to recombinant HA (~210 kDa) resulted in a much higher sensitivity in the experiments performed with VLPs. For example, ~10 nM HA embedded in VLP was necessary to obtain WL NMR spectra with optimal S/N ratio in a 2 h experiment. In order to collect data of comparable quality (i.e. S/N) with recombinant HA as the target, 10 μ M concentration was necessary. Consequently, by switching from a recombinant viral membrane protein without its transmembrane domain to HA embedded in VLP, ~1000 times more sensitivity was observed, supporting the high sensitivity of WL NMR for very large biomolecular systems (Antanasijevic et al. 2014b). Furthermore, as noted above, the

control versions of VLP are readily generated. For example, MBX2329 exhibits non-detectable interaction with NA-VLP (Figures 49. and 50.), which strongly supports the specificity of this compound for HA in the context of a membrane environment.

In the next step, we compared the binding mode of MBX2329 with recombinant HA and HA embedded in VLP by STD NMR (Figure 51.). As noted above, STD NMR gives insight into the relative contact of the ligand ^1H with the target surface and thus may be exploited to guide chemical optimization. In agreement with our previous work (Antanasijevic et al. 2014b), we observed that STD NMR is significantly less sensitive than WL NMR (the WL and STD spectra were acquired in 2 and 13 h, respectively). Nonetheless, similarly to the WL studies we achieved an increase in sensitivity by a factor of ~ 1000 when performing the experiments with HA-VLP with respect to recombinant HA, which we show is in good agreement with CORCEMA simulations (Figure 51.). Strikingly, the recombinant HA and HA-VLP datasets gave almost identical STD signatures (Figure 51.), suggesting very similar binding modes. In both cases, the relatively low STD signals of the ^1H in the linker region and the azepane group suggest that they are attractive sites for chemical optimization of this compound. Finally, the absence of measurable STD signal in the control measurement (NA-VLP) once again confirms the specificity of MBX2329 towards HA. Importantly, to our knowledge this work represents the first comparison of the binding mode of a small molecule inhibitor to recombinant and membrane-bound versions of a membrane protein.

We next demonstrated the utility of VLP applied to NA, a high priority target for influenza antivirals (von Itzstein et al. 1993; Lagoja and De Clercq 2008; Cairo 2014). In a first step we showed that NA embedded in VLP exhibits specific enzyme activity and that this activity is inhibited by DANA (Figure 53.), a parent compound of current influenza antivirals (von Itzstein et al. 1993; Lagoja and De Clercq 2008; Cairo 2014). Subsequently, a full analysis of NA activity and inhibition was performed by NMR

(Figure 53.). In addition, we demonstrated the ability to characterize the H274Y mutant of NA, which is commonly occurring mutation responsible for resistance to Tamiflu (Bloom et al. 2010; McKimm-Breschkin 2013). Notably, the H274Y-NA in VLP exhibited K_m increased by ~ 2 , which is in good agreement with previous studies of recombinant and influenza virus H274Y-N1 NA for which K_m of the mutant ranged from 2 to 4X higher than wild-type (Collins et al. 2008). Note that, with respect to recombinant membrane proteins, mutations are more readily generated in VLP (Caffrey 2011; Yermolina et al. 2011; Antanasijevic et al. 2014a). For example, the production of a mutant recombinant protein in a mammalian or insect expression system requires weeks of effort as opposed to VLP, which are routinely produced in a few days. Importantly, this work represents the first use of VLP to study a drug resistant mutant of NA.

Finally, to further demonstrate the utility of VLP for biophysical studies we characterized the interaction of the inhibitor DANA with NA-VLP by WL NMR. As shown in Figure 54., we observed binding of DANA to NA-VLP but not native-VLP, further underscoring the importance of native VLP controls. In addition we performed a competition WL NMR assay to demonstrate that DANA is a competitive inhibitor of the NA substrate, as previously observed by structural and kinetic studies. Thus, we clearly show that VLP can be used in combination with NMR to detect the binding of different inhibitors, as well as their binding sites and type of inhibition.

In summary, our work suggests that VLP have high potential to become standard tools in biochemical and biophysical studies of viral membrane proteins, particularly when they are highly purified and combined with control VLP containing native membranes. Importantly, the VLP constructs contain the entire protein sequence and are comprised of native membrane components including lipids, cholesterol, carbohydrates and cellular proteins. To date biochemical and biophysical studies have been limited to the viral membrane proteins from influenza (Haselhorst et al. 2008; Mohan et al. 2010;

Garcia et al. 2014, work reported herein); however, the VLP containing many other viral membrane proteins, including Ebola, HIV, and SARS-CoV are readily generated for virology studies (Jacobs et al. 2005; Kuhn et al. 2007; Yermolina et al. 2011) and thus we are confident that these systems will also be amenable for study by biochemical and biophysical methods to discover, characterize, and optimize ligand interactions.

APENDICES

Appendix A

In the thesis I have used the material (text and figures) from previously published research (authored by our lab). Literature source (if present) is indicated at the beginning of each chapter. Publications used:

- Antanasijevic A, Cheng H, Wardrop DJ, Rong L, Caffrey M. Inhibition of Influenza H7 Hemagglutinin-Mediated Entry, PLoS One. 2013, 8(10):e76363.
- Basu A, Antanasijevic A, Wang M, Li B, Mills DM, Ames JA, Nash PJ, Williams JD, Peet NP, Moir DT, Prichard MN, Keith KA, Barnard DL, Caffrey M, Rong L, Bowlin TL. New small molecule entry inhibitors targeting hemagglutinin-mediated influenza A virus fusion, J Virol. 2014, 88(3):1447-60.
- Antanasijevic A, Ramirez B, Caffrey M. Comparison of the sensitivities of WATERLOGSY and STD NMR experiments, J Biomol NMR. 2014, 60(1):37-44.
- Antanasijevic A, Basu A, Bowlin TL, Mishra RK, Rong L, Caffrey M. Mutagenesis studies of the H5 Influenza stem loop region, J Biol Chem. 2014, 289(32):22237-45.
- Antanasijevic A, Kingsley C, Basu A, Bowlin TL, Rong L, Caffrey M, Application of Virus-Like Particles (VLP) to Characterize the Interactions Between Inhibitors and Viral Membrane Proteins. J Biomol NMR, Vol 64(3):255-65, 2016;

All work is properly cited in accordance to the copyright terms prescribed by the corresponding journal. For details about the copyright permissions for individual journals visit the following links:

- PLOS One

<http://journals.plos.org/plosone/s/content-license>

- The Journal of Biological Chemistry

http://www.jbc.org/site/misc/Copyright_Permission.xhtml

- Journal of Biomolecular NMR

<https://www.springer.com/gp/rights-permissions>

- Journal of Virology

http://journals.asm.org/site/misc/ASM_Author_Statement.xhtml

H1 KVKSQKLNNAKEIGNGCFEFYHKCDNECMESVRNGTYDYPKYSEESKLNREKVDGVKLES 523
H3 KTKKQLRENAEDMGNGCFKIYHKCDNACIGSIRNGTYDHDVYRDEALNNRFQIKGVELKS 525
H7 RVKRQLRENAEEDGTGCFEIFHKCDDDCMASIRNNTYDHSKYREEAIQNRIQIDPVKLSS 528
.: : **::**:: *.****:::*****: *: **:* ***: * :*: :* :.: *:*.*

H5 IGIYQILSIYSTVASSLALAIMVAGLSLWMCSNGSLQCR--- 565
H1 MGIYQILAIYSTVASSLVLLVSLGAISFWMCSNGSLQCRICI 565
H3 -GYKDWILWISFAISCFLLCVALLGFIMWACQKGNIRCNICI 566
H7 -GYKDVILWFSFGASC FILLAIAMGLVFICVKNGNMRCTICI 569
* : : * *.: * .: : .:*.:*

Appendix C

Three sets of SPR measurements were done for measuring the binding of MBX2329 and MBX2546 to H5 HA (immobilized on CM5 chip). SPR sensograms for the experiments are shown on the left in the Figure 58. Corresponding steady-state dose dependency curves are shown on the right. For clarity, different concentration points are color coded.

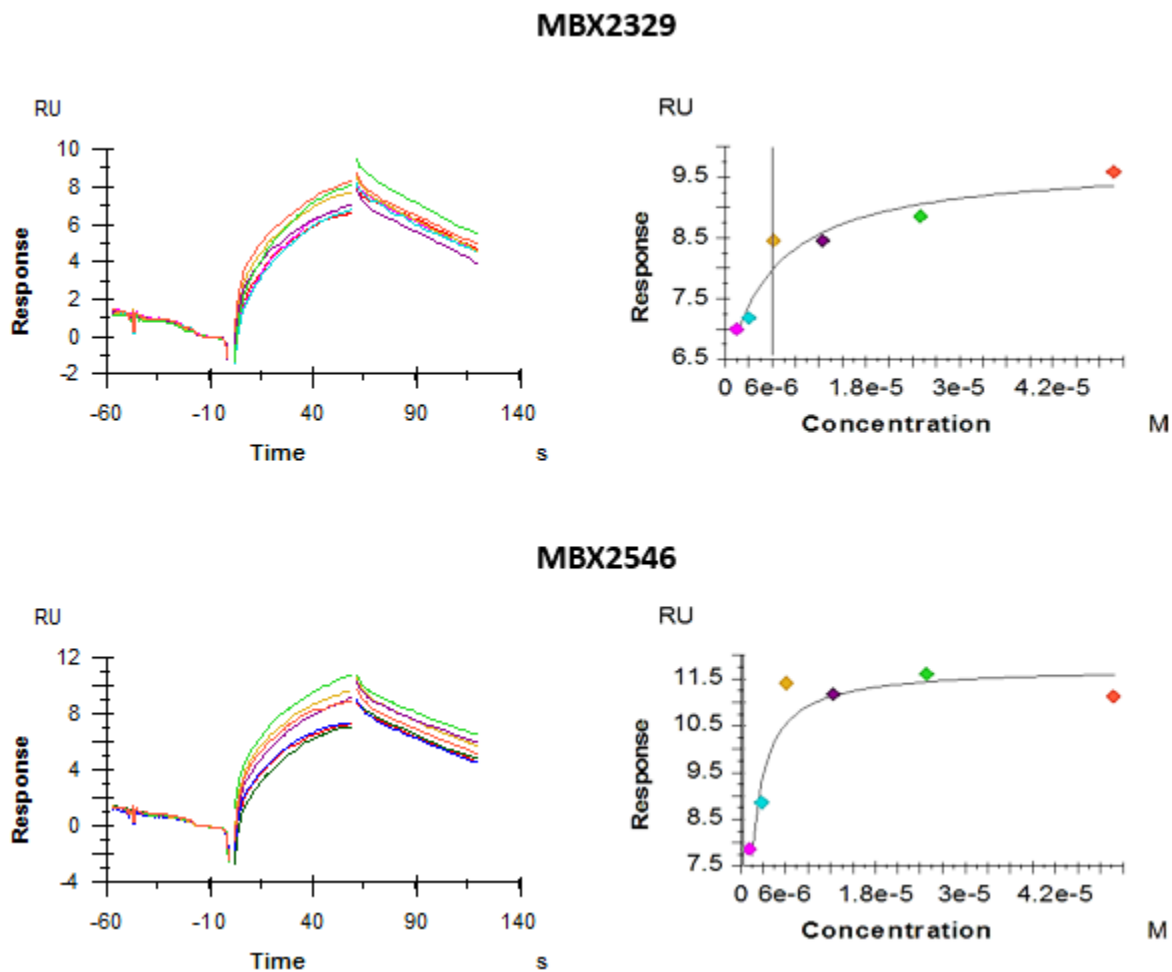


Figure 58. Raw SPR data for the binding of MBX2329 and MBX2546 to recombinant H5 HA. Sensograms are shown on the left and the corresponding steady-state binding curves are shown on the right. Corresponding concentration points in sensograms and binding curves share the same color.

Appendix D

Structural model of H3 HA with MBX2329 (blue), MBX2546 (yellow), RLC (orange) and TBHQ (red) bound is shown in the figure below. This model is based on experimentally determined x-ray structures with H5 HA (MBX2546, RLC), H3 HA (TBHQ) and molecular docking simulations (MBX2329).

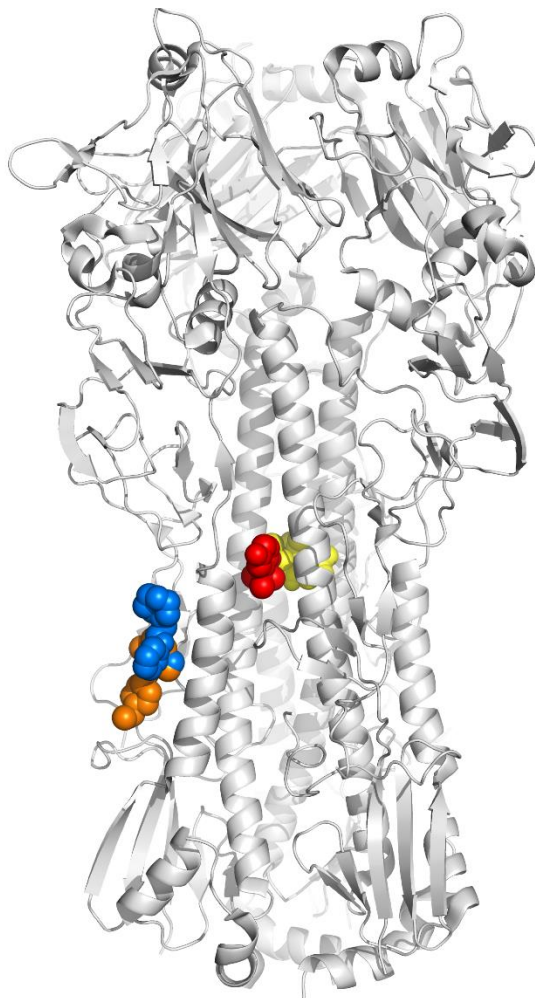


Figure 59. Proposed binding sites of MBX2329 (blue), MBX2546 (yellow), RLC (orange) and TBHQ (red) on HA. H3 HA structure was used in the model.

Literature

A

Adams PD, Afonine PV, Bunkóczi G, Chen VB, Davis IW, Echols N, Headd JJ, Hung LW, Kapral GJ, Grosse-Kunstleve RW, McCoy AJ, Moriarty NW, Oeffner R, Read RJ, Richardson DC, Richardson JS, Terwilliger TC, Zwart PH, PHENIX: a comprehensive Python-based system for macromolecular structure solution. *Acta Crystallogr D Biol Crystallogr*, Vol 66(Pt 2):213-21, 2010;

Antanasijevic A, Cheng H, Wardrop DJ, Rong L, Caffrey M, Inhibition of influenza H7 hemagglutinin-mediated entry. *PLoS One* Vol 23;8(10), 2013;

Antanasijevic A, Basu A, Bowlin TL, Mishra RK, Rong L, Caffrey M, Mutagenesis studies of the H5 influenza hemagglutinin stem loop region. *J Biol Chem*, Vol 8;289(32):22237-45, 2014a;

Antanasijevic A, Ramirez B, Caffrey M, Comparison of the sensitivities of WaterLOGSY and saturation transfer difference NMR experiments. *J Biomol NMR*, Vol 60:37–44, 2014b;

Antanasijevic A, Kingsley C, Basu A, Bowlin TL, Rong L, Caffrey M, Application of Virus-Like Particles (VLP) to Characterize the Interactions Between Inhibitors and Viral Membrane Proteins. *J Biomol NMR*, Vol 64(3):255-65, 2016;

Air GM, Influenza neuraminidase. *Influenza Other Respi Viruses*, Vol 6(4), 245-256, 2012;

B

Baell JB and Holloway GA, New substructure filters for removal of pan assay interference compounds (PAINS) from screening libraries and for their exclusion in bioassays. *J. Med Chem* Vol 53: 2719-40, 2010;

Balliet JW, Bates P, Efficient infection mediated by viral receptors incorporated into retroviral particles. *J Virol*, Vol 72:671–676, 1998;

Basu A, Antanasijevic A, Wang M, Li B, Mills DM, Ames JA, Nash PJ, Williams JD, Peet NP, Moir DT, Prichard MN, Keith KA, Barnard DL, Caffrey M, Rong L, Bowlin TL, New small molecule entry inhibitors targeting hemagglutinin-mediated influenza a virus fusion. *J Virol*, Vol 88(3):1447-60, 2014;

Berkower I, Raymond M, Muller J, Spadaccini A, Aberdeen A, Assembly, structure, and antigenic properties of virus-like particles rich in HIV-1 envelope gp120. *Virology*, Vol 321:75–86, 2004;

Bhunja A, Bhattacharjya S, Chatterjee S, Applications of saturation transfer difference NMR in biological systems. *Drug Discov Today*, Vol 17:505–513, 2012;

Bi S, Yan L, Sun Y, Zhang H, Investigation of ketoprofen binding to human serum albumin by spectral methods. *Spectrochim Acta A Mol Biomol Spectrosc*, Vol 78:410–414, 2010;

Bloom JD, Gong LI, Baltimore D, Permissive secondary mutations enable the evolution of influenza oseltamivir resistance. *Science*, Vol 328:1272–1275, 2010;

Bodian DL, Yamasaki RB, Buswell RL, Stearns JF, White JM, Kuntz ID, Inhibition of the fusion-inducing conformational change of influenza hemagglutinin by benzoquinones and hydroquinones. *Biochemistry*, Vol 32(12), 1993;

Boni MF, Nguyen TD, de Jong MD, van Doorn HR, Virulence attenuation during an influenza A/H5N1 pandemic. *Philos Trans R Soc Lond Biol Sci.*, Vol 368(1614), 2013;

Bullough PA, Hughson FM, Skehel JJ, Wiley DC, Structure of influenza haemagglutinin at the pH of membrane fusion. *Nature*, Vol 371(6492):37-43, 1994;

C

Caffrey M, HIV envelope: challenges and opportunities for the discovery of entry inhibitors. *Trends Microbiol*, Vol 19:191–197, 2011;

Cairo CW, Inhibitors of the human neuraminidase enzymes. *Med Chem Commun*, Vol 5:1067–1074, 2014;

Carlomagno T, Ligand–target interactions: what can we learn from NMR?. *Annu Rev Biophys Biomol Struct*, Vol 34:245–266, 2005;

Carra JH, Martins KA, Schokman RD, Robinson CG, Steffens JT, Bavari S, A thermostable, chromatographically purified Ebola nano-VLP vaccine. *J Transl Med*, Vol 13:228, 2015;

Chernomordik LV, Leikina E, Kozlov MM, Frolov VA, Zimmerberg J, Structural intermediates in influenza haemagglutinin-mediated fusion. *Mol Membr Biol*, Vol 16(1):33-42, 1999;

Collins PJ, Haire LF, Lin YP, Liu J, Russell RJ, Walker PA, Skehel JJ, Martin SR, Hay AJ, Gamblin SJ, Crystal structures of oseltamivir-resistant influenza virus neuraminidase mutants. *Nature*, Vol 453:1258–1261, 2008;

Costello DA, Whittaker GR, Daniel S, Variations in pH sensitivity, acid stability, and fusogenicity of three influenza virus H3 subtypes. *J Virol*, Vol 89(1):350-60, 2015;

Crooks ET, Moore PL, Franti M, Cayanan CS, Zhu P, Jiang P, de Vries RP, Wiley C, Zharkikh I, Schülke N, Roux KH, Montefiori DC, Burton DR, Binley JM, A comparative immunogenicity study of HIV-1 virus-like particles bearing various forms of envelope proteins, particles bearing no envelope and soluble monomeric gp120. *Virology*, Vol 366:245–262, 2000;

Cutting B, Shelke SV, Dragic Z, Wagner B, Gathje H, Kelm S, Ernst B, Sensitivity enhancement in saturation transfer difference (STD) experiments through optimized excitation schemes. *Magn Reson Chem*, Vol 45:720–724, 2007;

D

Dahlin JL and Walters MA, How to Triage PAINS-Full Research. *Assay Drug Dev Technol*, in press. 2015;

Dalvit C, Pevarello P, Tato M, Veronesi M, Vulpetti A, Sundstrom M, Time efficient detection of protein-ligand interactions with the polarization optimized PO-WaterLOGSY NMR experiment. *J Biomol NMR*, Vol 18:65–68, 2000;

Dalvit C, Fogliatto G, Stewart A, Veronesi M, Stockman B, WaterLOGSY as a method for primary NMR screening: practical aspects and range of applicability. *J Biomol NMR*, Vol 21:349–359, 2001;

de Graaf M, Fouchier RA, Role of receptor binding specificity in influenza A virus transmission and pathogenesis, *EMBO J.*, Vol 33(8), 823-41, 2014;

Delaglio F, Grzesiek S, Vuister W, Zhu G, Pfeifer J, et al., NMRPipe: A Multidimensional Spectral Processing System Based on UNIX pipes. *J Biomol NMR*, Vol 6: 277–293, 1995;

Donaldson LJ, Rutter PD, Ellis BM, Greaves FE, Mytton OT, Pebody RG, Yardley IE, Mortality from pandemic A/H1N1 2009 influenza in England: public health surveillance study. *BMJ*, Vol 339, 2009;

Dreyfus C, Ekiert DC, Wilson IA, Structure of a classical broadly neutralizing stem antibody in complex with a pandemic H2 influenza virus hemagglutinin. *J Virol*, Vol 87(12):7149-54, 2013;

E

Emsley P, Lohkamp B, Scott WG, Cowtan K, Features and development of Coot. *Acta Crystallogr D Biol Crystallogr*, Vol 66(Pt 4):486-501, 2010;

Endres MJ, Jaffer S, Haggarty B, Turner JD, Doranz BJ, O'Brien PJ, Targeting of HIV- and SIV-infected cells by CD4-chemokine receptor pseudotypes. *Science*, Vol 278:1462–1464, 1997;

F

Fauci AS, Emerging and Reemerging Infectious Diseases: The Perpetual Challenge. *Academic Medicine*, Vol. 80, 1079-1085, 2005;

Fontana J, Steven AC, Influenza virus-mediated membrane fusion: Structural insights from electron microscopy. *Arch Biochem Biophys*, Vol 1;581:86-97, 2015;

Franz AK and Wilson SO, Organosilicon Molecules with Medicinal Applications. *J Med Chem*, Vol 56 (2):388–405, 2013;

G

Garavito RM, Ferguson-Miller S, Detergents as tools in membrane biochemistry. *J Biol Chem*, Vol 276:32403–32406, 2001;

Garcia JM, Lai JC, Production of influenza pseudotyped lentiviral particles and their use in influenza research and diagnosis: an update. *Expert Rev Anti Infect Ther*, Vol 9:443–455, 2011;

Garcia JM, Lai JC, Haselhorst T, Choy KT, Yen HL, Peiris JS, von Itzstein M, Nicholls JM, Investigation of the binding and cleavage characteristics of N1 neuraminidases from avian, seasonal, and pandemic influenza viruses using saturation transfer difference nuclear magnetic resonance. *Influenza Other Respir Viruses*, Vol 8:235–242, 2014;

Garcia NK, Guttman M, Ebner JL, Lee KK, Dynamic changes during acid-induced activation of influenza hemagglutinin. *Structure*, Vol 23(4):665-76, 2015;

Gasparini R, Amicizia D, Lai PL, Bragazzi NL, Panatto D, Compounds with anti-influenza activity: present and future of strategies for the optimal treatment and management of influenza. Part II: Future compounds against influenza virus. *J Prev Med Hyg*, Vol 55(4):109-29, 2014;

Goodsell D, Molecule of the month: Hemagglutinin, rcsb.org, 2006;

Gossert AD, Henry C, Blommers MJ, Jahnke W, Fernández C, Time efficient detection of protein-ligand interactions with the polarization optimized PO-WaterLOGSY NMR experiment. *J Biomol NMR*, Vol 43:211–217, 2009;

Guo Y, Tisoncik J, McReynolds S, Farzan M, Prabhakar BS, Gallagher T, Rong L, Caffrey M, Identification of a new region of SARS-CoV S protein critical for viral entry. *J. Mol. Biol.*, Vol 394:600–605, 2009;

H

Hamilton BS, Whittaker GR, Daniel S, Influenza virus-mediated membrane fusion: determinants of hemagglutinin fusogenic activity and experimental approaches for assessing virus fusion. *Viruses*, Vol 4(7), 1144-1168, 2012;

Harner MJ, Frank AO, Fesik SW, Fragment-based drug discovery using NMR spectroscopy. *J Biomol NMR*, Vol 56:65–75, 2013;

Haselhorst T, Garcia JM, Islam T, Lai JC, Rose FJ, Nicholls JM, Peiris JS, von Itzstein M, Avian influenza H5-containing virus-like particles (VLPs): host-cell receptor specificity by STD NMR spectroscopy. *Angew Chem Int Ed Engl*, Vol 47:1910–1912, 2008;

Haynes JR, Influenza virus-like particle vaccines. *Expert Rev Vaccines*, Vol 8:435–445, 2009;

Herfst S, Schrauwen EJA, Linster M, Chutinimitkul S, de Wit E, Munster VJ, Sorrell EM, Bestebroer TM, Burke DF, Smith DJ, Rimmelzwaan GF, Osterhaus AD, Fouchier RAM, Airborne transmission of influenza A/H5N1 virus between ferrets. *Science*, Vol 336:1534–1541, 2012;

I

Iba Y, Fujii Y, Ohshima N, Sumida T, Kubota-Koketsu R, Ikeda M, Wakiyama M, Shirouzu M, Okada J, Okuno Y, Kurosawa Y, Yokoyama S, Conserved neutralizing epitope at globular head of hemagglutinin in H3N2 influenza viruses. *J Virol*, Vol 88(13):7130-44, 2014;

Ilyushina NA, Govorkova EA, Russell CJ, Hoffmann E, Webster RG, Contribution of H7 haemagglutinin to amantadine resistance and infectivity of influenza virus. *J Gen Virol*, Vol 88: 1266–1274, 2007;

Ivanovic T, Harrison SC, Distinct functional determinants of influenza hemagglutinin-mediated membrane fusion. *Elife*. Vol 27:4. pii: e11009, 2015;

Ivanovic T, Choi JL, Whelan SP, van Oijen AM, Harrison SC, Influenza-virus membrane fusion by cooperative fold-back of stochastically induced hemagglutinin intermediates. *Elife*, Vol 19;2:e00333, 2013;

J

Jacobs A, Sen J, Rong L, Caffrey M, Alanine scanning mutagenesis of the HIV gp41 loop. *J Biol Chem*, Vol 280:27284– 27288, 2005;

Jalaguier P, Turcotte K, Danylo A, Cantin R, Tremblay MJ, Efficient production of HIV-1 virus-like particles from a mammalian expression vector requires the N-terminal capsid domain. *PLoS ONE*, Vol 6:e28314, 2011;

Jayalakshmi V, Krishna NR, Complete relaxation and conformational exchange matrix (CORCEMA) analysis of intermolecular saturation transfer effects in reversibly forming ligandreceptor complexes. *J Magn Reson*, Vol 155:106–118, 2002;

Jiang H, Wang J, Manicassamy B, Manicassamy S, Caffrey M, Rong L, The role of the charged residues of the GP2 helical regions in Ebola entry. *Virol. Sin.*, Vol 24:121–135, 2009;

Julien JP, Cupo A, Sok D, Stanfield RL, Lyumkis D, Deller MC, Klasse PJ, Burton DR, Sanders RW, Moore JP, Ward AB, Wilson IA, Crystal structure of a soluble cleaved HIV-1 envelope trimer. *Science*, Vol 342:1477–1483, 2013;

K

Kabsch W, XDS. *Acta Cryst*, Vol D66:125-132, 2010;

Kalani MR, Moradi A, Moradi M, Tajkhorshid E, Characterizing a histidine switch controlling pH-dependent conformational changes of the influenza virus hemagglutinin. *Biophys J*, Vol 20;105(4):993-1003, 2013;

Kouznetsova J, Sun W, Martínez-Romero C, Tawa G, Shinn P, Chen CZ, Schimmer A, Sanderson P, McKew JC, Zheng W, GarciaSastre A, Identification of 53 compounds that block Ebola virus-like particle entry via a repurposing screen of approved drugs. *Emerg Microbes Infect*, Vol 3:e84, 2014;

Ku PI, Miller AK, Ballew J, Sandrin V, Adler FR, Saffarian S, Identification of pauses during formation of HIV-1 virus like particles. *Biophys J*, Vol 105:2262–2272, 2013;

Kuhn JH, Li W, Radoshitzky SR, Choe H, Farzan M, Severe acute respiratory syndrome coronavirus entry as a target of antiviral therapies. *Antivir Ther*, Vol 12:639–650, 2007;

Kumari K, Gulati S, Smith DF, Gulati U, Cummings RD, Air GM, Receptor binding specificity of recent human H3N2 influenza viruses. *Virology*, Vol 4(42), 2007;

L

Lagoja IM, De Clercq E, Anti-influenza virus agents: synthesis and mode of action. *Med Res Rev*, Vol 28:1–38, 2008;

Lam TT, Zhou B, Wang J, Chai Y, Shen Y, Chen X, Ma C, Hong W, Chen Y, Zhang Y, Duan L, Chen P, Jiang J, Zhang Y, Li L, Poon LL, Webby RJ, Smith DK, Leung GM, Peiris JS, Holmes EC, Guan Y, Zhu H, Dissemination, divergence and establishment of H7N9 influenza viruses in China. *Nature*, Vol 4: 522(7554), 2015;

Lee JE, Fusco ML, Hessel AJ, Oswald WB, Burton DR, Saphire EO, Structure of the Ebola virus glycoprotein bound to an antibody from a human survivor. *Nature*, Vol 454:177–182, 2008;

Ley NB, Rowe ML, Williamson RA, Howard MJ, Optimising selective excitation pulses to maximize saturation transfer difference NMR spectroscopy. *RSC Adv*, Vol 4:7347–7351, 2014;

Li F, Ma C, Wang J, Inhibitors targeting the influenza virus hemagglutinin. *Curr Med Chem*, Vol 22(11):1361-82, 2015;

Li Q, Qi J, Zhang W, Vavricka CJ, Shi Y, Wei J, Feng E, Shen J, Chen J, Liu D, He J, Yan J, Liu H, Jiang H, Teng M, Li X, Gao GF, The 2009 pandemic H1N1 neuraminidase N1 lacks the 150-cavity in its active site. *Nat Struct Mol Biol*, Vol 17:1266–1268, 2010;

Luo G, Colonno R, Krystal M, Characterization of a hemagglutinin-specific inhibitor of influenza A virus. *Virology*, Vol 226(1), 66-76, 1996;

Luo M, Influenza virus entry. *Adv Exp Med Biol*, Vol 726, 201-221, 2012;

M

Madhusoodanan M, Lazaridis T, Investigation of pathways for the low-pH conformational transition in influenza hemagglutinin. *Biophys J*, Vol 84(3):1926-39, 2003;

Mair CM, Meyer T, Schneider K, Huang Q, Veit M, Herrmann A, A histidine residue of the influenza virus hemagglutinin controls the pH dependence of the conformational change mediating membrane fusion. *J Virol*, Vol 88(22):13189-200, 2014;

Mamos P, Krokidis MG, Papadas A, Karahalios P, Starosta AL, Wilson DN, Kalpaxis DL, Dinos GP, On the use of the antibiotic chloramphenicol to target polypeptide chain mimics to the ribosomal exit tunnel. *Biochimie*, Vol 95:1765–1772, 2013;

Marathe BM, Lévêque V, Klumpp K, Webster RG, Govorkova EA, Determination of neuraminidase kinetic constants using whole influenza virus preparations and correction for spectroscopic interference by a fluorogenic substrate. *PLoS ONE*, Vol 8:e71401, 2013;

Mayer M, Meyer B, Group epitope mapping by saturation transfer difference NMR to identify segments of a ligand in direct contact with a protein receptor. *J Am Chem Soc*, Vol 123:6108–6117, 2001;

Mayer M, James TL, Detecting ligand binding to a small RNA target via saturation transfer difference NMR experiments in D₂O and H₂O. *J Am Chem Soc*, Vol 124:13376–13377, 2002;

McBurney S, Young K, Ross T, Membrane embedded HIV-1 envelope on the surface of a virus-like particle elicits broader immune responses than soluble envelopes. *Virology*, Vol 358: 334–346, 2007;

McKimm-Breschkin JL, Influenza neuraminidase inhibitors: antiviral action and mechanisms of resistance. *Influenza Other Respir Viruses*, Vol 7(Suppl 1):25–36, 2013;

Meindl P, Bodo G, Palese P, Schulman J, Tuppy H, Inhibition of neuraminidase activity by derivatives of 2-deoxy-2,3-dehydro-N-acetylneuraminic acid. *Virology*, Vol 58:457–463, 1974;

Mittal A, Leikina E, Chernomordik LV, Bentz J, Kinetically differentiating influenza hemagglutinin fusion and hemifusion machines. *Biophys J*, Vol 85(3):1713-24, 2003;

Mohan S, McAtamney S, Haselhorst T, von Itzstein M, Pinto BM, Carbocycles related to oseltamivir as influenza virus group-1-specific neuraminidase inhibitors. Binding to N1 enzymes in the context of virus-like particles. *J Med Chem*, Vol 53:7377–7391, 2010;

N

Nelson MI, Holmes EC, The evolution of epidemic influenza, *Nat Rev Genet.*, Vol 8(3):196-205, 2007;

Ni F, Chen X, Shen J, Wang Q, Structural insights into the membrane fusion mechanism mediated by influenza virus hemagglutinin. *Biochemistry*, Vol 53(5):846-54, 2014;

O

Official Centers for Disease Control and Prevention website at <http://www.cdc.gov/>

Ooi N, Chopra I, Eady A, Cove J, Bojar R, O'Neill AJ, Antibacterial activity and mode of action of tert-butylhydroquinone (TBHQ) and its oxidation product, tert-butylbenzoquinone (TBBQ). *J Antimicrob Chemother*, Vol 68(6):1297-304, 2013;

P

Papp I, Sieben C, Sisson AL, Kostka J, Böttcher C, Ludwig K, Herrmann A, Haag R, Inhibition of influenza virus activity by multivalent glycoarchitectures with matched sizes. *Chembiochem*, Vol 12(6), 887-895, 2011;

Potter CW, A history of influenza. *Journal of applied Microbiology*, Vol 91, 572-579, 2001;

Q

Qian Z, Dominguez SR, Holmes KV, Role of the spike glycoprotein of human Middle East respiratory syndrome coronavirus (MERSCoV) in virus entry and syncytia formation. *PLoS ONE*, Vol 8:e76469, 2013;

R

Rademacher C, Krishna NR, Palcic M, Parra F, Peters T, NMR experiments reveal the molecular basis of

receptor recognition by a calicivirus. *J Am Chem Soc*, Vol 130:3669–3675, 2008;

Rameix-Welti MA, Agou F, Buchy P, Mardy S, Aubin JT, Véron M, van der Werf S, Naffakh N, Natural variation can significantly alter the sensitivity of influenza A (H5N1) viruses to oseltamivir. *Antimicrob Agents Chemother*, Vol 50:3809–3815, 2006;

Ramirez BE, Antanasijevic A, Caffrey M, Ligand screening using NMR. *Methods Mol Biol*, Vol 1140:305–313, 2014;

Reed ML, Yen HL, DuBois RM, Bridges OA, Salomon R, Webster RG, Russell CJ, Amino acid residues in the fusion peptide pocket regulate the pH of activation of the H5N1 influenza virus hemagglutinin protein. *J Virol*, Vol 83(8):3568-80, 2009;

Remeta DP, Krumbiegel M, Minetti CA, Puri A, Ginsburg A, Blumenthal R, Acid-induced changes in thermal stability and fusion activity of influenza hemagglutinin. *Biochemistry*, Vol 41(6):2044-54, 2002;

Russell CJ, Acid-induced membrane fusion by the hemagglutinin protein and its role in influenza virus biology, *Curr Top Microbiol Immunol.*, Vol 385, 93-116, 2014;

Russell RJ, Kerry PS, Stevens DJ, Steinhauer DA, Martin SR, Gamblin SJ, Skehel JJ, Structure of influenza hemagglutinin in complex with an inhibitor of membrane fusion. *Proc Natl Acad Sci U S A*, 105(46), 17736-17741, 2008;

S

Sakabe S, Iwatsuki-Horimoto K, Horimoto T, Nidom CA, Le Mt, Takano R, Kubota-Koketsu R, Okuno Y, Ozawa M, Kawaoka Y, A cross-reactive neutralizing monoclonal antibody protects mice from H5N1 and pandemic (H1N1) 2009 virus infection. *Antiviral Res*, Vol 88:249–255, 2010;

Schlünzen F, Zarivach R, Harms J, Bashan A, Tocilj A, Albrecht R, Yonath A, Franceschi F, Structural basis for the interaction of antibiotics with the peptidyl transferase centre in eubacteria. *Nature*, Vol 413:814–821, 2011;

Schrodinger LLC, MacroModel version 9.8, Schrodinger LLC, New York, 2012;

Sen J, Yan T, Wang J, Rong L, Tao L, Caffrey M, Alanine scanning mutagenesis of the HIV-1 gp41 heptad repeat 1: insight into the gp120-gp41 Interaction. *Biochemistry*, Vol 49:5057–5065, 2010;

Shuker SB, Hajduk PJ, Meadows RP, Fesik SW, Discovering high-affinity ligands for proteins: SAR by NMR. *Science*, Vol 274:1531–1534, 1996;

Skehel JJ, Wiley DC, Receptor binding and membrane fusion in virus entry: the influenza hemagglutinin. *Annu Rev Biochem*, Vol 69:531–569, 2000;

Sowell J, Mason JC, Streckowski L, Patonay G, Binding constant determination of drugs toward subdomain

IIIA of human serum albumin by near-infrared dye-displacement capillary electrophoresis. *Electrophoresis*, Vol 22:2512–2517, 2001;

Steel J, Lowen AC, Wang TT, Yondola M, Gao Q, Haye K, García-Sastre A, Palese P, Influenza Virus Vaccine Based on the Conserved Hemagglutinin Stalk Domain. *mBio*, Vol 1, 2010;

Stevens J, Corper AL, Basler CF, Taubenberger JK, Palese P, Wilson IA, Structure of the uncleaved human H1 hemagglutinin from the extinct 1918 influenza virus. *Science*, Vol 303(5665):1866-70; 2004;

Stevens J, Blixt O, Tumpey TM, Taubenberger JK, Paulson JC, Wilson IA, Structure and receptor specificity of the hemagglutinin from an H5N1 influenza virus. *Science*, Vol 312:404–410, 2006;

Stray SJ, Cummings RD, Air GM, Influenza virus infection of desialylated cells. *Glycobiology*, Vol 10(7), 649-658, 2000;

Sun X, Shi Y, Lu X, He J, Gao F, Yan J, Qi J, Gao GF, Bat-derived influenza hemagglutinin H17 does not bind canonical avian or human receptors and most likely uses a unique entry mechanism. *Cell Rep*, Vol 3: 769-778, 2013;

T

Tedbury PR, Mercredi PY, Gaines CR, Summers MF, Freed EO, Elucidating the mechanism by which compensatory mutations rescue an HIV-1 matrix mutant defective for gag membrane targeting and envelope glycoprotein incorporation. *J Mol Biol*, Vol 427:1413–1427, 2015;

Thoennes S, Li ZN, Lee BJ, Langley WA, Skehel JJ, Russell RJ, Steinhauer DA, Analysis of residues near the fusion peptide in the influenza hemagglutinin structure for roles in triggering membrane fusion. *Virology*, Vol 20;370(2):403-14, 2008;

Tripes International, SybylX 1.3, Tripes International, St. Louis, MI, 2013;

U

Ueda M, Maeda A, Nakagawa N, Kase T, Kubota R, Takakura H, Ohshima A, Okuno Y, Application of subtype-specific monoclonal antibodies for rapid detection and identification of influenza A and B viruses. *J Clin Microbiol*, Vol 36: 340–344, 1998;

V

van Esch GJ, Toxicology of tert-butylhydroquinone (TBHQ). *Food Chem Toxicol*, Vol 24: 1063-1065, 1986;

Vanderlinden E, Göktas F, Cesur Z, Froeyen M, Reed ML, Russell CJ, Cesur N, Naesens L, Novel inhibitors of influenza virus fusion: structure-activity relationship and interaction with the viral hemagglutinin. *J Virol*, Vol 84(9), 4277-4288, 2010;

von Itzstein M, The war against influenza: discovery and development of sialidase inhibitors. *Nat Rev Drug Discov*, Vol 6:967–974, 2007;

W

Wang J, Cheng H, Ratia K, Varhegyi E, Hendrickson WG, Li J, Rong L, A comparative high-throughput screening protocol to identify entry inhibitors of enveloped viruses. *J Biomol Screen*, Vol 19:100–107, 2014;

Wang W, DeFeo CJ, Alvarado-Facundo E, Vassell R, Weiss CD, Intermonomer Interactions in Hemagglutinin Subunits HA1 and HA2 Affecting Hemagglutinin Stability and Influenza Virus Infectivity. *J Virol*, Vol 89(20):10602-11, 2015;

Wang M, Tscherne DM, McCullough C, Caffrey M, García-Sastre A, Rong L, Y161 is a critical residue of HA for receptor recognition. *J Virol*, Vol 86:4455–4462, 2012;

Wathen MW, Barro M, Bright RA, Antivirals in seasonal and pandemic influenza--future perspectives. *Influenza Other Respi Viruses*, Vol 7 Suppl 1:76-80, 2013;

Williamson MP, Chapter 3: Applications of the NOE in molecular biology. In: Webb GA (ed) *Annual reports on NMR spectroscopy*, Academic Press, Vol 65. pp 77–109, 2009;

Winn MD, Ballard CC, Cowtan KD, Dodson EJ, Emsley P, Evans PR, Keegan RM, Krissinel EB, Leslie AG, McCoy A, McNicholas SJ, Murshudov GN, Pannu NS, Potterton EA, Powell HR, Read RJ, Vagin A, Wilson KS, Overview of the CCP4 suite and current developments. *Acta Crystallogr D Biol Crystallogr*, Vol 67(Pt 4):235-42, 2011;

X

Xu R, Wilson IA, Structural characterization of an early fusion intermediate of influenza virus hemagglutinin. *J Virol*, Vol 85(10):5172-82, 2011;

Xie Y, Gong J, Li M, Fang H, Xu W, The medicinal potential of influenza virus surface proteins: hemagglutinin and neuraminidase. *Curr Med Chem*, Vol 18(7):1050-66, 2011;

Y

Yang J, Li M, Shen X, Liu S, Influenza A Virus Entry Inhibitors Targeting the Hemagglutinin. *Viruses*, Vol 5(1), 352-373, 2013;

Yermolina MV, Wang J, Caffrey M, Rong LL, Wardrop DJ, Discovery, synthesis, and biological evaluation of a novel group of selective inhibitors of filoviral entry. *J Med Chem*, Vol 54:765–781, 2011;

Yonezawa A, Cavrois M, Greene WC, Studies of Ebola virus glycoprotein-mediated entry and fusion by using pseudotyped Human Immunodeficiency Virus type 1 virions: involvement of cytoskeletal proteins and enhancement by tumor necrosis factor alpha. *J Virol*, Vol 79:918–926, 2005;

Z

Zhang S, Xiao L, Zhou H, Yu Z, Chen H, Guo A, Jin M, Generation and characterization of an H5N1 avian influenza virus hemagglutinin glycoprotein pseudotyped lentivirus. *J Virol Methods*, Vol 154:99–103, 2008;

Zhang W, Shi Y, Lu X, Shu Y, Qi J, Gao GF, An airborne transmissible avian influenza H5 hemagglutinin seen at the atomic level. *Science*, Vol 340:1463–1467, 2013;

Zhu L, Li Y, Li S, Li H, Qiu Z, Lee C, Lu H, Lin X, Zhao R, Chen L, Wu JZ, Tang G, Yang W, Inhibition of influenza A virus (H1N1) fusion by benzenesulfonamide derivatives targeting viral hemagglutinin. *PLoS One*, Vol 6: e29120, 2011;

Zhu P, Liu J, Bess J Jr, Chertova E, Lifson JD, Grisé H, Ofek GA, Taylor KA, Roux KH, Distribution and three-dimensional structure of AIDS virus envelope spikes. *Nature*, Vol 441:847–852, 2006;

Zhu T, Lee H, Lei H, Jones C, Patel K, Johnson ME, Hevener KE, Fragment-based drug discovery using a multidomain, parallel MD-MM/PBSA screening protocol. *J Chem Inf Model*, Vol 53(3):560-72, 2013;

Zhu X, Yu W, McBride R, Li Y, Chen LM, Donis RO, Tong S, Paulson JC, Wilson IA, Hemagglutinin homologue from H17N10 bat influenza virus exhibits divergent receptor-binding and pH-dependent fusion activities. *PNAS*, Vol 110: 1458-1463, 2013;

Zhu Z, Li R, Xiao G, Chen Z, Yang J, Zhu Q, Liu S, Design, synthesis and structure-activity relationship of novel inhibitors against H5N1 hemagglutinin-mediated membrane fusion. *Eur J Med Chem.*, Vol 57, 211-216, 2012;

VITA

Name	Aleksandar Antanasijevic
Education	B.A. Faculty of Physical Chemistry, University of Belgrade, Belgrade, Serbia, 2010 M.S. Faculty of Physical Chemistry, University of Belgrade, Belgrade, Serbia, 2011
Teaching	BMS 648 - Medical Biochemistry and Nutrition (College of Medicine, UIC) - Teaching assistant, Fall 2013 and Fall 2014.
Honors and Awards	<ul style="list-style-type: none"> - Dean's Scholar Award, University of Illinois at Chicago (UIC), Chicago, IL, 2014 - Chicago Biomedical Consortium (CBC) scholars award, Chicago, IL, 2014 - Baxter Young Investigator Award - 2nd tier, Baxter International Inc., 2014 - The best scientific poster award on the 6th annual Department of Biochemistry and Molecular Genetics (UIC) retreat, Lake Geneva, WI, 2013 - Pavle Savić Award for outstanding success during the undergraduate studies, University of Belgrade, Belgrade, Serbia, 2014 - The best student in the class of 2006, High School, Gymnasium "Bora Stanković", Vranje, Serbia - The best student in the class of 2002, Elementary School "Radoje Domanović", Vranje, Serbia
Publications	<p>[1] Antanasijevic A, Cheng H, Wardrop DJ, Rong L, Caffrey M. Inhibition of Influenza H7 Hemagglutinin- Mediated Entry, PLoS One. 2013, 8(10):e76363.</p> <p>[2] Basu A, Antanasijevic A, Wang M, Li B, Mills DM, Ames JA, Nash PJ, Williams JD, Peet NP, Moir DT, Prichard MN, Keith KA, Barnard DL, Caffrey M, Rong L, Bowlin TL. New small molecule entry inhibitors targeting hemagglutinin-mediated influenza A virus fusion, J Virol. 2014, 88(3):1447-60.</p> <p>[3] Ramirez B, Antanasijevic A, Caffrey M. Ligand screening using NMR, Methods and Protocols. Series: Methods in Molecular Biology, Vol. 1140. Anderson, Wayne F. (Ed.), Humana Press, 2014, 344p.</p> <p>[4] Ratia, Light S, Antanasijevic A, Anderson WF, Caffrey M, Lavie A. Discovery of selective inhibitors of the Clostridium difficile dehydroquininate dehydratase, PLoS ONE, 2014, 9(2): e89356.</p> <p>[5] Light SH, Antanasijevic A, Krishna SN, Caffrey M, Anderson WF, Lavie A. Crystal Structures of Type I Dehydroquininate Dehydratase in Complex with Quinate and Shikimate Suggest a Novel Mechanism of Schiff Base Formation, Biochemistry, 2014, 53 (5), pp 872–880.</p>

- [6] **Antanasijevic A**, Ramirez B, Caffrey M. Comparison of the sensitivities of WATERLOGSY and STD NMR experiments, *J Biomol NMR*. 2014, 60(1):37-44.
- [7] **Antanasijevic A**, Basu A, Bowlin TL, Mishra RK, Rong L, Caffrey M. Mutagenesis studies of the H5 Influenza stem loop region, *J Biol Chem*. 2014, 289(32):22237-45.
- [8] Nomme J, **Antanasijevic A**, Caffrey M, Van Itallie CM, Anderson JM, Fanning AS, Lavie A. Structural basis of a key factor regulating the affinity between the zonula occludens first PDZ domain and claudins, *J Biol Chem*. 2015, 290(27):16595-606.
- [9] Schalk AM, **Antanasijevic A**, Caffrey M, Lavie A. Experimental data in support of a direct displacement mechanism for Type I/II L-asparaginases, *J Biol Chem*. 2016, pii: jbc.M115.699884.
- [10] **Antanasijevic A**, Kingsley C, Basu A, Bowlin TL, Rong L, Caffrey M, Application of Virus-Like Particles (VLP) to Characterize the Interactions Between Inhibitors and Viral Membrane Proteins. *J Biomol NMR*, Vol 64(3):255-65, 2016;
- [11] **Antanasijevic A**, Hafeman N, Kingsley C, Mishra RK, Rong L, Wardrop DJ, Manicassamy B, Caffrey M, Stabilization and improvement of a promising influenza antiviral: Making a PAIN PAINless, submitted.
- [12] Nguyen HA, Su Y, Zhang JY, **Antanasijevic A**, Caffrey M, Merrill BJ, Lavie A High L-glutaminase co-activity is not required for in vivo efficacy of L-asparaginases, submitted.